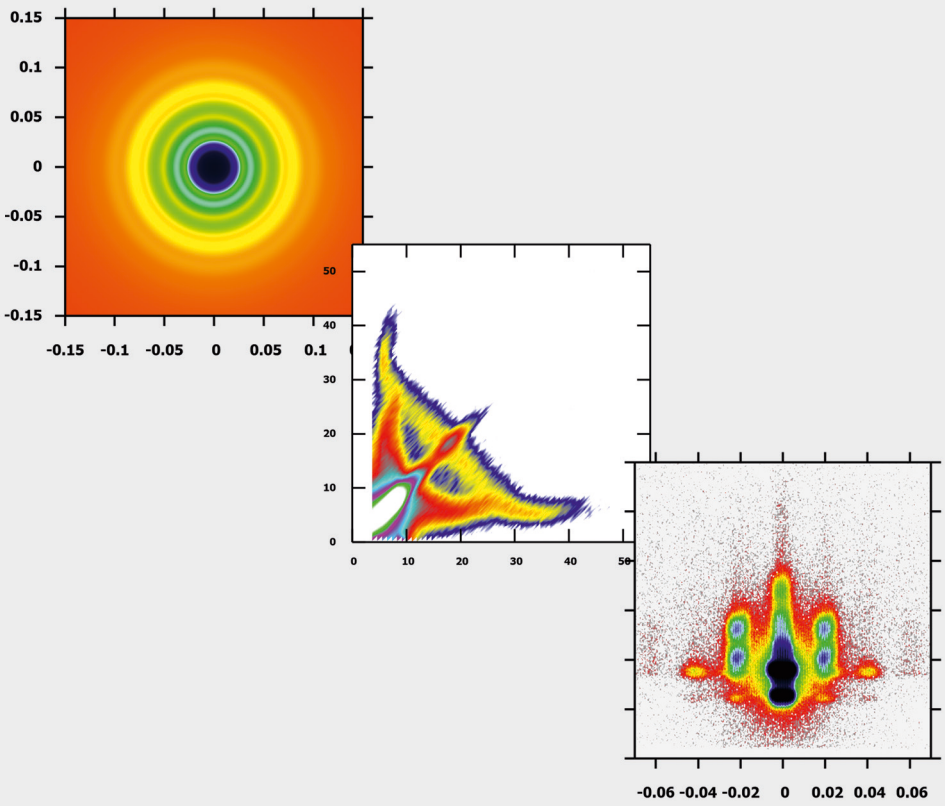

The guided self-assembly of magnetic nanoparticles into two- and three-dimensional nanostructures using patterned substrates

Wenhai Ji

Schlüsseltechnologien / Key Technologies
Band / Volume 214
ISBN 978-3-95806-462-1

Mitglied der Helmholtz-Gemeinschaft

JÜLICH
Forschungszentrum

Schriften des Forschungszentrums Jülich
Reihe Schlüsseltechnologien / Key Technologies Band / Volume 214

Forschungszentrum Jülich GmbH
Jülich Centre for Neutron Science (JCNS)
Quantenmaterialien und kollektive Phänomene (JCNS-2 / PGI-4)

The guided self-assembly of magnetic nanoparticles into two- and three-dimensional nanostructures using patterned substrates

Wenhai Ji

Schriften des Forschungszentrums Jülich
Reihe Schlüsseltechnologien / Key Technologies Band / Volume 214

ISSN 1866-1807 ISBN 978-3-95806-462-1

Bibliografische Information der Deutschen Nationalbibliothek.
Die Deutsche Nationalbibliothek verzeichnet diese Publikation in der
Deutschen Nationalbibliografie; detaillierte Bibliografische Daten
sind im Internet über http://dnb.d-nb.de abrufbar.

Herausgeber und Vertrieb:	Forschungszentrum Jülich GmbH Zentralbibliothek, Verlag 52425 Jülich Tel.: +49 2461 61-5368 Fax: +49 2461 61-6103 zb-publikation@fz-juelich.de www.fz-juelich.de/zb
Umschlaggestaltung:	Grafische Medien, Forschungszentrum Jülich GmbH
Druck:	Grafische Medien, Forschungszentrum Jülich GmbH
Copyright:	Forschungszentrum Jülich 2020

Schriften des Forschungszentrums Jülich
Reihe Schlüsseltechnologien / Key Technologies, Band / Volume 214

D 82 (Diss. RWTH Aachen University, 2020)

ISSN 1866-1807
ISBN 978-3-95806-462-1

Vollständig frei verfügbar über das Publikationsportal des Forschungszentrums Jülich (JuSER)
unter www.fz-juelich.de/zb/openaccess.

Abstract

The present thesis provides an original and extensive contribution to the understanding of the self-assembly of magnetic nanoparticles in different dimensions with the help of patterned sapphire substrates and block copolymers. The combination of real space and reciprocal space techniques allows a better understanding of nanostructures with different dimensions, which are formed on the patterned substrates.

The first topic covered in the thesis is formation of 2D nanoparticle assemblies by annealing the M-plane sapphire at various temperatures. The procedure is adjusted to obtain patterned substrates that can accommodate the nanoparticles of a given size. The highly-ordered 2D magnetic nanoparticles arrays deposited on patterned sapphire substrates were studied using scanning electron microscopy and grazing incidence x-ray scattering (GISAXS) methods. In addition, a detailed analysis of GISAXS data using the Distorted Wave Born Approximation theory allowed characterizing the samples quantitatively. The second topic is to deal with the self-organization of 3D nanoparticles assemblies over the macroscopic scale, with precise control of the spatial organization of nanoparticles by employing the block copolymers. It was achieved by controlling the morphology of the block copolymer films with a solvent vapor annealing, which proved to be a powerful method. It was demonstrated that the solvent volume, annealing time and drying process had an impact on the final morphology of the nanocomposite film. The influence of those parameters was thoroughly investigated and optimum values were derived. The orientation parameter obtained from GISAXS measurements allows identifying the different stages of the alignment of the block copolymer matrix. Using developed approach, 3D nanoparticles with a long-range order in nanocomposite film can be readily obtained on patterned substrates, which were confirmed by both atomic force microcopy and GISAXS methods. The magnetic interactions between magnetic nanoparticles in nanocomposite film, containing only 8 wt % of nanoparticles were studied with polarized neutron scattering experiments. The qualitative analysis of the grazing incidence neutron scattering and polarized neutron reflectometry data, combined with GISAXS data analysis, unambiguously demonstrated that a weak magnetic scattering from array of magnetic nanoparticles can be detected. The methodology developed in this work exemplifies a key role of polarized neutron scattering techniques in characterization of magnetic inter-particle interactions embedded in complex nanocomposite materials.

In conclusion, this work shows how 2D and 3D nanoparticles assemblies can be prepared by using patterned substrates and how preparation parameters affect the resulting nanostructures. The vital role of various scattering methods in qualitative characterization of structural and magnetic properties of nanostructures was emphasized.

Zusammenfassung

Die vorliegende Arbeit leistet einen originalen und umfassenden Beitrag zum Verständnis der Selbstorganisation von magnetischen Nanopartikeln in verschiedenen Dimensionen, mit Hilfe von strukturierten Saphir-Substraten und Blockcopolymeren. Die Kombination von Techniken im Realraum als auch im reziproken Raum erlaubt ein besseres Verständnis von Nanostrukturen mit verschiedenen Dimensionen, welche auf strukturierten Substraten gebildet werden.

Der erste Teil beinhaltet die Bildung der 2D-Organisation der Nanopartikel durch Erhitzen der M-Ebene des Saphir-Substrates in Abhängigkeit der angelegten Temperatur. So können die Substrate gezielt auf die jeweiligen Durchmesser der gewünschten Nanopartikel angepasst werden. Die hochgeordneten 2D magnetischen Nanopartikel-Anordnungen werden mittels Rastereleketronenmikroskopie (SEM) und Röntgenstreuung unter streifendem Einfall (GISAXS) charakterisiert. Eine quantitative Analyse der GISAXS-Daten wurde unter Verwendung der “Distorted-Wave Born-Approximation” (DWBA)-Theorie durchgeführt.

Der zweite Teil der Arbeit beschäftigt sich mit der Organisation 3-dimensionaler Nanopartikelstrukturen auf makroskopischer Längenskala, mit präziser Kontrolle über die räumliche Anordnung der Nanopartikel durch die Verwendung von Blockcopolymeren. Als geeignetes Mittel zur Bestimmung der Morphologie der Blockcopolymere stellt sich das Erhitzen unter Lösungsmitteldampf heraus. Es wird beschrieben, dass sowohl das Lösungsmittelvolumen, als auch die Aufwärmzeit und der Trocknungsprozess erheblichen Einfluss auf die endgültige Morphologie der Nanokompositschichten besitzen. Der Einfluss dieser Parameter wird innerhalb einer umfangreichen Studie dargestellt und die optimalen Prozessparameter wurden ermittelt. Mit Hilfe von GISAXS Messungen der Orientierung der Schichten werden die verschiedenen Phasen der Anordnung der Blockcopolymermatrix bestimmt. Mit diesem Vorgehen können langreichweitige 3D-Strukturierungen von Nanopartikeln innerhalb der Nanokompositfilme auf bereits vorstrukturierten Substraten gebildet werden. Dies wird mit Atomkraftmikroskopie (AFM), als auch mit GISAXS Messungen belegt. Zudem werden die magnetischen Wechselwirkungen von Nanopartikeln mit nur 8 Gew.-% mittels Polarisierter Neutronenreflektometrie (PNR) studiert. Die Ergebnisse von PNR und Neutronenstreuung unter streifendem Einfall (GISANS) zeigen unter Vergleich mit den GISAXS Daten, dass eine schwache magnetische Streuung von den Arrays der magnetischen Nanopartikel beobachtet werden kann. Die so ermittelten Methoden aus einem Zusammenspiel von PNR, GISANS und GISAXS verdeutlichen den Nutzen von polarisierter Neutronenstreuung für die Charakterisierung der magnetischen Inter-Partikel Wechselwirkungen von Nanopartikeln eingebettet in komplexen Nanokompositmaterialien.

Zusammenfassend wird in dieser Arbeit das Wachstum selbstorganisierter 2D und 3D Nanopartikel-Strukturen mit Hilfe von vorstrukturierten Substraten vorgestellt und der Einfluss verschiedener Prozessparameter auf die Nanopartikel ermittelt. Eine wichtige Rolle bildet dabei die Verwendung verschiedener Streumethoden zur qualitativen Charakterisierung der strukturellen und magnetischen Eigenschaften der Nanopartikel.

Contents

Chapter 1 Introduction

1.1 Motivation

The self-assembly of nanoparticles is described as a process in which individual nanoparticles spontaneously form a defined and organized structure from the nanoscale. The chemical methods developed over the past decades enable fabrication of nanoparticles with uniform size and various shapes [1-3]. Monodisperse nanoparticles are ideal candidates for self-assembly as 'building blocks' to form two and three dimensional structure, respectively. Depending on specifics of applications, such as magnetic storage media, drug delivery systems, biosensors, solar cells and catalysis, varieties of interesting nanoparticles with distinctive magnetic, biological, electrical, mechanical, optical and chemical properties can be chosen [4-10].

Nevertheless, how to direct the self-assembly process to form desired structures is still a big challenge. A lot of efforts have been made to manipulate the arrangement of nanoparticles [11-13]. Guided self-assembly with templates or external fields can provide rich opportunities for building fruitful self-assembled structures [14-16]. Furthermore, direct imaging techniques and scattering techniques are needed to obtain the structural information on various scales. By combining different techniques, the structure and properties of an artificial material made up by nanoparticles can be tailored to meet specific requirements in applications.

1.2 Concept

The aim of this thesis is to achieve highly ordered 2D and 3D arrangements of magnetic nanoparticles. The following chapter 2 briefly introduces theoretical backgrounds related to this thesis, which includes magnetism, self-assembly and basics of scattering theory. All employed experimental methods and corresponding instruments used in this thesis are described in chapter 3. They can be divided into real space (TEM, SEM and AFM) and reciprocal space (SAXS, GISAXS, PGISANS and PNR) techniques. Transmission electron microscopy (TEM) has been used to provide the size/size distribution and shape information of nanoparticles which are combined with results obtained from small angle x-ray scattering (SAXS). The topography images have been obtained with scanning electron microscopy (SEM) and atomic force microscopy (AFM) on a micrometer scale. In addition, the phase images have been taken by AFM. Grazing incidence small angle x-ray scattering (GISAXS) has been employed as the most important method for probing the nanostructures over a large illuminated area. Besides, the challenge of magnetic structure determination has been addressed with polarized

grazing incidence small angle neutron scattering (PGISANS) and polarized neutron reflectometry (PNR) measurements. Since the nanoparticles and patterned substrates are fundamental materials used in the thesis, Chapter 4 presents the characterization of nanoparticles and patterned substrates, before they are combined during the self-assembly process.

The present thesis describes three different systems, and the investigations mainly focus on how to achieve highly ordered self-assembly of nanoparticles of different dimensions and how to properly characterize them. The first objective is to prepare 2D self-assembly of nanoparticles via patterned substrate (chapter 5). Simulations of GISAXS data based on Distorted-wave Born approximation (DWBA) are carried out to gain a deeper understanding of the sample structure. The second goal of the thesis is to control the process of 3D self-assembly of nanoparticles in polymer film (chapter 6). Thus, the influence of different spin coating parameters, solvent vapor annealing and drying process is systematically investigated by GISAXS and AFM to optimize the sample preparation. The DWBA simulations provide more information about buried nanostructures located underneath the surface. A highlight of this thesis is to extend and enhance the use of polarized neutron scattering on the nanocomposite film embedded with low concentration (8 wt %) of magnetic nanoparticles (chapter 7). Those challenging experiments prove the feasibility of neutron scattering and showcase how many different techniques can be combined for investigations of the complex sample with a low concentration of magnetic nanoparticles. The thesis ends with a summary and an outlook in the chapter 8.

1.3 Current state of the research

Templated self-assembly combines bottom-up self-assembly with top-down patterned templates to eliminate defects and induce orientation in final structures, providing rich opportunities to fabricate designed structures. To produce 2D self-assembly of nanoparticles, various prefabricated topographical templates (Anodic aluminum oxide, patterned Si by lithography, surface reconstructed M-Al_2O_3, and so on) have been employed. The V-shaped grooves on Si substrates can guide polystyrene (PS) beads to form different 2D arrays and even helical chains [17]. By changing the size of a 2D array of cylindrical holes on Si substrates using conventional photolithography, monomers, dimers or trimmers of PS beads can be found in the holes [18]. By tuning the shape of templates, more complex structures are possible [19-21]. Lithography is a powerful method to design complex patterns to control the self-assembly while the high cost of lithography limits widespread applications. The surface reconstructed M-Al_2O_3 shows some advantages which is more economical and easy to produce. However, as far as we know, there has been no report on directing self-assembly of nanoparticles by using patterned sapphire to form 2D nanostructure.

And for controlling the self-assembly of copolymer based film, there are only four reports using patterned sapphire substrates. Park et al. reported ultrahigh-density arrays using cylindrical microdomains of polystyrene-block-poly(ethylene oxides) (PS-b-PEO) on patterned sapphire substrates. The cylinders are perpendicular to the surface. This is the initial report of guided block copolymer self-assembly with patterned sapphire [22]. Reconstructed faceted sapphire substrates have also been shown to induce a high degree of alignment in cylinder-forming PS-b-PEO films deposited on them, wherein the unidirectionally aligned cylinders are parallel to the surface [23]. Nanocomposite thin films (polystyrene-block-poly(4-vinylpyridine) (PS-P4VP) and 3-n-Pentadecylphenol (PDP)) containing 3D Au nanoparticles arrays with long-range order can be readily obtained by using patterned sapphire substrates [24]. Employed the self-assembled of polystyrene-b-poly(methyl methacrylate) (PS-b-PMMA) film on patterned sapphire substrate as the further template, monodisperse metal nanostructures in highly regular arrays covering the block copolymer surface were produced by magnetron sputter deposition [25]. This concept has not been extended to the case of nanocomposite thin films doped with magnetic nanoparticles yet.

Investigation of nanocomposite samples is usually done by AFM, TEM, SAXS and GISAXS. For the structure characterization by neutron scattering techniques, small angle neutron scattering (SANS) [26], grazing incidence small angle neutron scattering (GISANS) [27], and neutron reflectivity (NR) [28, 29] have been employed to study the structure of nanocomposite materials. PNR and PGISANS could allow one to understand the magnetization distribution between nanostructures. But PNR and PGISANS have rarely been reported in investigation of nanocomposite embedded with nanoparticles until now.

Chapter 2 Theoretical background

This chapter outlines the relevant background knowledge needed to perform and analyze the experimental data described in the rest of this thesis. The first section (2.1) of this chapter describes the fundamentals of magnetism. The second part (2.2) explains the self-assembly. The basics of x-ray/neutron scattering theory and the different scattering methods used in the thesis are given in section 2.3.

2.1 Magnetism

2.1.1 Basics of magnetism

The present section is written to give an insight into fundamentals of magnetism, types of magnetic materials and superparamagnetic nanoparticles [1]. The best way to introduce the different types of magnetism is to describe how materials respond to magnetic fields. When magnetic field is applied to materials, some of them are attracted by the field and some of them are repelled by the field. The susceptibility (χ) is defined as:

$$\chi = \frac{M}{H} \tag{2.1}$$

Where *H* is magnetic field and *M* is magnetization. The susceptibility is a dimensionless scalar which is a measure of how magnetizable a substance can become in the presence of a magnetic field and thus, it can help to distinguish the various classes of magnetic materials. The net magnetic moment depends on the magnetic moments of individual atoms, which depend on the spin and orbital motions of electrons, and interactions with other magnetic moments. We classify magnetic materials into five types as shown in Table 2.1.

Table 2. 1 The classification of materials.

Classification	susceptibility (χ)	Magnetic order and χ vs. T
Diamagnetism	negative, $(-10^{-6} \leq \chi \leq -10^{-5})$ temperature independent	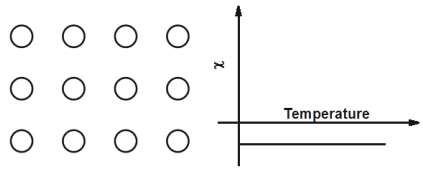
Paramagnetism	positive, $(10^{-5} \leq \chi \leq 10^{-3})$ temperature dependent	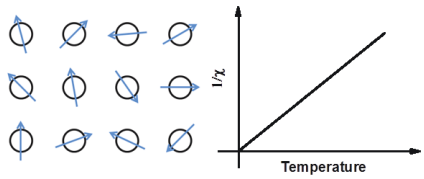
Ferromagnetism	positive, $(\chi \gg 0)$ temperature dependent	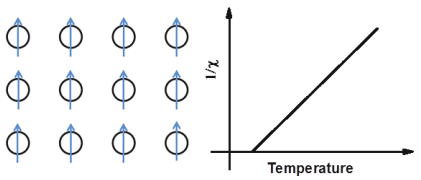
Antiferromagnetism	positive, $(\chi > 0)$ temperature dependent	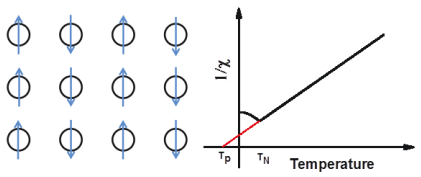
Ferrimagnetism	positive, $(\chi \gg 0)$ temperature dependent	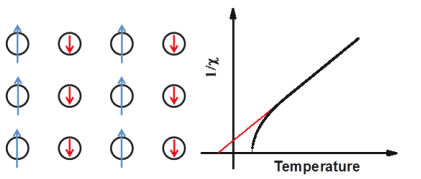

In **diamagnetic** materials, there are no unpaired electrons and all the orbital shells are filled. The net magnetic moment is zero. When external field is applied, it will produce a magnetization in the opposite direction to the applied field. Thus, the susceptibility is negative $(-10^{-6} \leq \chi \leq -10^{-5})$ and temperature independent. For other types of

magnetic materials, the susceptibility is temperature dependent. Above the critical temperature, the thermal energy exceeds exchange interaction energy and a material shows paramagnetic behavior. We can use the Curie-Weiss law to describe the relation between susceptibility and temperature shown as below [1]:

$$\chi = \frac{C}{T-\theta} \tag{2.2}$$

Where T is temperature, C is materials constant called Curie constant and θ is Weiss constant. If $\theta = 0$, the substance is in the **paramagnetic** state. This state is characterized by a positive susceptibility ($10^{-5} \leq \chi \leq 10^{-3}$). Due to unpaired electrons in partially filled orbitals, each individual atom has a permanent magnetic moment in the paramagnetic state. Because of thermal motion, magnetic moments point in random directions and net magnetization is zero.

For **ferromagnetic** materials ($\theta > 0$) all the magnetic moments are parallel to each other and aligned in the same direction, as shown in Table 2.1. The magnetic order in ferromagnetic materials is destroyed above the critical temperature T_C (Curie temperature).

The magnetic order of **antiferromagnetic** materials ($\theta < 0$) is composed of two magnetic sublattices as shown in Table 2.1. The magnetic moments in the neighboring sublattice are the same, but aligned in the opposite direction, leading to zero net magnetic moment for vanishing magnetic field. Above the critical temperature T_N (Néel temperature), the antiferromagnetic materials transform into a paramagnetic state.

The magnetic order of **ferrimagnetic** materials is also composed of two magnetic sublattices similar to antiferromagnets, but magnetic moments in each sublattice are different and result in a net magnetic moment. The magnetic behavior is very similar to ferromagnetic materials, but ferrimagnetic materials usually have lower saturation magnetization.

2.1.2 Superparamagnetism

When the size of a ferromagnetic material is reduced to nanoscale size, it can only sustain a single-domain magnetic structure. The single-domain nanoparticle can be then described as a single magnetic spin. The orientation of the spin can be affected by both thermal fluctuations and applied magnetic field.

This phenomenon occurs in nanoparticles and it is known as **superparamagnetism**. The following equation can be used to estimate the critical radius r_C, below which a nanoparticle is a single domain [2]:

$$r_c \approx 9\frac{\sqrt[2]{AK_u}}{\mu_0 {M_s}^2} \tag{2.3}$$

where A is the exchange constant, K_u is the uniaxial anisotropy constant, μ_0 is the vacuum permeability, and M_S is the saturation magnetization. The size-dependent coercivity of small magnetic particles is shown schematically in Fig. 2.1. According to this behavior, the coercivity of magnetic particles increases with the reduction of particle size. It reaches a maximum at the single domain size (r_C) and then decreases again for smaller particles due to thermal effects and becomes zero when the size is well below r_C. The typical critical radius of nanoparticles used in this work is 45 nm and 64 nm for maghemite and magnetite, respectively [3]. Superparamagnetic NPs can be aligned either parallel or antiparallel to a particular direction, depending on their magnetic energy.

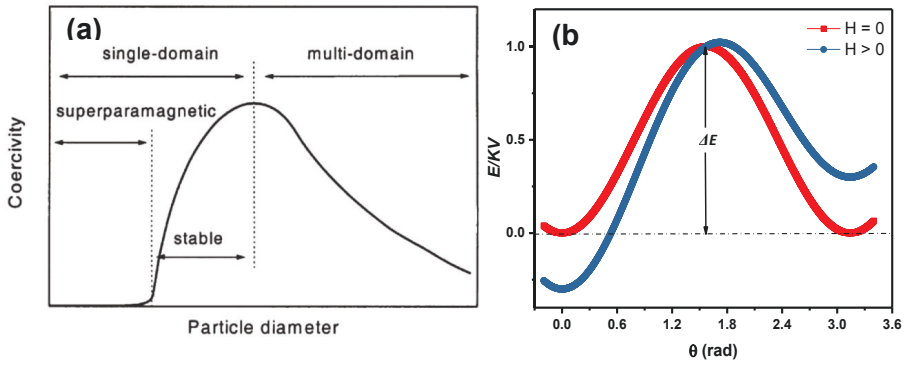

Fig. 2. 1 (a) Size dependence of coercivity of magnets. Taken from [5]. (b) The magnetic energy of a single-domain particle with uniaxial anisotropy as a function of the direction of the magnetization with H = 0 and H > 0.

The magnetic energy of a single nanoparticle is described by the Stoner-Wohlfarth model and is given by [4]:

$$E = K_{eff} V sin^2\theta - \mu_0 M_S V H\, cos(\varphi - \theta) \tag{2.4}$$

where K_{eff} the effective anisotropy constant, V is the volume of nanoparticle, H is the applied field, θ is the angle between magnetic moment and anisotropy axis and ϕ is the angle between the applied magnetic field and the anisotropy axis. The energy has two minima at θ=0 and π separated by the energy barrier of ΔE ($\Delta E = K_{eff} V$), in zero magnetic field. In order to reverse its magnetization a nanoparticle needs to overcome the energy barrier ΔE. If the magnetic field H is applied, the energy barrier becomes

asymmetric and the magnitude of the energy barrier also changes (Fig 2.1(b)). For superparamagnetic nanoparticles, the energy barrier *ΔE* is small compared to $k_B T$ (k_B is Boltzmann's constant and T is the temperature) and magnetization can be easily reversed by thermal fluctuations even in the absence of an external magnetic field. When $k_B T > \Delta E$, the particle will behave similar to a paramagnet. When $k_B T < \Delta E$, they again behave as single domain particles with magnetic hysteresis. The critical temperature at which the thermal energy can overcome the barrier is referred to as the blocking temperature (T_B). T_B is not an intrinsic property of the nanoparticles and it depends on the experimental measuring time.

According to the Néel-Brown law [6, 7] the spin relaxation time (τ) follows the Arrhenius-type equation:

$$\tau = \tau_0 exp\left(\frac{\Delta E}{k_B T}\right) \tag{2.5}$$

where τ_0 is a material-dependent constant, with typical values in the order of 10^{-9} s. The equation (2.5) demonstrates a profound effect of the temperature on the magnetization reversal in nanoparticles. As the temperature is increasing, the relaxation time will become short, which means magnetization fluctuates fast. When τ is longer than the measuring time of the experimental technique, the system is best described as static. Below T_B, the magnetization is blocked in one of the energy minima states during the measurements. The temperature dependent magnetization measurements (*M-T)* include measurements of two different curves for zero-field-cooling (ZFC) and field-cooling (FC), as shown in Fig 2.2(a).

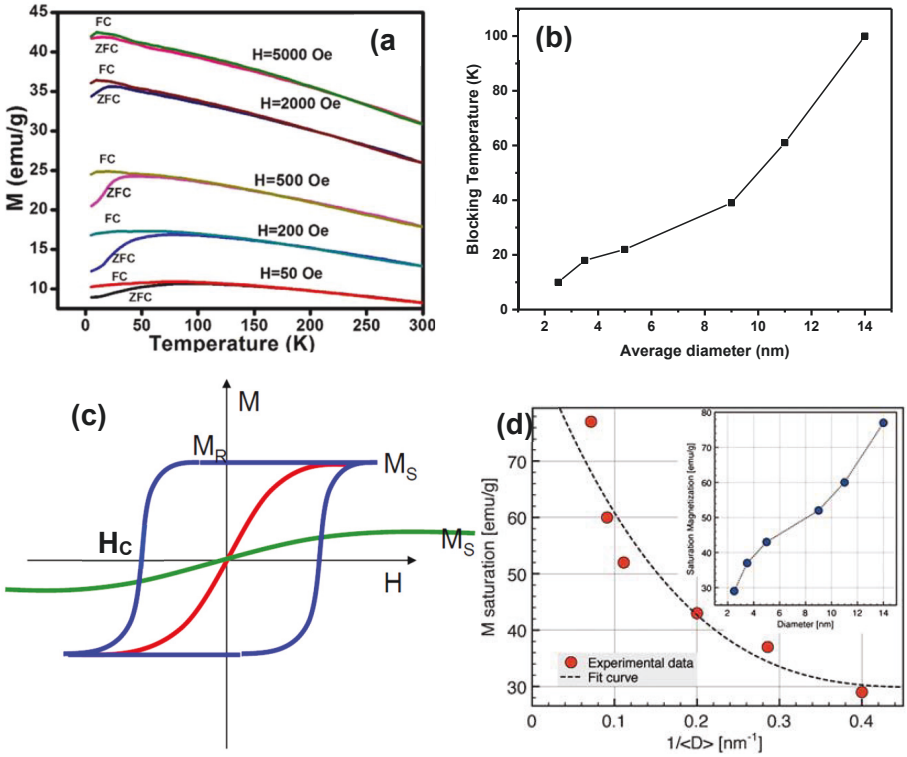

Fig. 2. 2 Typical (a) *M-T* of iron oxide nanoparticles with T_B dependences on the field of iron oxide with an average diameter of 10 nm. Taken from [26]. (b) Size-dependent blocking temperature of magnetic iron oxide nanoparticles. Adopted from [9]. (c) M-H curves of ferromagnets (blue), paramagnets (green) and superparamagnetic (red) nanoparticles. (d) The size-dependent saturation magnetization of iron oxide nanoparticles at 5 K. Taken from [9].

For ZFC measurements, the sample is cooled in zero field, and then a small field is applied. The magnetization is recorded as a function of increasing temperature. During zero field cooling, the two energy minima are equal. When small field is applied, it is too small to induce sufficient magnetization reversal at low temperature. With increasing temperature, thermal fluctuations induce to magnetization reversal in the direction of applied field. When the magnetization crosses its peak value, the effective thermal fluctuations decrease the magnetization. For FC measurements, the sample is cooled under applied magnetic field down to the base temperature, introducing unequal energy minima. The magnetization is then recorded during heating as a function of temperature. In experiment, bifurcation of ZFC and FC magnetizations indicates the transition of

magnetic nanoparticles into the blocked state. The peak in ZFC magnetization defines T_B. T_B depends on the field applied during the measurements and size of particles, as shown in Fig 2.2 (a) and (b). In general, an applied field will lead to a reduction of the blocking temperature. In *M-H* curves of superparmagnetic materials, there will be a high saturation magnetization (M_S) and zero coercivity field (no open loop) and remanence magnetization (M_R) above T_B (Fig 2.2 (c)). While ferromagnets have an open loop with large M_S, and paramagnets have no open loop with small M_S. Those facts make it easier to distinguish superparamagnets from ferromagnets and paramagnets. The saturation magnetization of iron oxide nanoparticles is also found size-dependent as shown in Fig. 2.2 (d).

The most prominent interaction in superparamagnetic nanoparticles is the **magnetic dipolar interaction**. Two magnetic dipoles μ_1 and μ_2 separated by r have energy equal to:

$$E = \frac{\mu_0}{4\pi r^3}\left[\boldsymbol{\mu_1}\boldsymbol{\mu_2} - \frac{3}{r^2}(\boldsymbol{\mu_1}\cdot\boldsymbol{r})(\boldsymbol{\mu_2}\cdot\boldsymbol{r})\right] \quad (2.6)$$

where μ_0 is the magnetic constant. One can easily estimate the order of magnitude of the dipolar energy of two spherical maghemite nanoparticles with radius of 3 nm (a saturation moment of 3913 μ_B calculated from a magnetization per formula unit of 2.5 μ_B [10], a cell volume of 578 $Å^3$ and 8 formula units per unit cell) at room temperature. In order to estimate the effect of the distance on the energy of the dipolar interactions, two different center to center distances of 25 nm and 10 nm were considered. The latter corresponds to the closest distances between the particles covered with organic shell of 2 nm thickness. The corresponding energies are 1 K and 18 K, respectively. Thus, we can conclude that the dipolar interaction is much weaker in nanocomposites films studied here with large particle-to-particle separation than in closely packed ensemble of nanoparticles.

The **magnetic anisotropy** is used to describe the dependence of the internal energy on the direction of the magnetization. The net magnetization of a system will prefer to lie along so-called easy axis. The energetic difference between the easy and hard axes results from two microscopic interactions: the spin-orbit interaction and the long-range dipolar-interactions of magnetic moments. The spin-orbit coupling is responsible for **magnetocystalline anisotropy**, **surface anisotropy** and **strain anisotropy**, while **shape anisotropy** is a dipolar- contribution. In bulk materials, magnetocrystalline and magnetostatic energies are the main sources of anisotropy, whereas in nanoparticles other kinds of anisotropies such as shape and surface anisotropy are relevant in addition [11]. The shape anisotropy is calculated by assuming a uniform distribution of magnetic poles on the surfaces. A uniformly magnetized spherical superparamagnetic nanoparticle has no shape anisotropy, because the demagnetizing factors are isotropic

in all directions. For spherical superparamagnetic nanoparticles with radius *r*, the effective magnetic anisotropy can be expressed as:

$$K_{eff} = K_V + \frac{S}{V}K_S \tag{2.7}$$

Where $S = 4\pi r^2$ and $V = \frac{4}{3}\pi r^3$are the surface and the volume of the NPs. K_V and K_S are the volume and surface anisotropies, respectively [12].

2.2 Self-assembly

The self-assembly is defined as a process in which individual units of material spontaneously form a defined and organized structure or larger units with a minimal external influence. In this work, we focused on the self-assembly of nanoparticles, which uses nanoparticle as building blocks. The self-assembly is a highly useful technique of nanofabrication because of its simplicity and versatility. The self-assembly is a new tool in creating the next generation smart materials. A variety of methods can be used for self-assembly of nanoparticles, such as dip-coating, drop-casting and spin coating. This section will describe the self-assembly processes without and with external control.

2.2.1 Self-assembly without control

Typically, assembly is occurring in a solvent, or during solvent evaporation, to ensure the particles have enough mobility and time to assemble. The process is often driven by inter-particle interactions, surrounding environment or combination of both.

The **Van-der-Waals interactions** are distance-dependent interactions between atoms or molecules. The Van-der-Waals forces are driven by dipole-dipole interactions when two or more atoms or molecules are very close to each other. When an instantaneous dipole atom or permanent dipole atom approaches a neighboring atom, it can cause this atom to also produce dipoles. The dipole-dipole interactions can occur between two permanent dipoles, between a permanent dipole and an induced dipole, and between two induced dipoles. The Van der Waals interaction is the weakest of all intermolecular attractions between molecules. The Van-der-Waals force between spherical bodies of radii r_1 and r_2 and with smooth surfaces [27]:

$$\mathrm{F} = -\frac{Ar_1r_2}{6(r_1+r_2)d^2} \tag{2.8}$$

where A is the Hamaker coefficient, which is a constant (~10^{-19} - 10^{-20} J) that depends on the material properties, and *d* ($d \ll r_1$ or r_2) is the distance between the surfaces. However, with a closed distance between two objects, the interaction can be very strong. In our work the solvent evaporation will bring nanoparticles close to each other and Van

der Waals interactions can be considerable during dip-coating, drop-casting and spin coating processes.

The steric repulsion is another effect that needs to be considered in our preparation methods. Most of the nanoparticles are covered by a layer of surface-bound molecules (ligands), and dispersed in solution. These ligands are often introduced during synthesis and composed of mostly short alkyl chains. The steric repulsion provided by these small surfactants is sometimes not strong enough. One approach to improve nanoparticle assembly is modifying the nanoparticle surface, typically through ligating functional molecules to the surface or through the modification of existing ligands [13]. The coordinative ligand exchange can be thermodynamically described by a reaction: $\mathrm{NP\text{-}L_1 + L_2 \rightleftarrows NP\text{-}L_2 + L_1}$, where NP-$L_1$ are the NP coated with the original low molecular weight ligand L_1, and NP-L_2 are the NPs coated with the desired big size ligand L_2. By surface modification, Van der Waals interaction can be balanced and NPs will stay well separated after a solvent is evaporated.

2.2.2 Self-assembly with control

2.2.2.1 External field directed assembly

Some external forces induced by an electric or magnetic field can be applied to restrict the movement of nanoparticles during assembly process. The electric field is the most commonly used external field, which can be used to polarize nanoparticles or their ligand shell, causing them to form chains or colloidal crystals [14]. It is typically applied by setting a high voltage across a pair of planar electrodes on either side, while controlling the evaporation rate. The electric field force ($\mathrm{F = qE}$) is depend on the electric field intensity (E) and the quantity of induced charge (q). The magnetic field can also be used to align nanoparticles which have magnetic moment [15]. When magnetic nanoparticles are exposed to an external magnetic field, the field will force nanoparticles to align along the field direction. The magnetic field force ($\mathrm{F} = (M_s \mathrm{V} \cdot \nabla)\mathrm{B}$) is depend on the saturation magnetization of nanoparticles (Ms), the nanoparticle volume (V), and the magnetic induction (B). Hence, one can directly tune the magnetic dipole-dipole interactions between magnetic NPs.

2.2.2.2 Templated self-assembly

The self-assembly of nanoparticles can be achieved by using templates. A patterned substrate is a simple and effective template, which can be used to align and order nanoparticles more precisely as compared to a flat surface. Anodic aluminum oxide (AAO), lithography Si grating and annealing sapphire are the main patterned **hard templates** (Fig 2.3). Due to their vertical pore channel structures, AAO template

provides ideal voids that can be filled with the nanoparticles dispersion to provide 1D assembly of nanoparticles. The anodization process is used to fabricate AAO on a surface of high purity aluminum foil [16]. The lithography Si grating can be used to align and distribute nanoparticles more precisely than methods described above by controlling the width and depth of the trenches [17]. Moreover, lithography is also a powerful method to design more complex patterns to control the self-assembly. The M-plane (1 0 -1 0) sapphire substrate surface is unstable, and spontaneously forms primarily (-1 1 0 1) and (1 -1 0 2) facets upon annealing at high temperatures [18]. After annealing at high temperatures, the surface of sapphire' M-plane will form saw-tooth patterns. The height of a saw-tooth pattern of sapphire is controlled by the temperature and annealing time, providing very little room for adjustment. We used annealed sapphire as the template in this work.

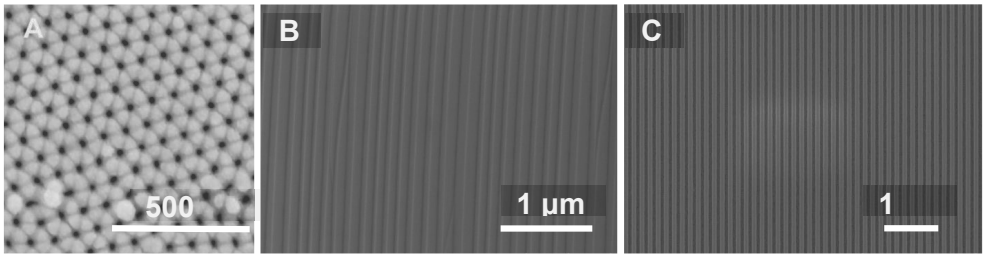

Fig. 2. 3 SEM images of (a) AAO taken from [16], (b) annealed sapphire and (c) lithography Si grating.

The di-block copolymers (DBP) are also possible to be used as a **soft template** [19]. The DBP consist of two distinct polymer segments connected with a chemical covalent bond. The repulsive interaction between the chemically different blocks leads them to segregate into two phases. The process can be understood from Gibb's free energy.

$$G = H - TS \tag{2.9}$$

The homogeneous phase domain size is in a mesoscopic scale, which mainly depends on the lengths of both blocks. Driven by entropic and enthalphic interactions between both blocks, micro-phase separates to form mesoscopic scale periodic spatial structures. This separation is called microphase separation. We can also call this microphase separation the self-assembly of the DBP. The morphology of the periodic spatial structures depends on molecular weight, volume fractions of blocks, polydispersity, as well as on polymer-polymer interaction between both blocks. A variety of nanostructures can be formed by increasing the volume fraction of one block (Fig 2.4), such as body-centered cubic spheres, hexagonally packed cylinders, lamellae and gyroid. As the volume fraction further increases, the similar morphologies are formed inversely, i.e. A domains in B matrix transform into B domains in A matrix.

The glass transition temperature (Tg) defines a critical transitional temperature, above which the polymer starts to behave like the soft rubber. Below Tg, the polymer starts freezing like the hard glass. Tg is an important parameter during the self-assembly of the DBP. Thermal annealing and solvent vapor annealing are main methods to achieve the self-assembly of the block copolymers. The thermal annealing needs to be performed above the Tg of both blocks and below the order-disorder transition temperature (above which DBP lose their order) of the block copolymer. When the solvent vapor annealing is applied, the DBP are exposed to a solvent vapor, which reduces the Tg and increases the polymer chain mobility. This is why solvent vapor annealing can be performed at room temperature.

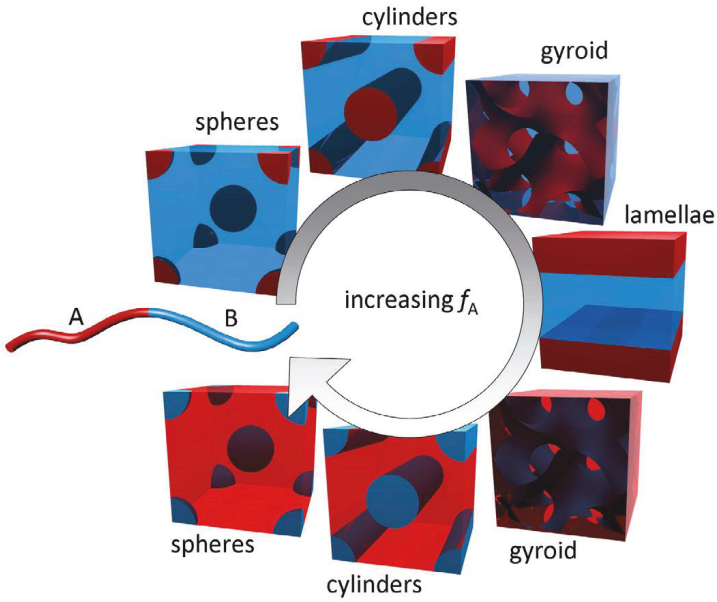

Fig. 2. 4 Different phases formed by self-assembly of di-block copolymers in the bulk as a function of the volume fraction of one of the blocks (f_A). Taken from [20].

2.3 Scattering methods

In general, scattering is the physical process in which radiation or moving particles are being deflected by an object from the straight propagation. If there is no exchange of energy, we call it elastic scattering, otherwise it is called the inelastic scattering. X-ray and neutron scattering methods in particular, are a non-destructive and very powerful tool to understand the morphology and atomic structure of a material. The principle interaction processes are depicted schematically in Fig 2.5 for x-rays and neutrons. The

x-ray interacts with the electron cloud of an atom. Thus, heavy atoms with a high atomic number are good x-ray scatterers. Neutrons are neutral particles with a magnetic moment and interact with nuclei. Therefore, neutrons have much higher penetration depth as compared to x-rays. If an atom has unpaired electrons, the magnetic moment of neutrons will interact with the magnetic moment of unpaired electrons by dipole-dipole interaction [21-22].

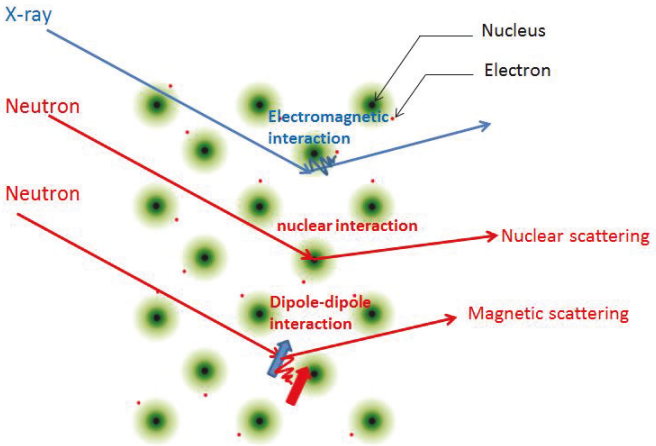

Fig. 2. 5 X-rays and neutrons interaction with atoms.

2.3.1 Basics of scattering

The scattering vector is defined as: $\vec{Q} = \overrightarrow{k_f} - \overrightarrow{k_i}$, where $\overrightarrow{k_f}$ is the wave vector of the scattered beam, $\overrightarrow{k_i}$ is the wave vector of the incident beam (Fig 2.6). The magnitude of the wave vector is given by:

$$\left|\vec{k}\right| = \frac{2\pi}{\lambda} = k \tag{2.10}$$

where λ is the wavelength. The modulus of the scattering vector can be calculated from the wavelength and scattering angle:

$$\mathrm{Q} = \left|\vec{Q}\right| = \sqrt{k_f^2 + k_i^2 - 2k_f k_i \cos 2\theta} \tag{2.11}$$

In scattering experiments, the measurement of the intensity distribution $I(\vec{Q})$ is obtained as a function of the scattering vector $\vec{Q}$. The scattered intensity is proportional to so-called double differential cross section:

$$I(\vec{Q}) \propto \frac{d^2\sigma}{d\Omega\, dE} = \frac{N}{\Phi\, d\Omega\, dE} \tag{2.12}$$

Where *N* is the number of particles scattered per second into a solid angle *dΩ*, with the final energy between *E* and *E+dE*, and Φ is the particles flux of the incident beam.

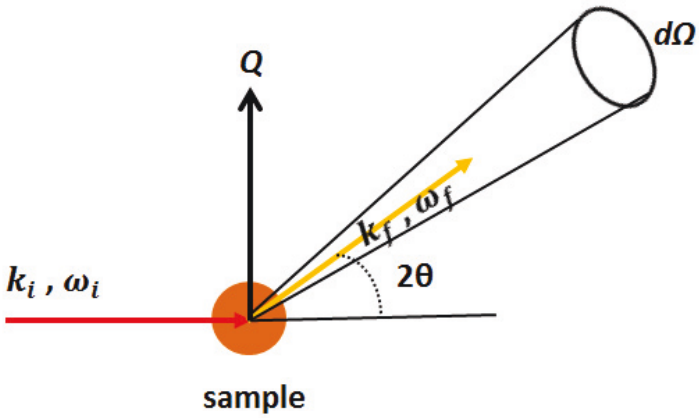

Fig. 2.6 A sketch of the scattering process and geometry used for the definition of the scattering vector and the scattering cross section.

For elastic scattering, the energy is not analyzed and the number of scattered neutrons is counted. We can describe the angular dependence by the differential cross section:

$$\frac{d\sigma}{d\Omega} = \int \frac{d^2\sigma}{d\Omega\, dE} dE \tag{2.13}$$

The total scattering cross section, which gives the total scattering probability of the sample, is written as the integral over the entire solid angle:

$$\sigma = \int_0^{4\pi} \frac{d\sigma}{d\Omega} d\Omega \tag{2.14}$$

In quantum mechanics, scattering can be described as a particle wave through the Schrödinger equation:

$$\hat{H}\Psi(\vec{r}) = \left[-\frac{\hbar^2}{2m}\nabla^2 + V(\vec{r})\right]\Psi(\vec{r}) = E\Psi(\vec{r}) \tag{2.15}$$

Where $\Psi(\vec{r})$ is wave function, $V(\vec{r})$ is the interaction potential which is the function of scattering length (*b*), $\vec{r}$ is the sample-to-detector distance and m is the mass. $E = \frac{\hbar^2 k^2}{2m}$, where $\hbar = \frac{h}{2\pi}$ is reduced Planck constant.

$$\frac{\hbar^2}{2m}(\nabla^2 + k^2)\Psi(\vec{r}) = V(\vec{r})\Psi(\vec{r}) \tag{2.16}$$

We rewrite the interaction potential as $V(\vec{r}) = \frac{\hbar^2}{2m}U(\vec{r})$, and we can simplify the equation as follow:

$$(\nabla^2 + k^2)\Psi(\vec{r}) = U(\vec{r})\Psi(\vec{r}) \tag{2.17}$$

We define a Green's-function by:

$$(\nabla^2 + k^2)G(\vec{r} - \overrightarrow{r'}) = \delta(\vec{r} - \overrightarrow{r'}) \tag{2.18}$$

A solution of Green's-function is given by:

$$G(\vec{r} - \overrightarrow{r'}) = -\frac{e^{ik|\vec{r} - \overrightarrow{r'}|}}{4\pi|\vec{r} - \overrightarrow{r'}|} \tag{2.19}$$

Using the solution of Green's function, we can write the general solution of wave function as:

$$\Psi(\vec{r}) = \Psi(\vec{r})_i + \int G(\vec{r} - \overrightarrow{r'})U(\overrightarrow{r'})\Psi(\overrightarrow{r'})d^3\overrightarrow{r'} \tag{2.20}$$

When we perform scattering experiments, the size of the sample is much smaller than both sample-to-source and sample-to-detector distances ($r \gg r', far\ field\ approximation$). The solution of Green's-function can be deduced as:

$$G(\vec{r} - \overrightarrow{r'}) = -\frac{e^{ikr} \cdot e^{-ik\frac{\vec{r}}{r}\overrightarrow{r'}}}{4\pi r} \tag{2.21}$$

$$\Psi(\vec{r})_i = e^{i\overrightarrow{k_i}\vec{r}}\ ,\ \overrightarrow{k_f} = k\frac{\vec{r}}{r} \tag{2.22}$$

$$\Psi(\vec{r}) = e^{i\overrightarrow{k_i}\vec{r}} + \left[-\frac{1}{4\pi}\int e^{-i\overrightarrow{k_f}\overrightarrow{r'}}U(\overrightarrow{r'})\Psi(\overrightarrow{r'})d^3\overrightarrow{r'}\right] \cdot \frac{e^{ikr}}{r} \tag{2.23}$$

The incident plane wave $\Psi(\vec{r})_i$ is superimposed by spherical waves emitted from scattering at the position $\overrightarrow{r'}$. The solution can be written as a plane wave plus a scattered spherical wave.

$$\Psi(\vec{r}) = \Psi(\vec{r})_i + f(\theta,\phi)\frac{e^{ikr}}{r} \tag{2.24}$$

The amplitude ($f(\theta,\phi)$) of these spherical waves is proportional to the interaction potential $V(\overrightarrow{r'})$ and the amplitude of the wave field at the position $\overrightarrow{r'}$. In order to obtain the total scattering amplitude, we have to integrate over the entire sample volume. The more fundamental problem is that normally the amplitude of scattered wave is not measurable. Instead only the scattered intensity can be determined ($I(\vec{Q}) \propto |f(\theta,\phi)|^2$). The phase information is lost which is the so-called phase problem of scattering. The relationship between the scattered intensity and structure of the sample is particularly simple in the so-called Born approximation.

$$\Psi(\vec{r})^0 = \Psi(\vec{r})_i = e^{i\overrightarrow{k_i}\vec{r}} \tag{2.25}$$

The incoming plane wave is not substantially altered by the potential.

$$\Psi(\vec{r})^1 = \Psi(\vec{r})_i + \int G(\vec{r}-\overrightarrow{r'})U(\overrightarrow{r'})\Psi(\overrightarrow{r'})^0 d^3\overrightarrow{r'} \tag{2.26}$$

$$\Psi(\vec{r})^1 = e^{i\overrightarrow{k_i}\vec{r}} + \left[-\frac{1}{4\pi}\int e^{i(\overrightarrow{k_i}-\overrightarrow{k_f})\overrightarrow{r'}}U(\overrightarrow{r'})d^3\overrightarrow{r'}\right]\cdot\frac{e^{ikr}}{r} \tag{2.27}$$

$$\Psi(\vec{r})^1 = e^{i\overrightarrow{k_i}\vec{r}} + \left[-\frac{1}{4\pi}\int e^{-i\vec{Q}\cdot\overrightarrow{r'}}U(\overrightarrow{r'})d^3\overrightarrow{r'}\right]\cdot\frac{e^{ikr}}{r} \tag{2.28}$$

The first Born approximation (BA) is obtained by substituting the $\Psi(\vec{r})^0$ in $\Psi(\vec{r})^1$equation, i.e. one assumes that the incoming wave scatters only once inside the target potential before forming the scattered wave.

$$\Psi(\vec{r})^{(n+1)} = \Psi(\vec{r})_i + \int G(\vec{r}-\overrightarrow{r'})U(\overrightarrow{r'})\Psi(\overrightarrow{r'})^n d^3\overrightarrow{r'} \tag{2.29}$$

In a similar manner, all higher order approximations can be calculated. This gives the so-called Born series. The BA is valid for large incident energies and weak scattering potentials.

2.3.2 Small angle scattering

Small angle scattering (SAS) is used as a tool to study morphology of our nanoparticles due to low Q-range accessible by this method (10^{-3} - 0.6 $Å^{-1}$). SAS is widely used for studies of biological materials, polymers, colloids, chemicals, nanocomposites, metals,

minerals, food and pharmaceuticals. In this thesis, SAS is used for the determination of the parameters of nanoparticles, such as size, shape and size distribution. The schematic of small angle scattering geometry is shown in Fig 2.7. In the transmission mode geometry, x-rays or neutrons are sent to the sample and scattered intensity is collected by 2D position-sensitive detector.

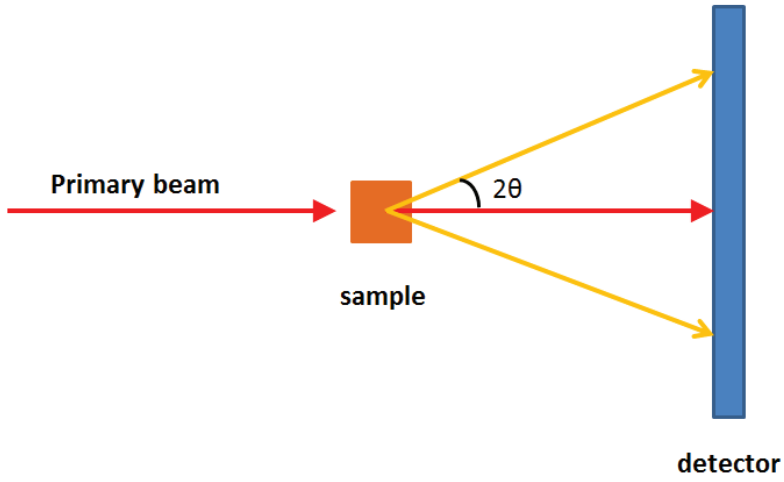

Fig. 2. 7 Small angle scattering geometry.

The scattering intensity of SAS is written as:

$$\mathrm{I}(\vec{Q}) \propto \mathrm{P}(\vec{Q})\mathrm{S}(\vec{Q}) \tag{2.30}$$

where $\mathrm{P}(\vec{Q})$ is form factor and $\mathrm{S}(\vec{Q})$ is the structure factor. The form factor is the Fourier transform of the scattering length density which is given by:

$$\mathrm{P}(\vec{Q}) = \left|\mathrm{F}(\vec{Q})\right|^2 = \left|\int \rho(\vec{r}) e^{-i\vec{Q}\cdot\vec{r}} d^3\vec{r}\right|^2 \tag{2.31}$$

where r is the radius of the nanoparticle and $\rho(\vec{r})$ is scattering length density of the nanoparticles. $\mathrm{P}(\vec{Q})$ is called the nanoparticle form factor which contains the shape and size information of nanoparticles. The structure factor is the Fourier transform of reciprocal space lattice which is written as:

$$\mathrm{S}(\vec{Q}) = \sum_{J=1}^{N} e^{-i\vec{Q}\cdot\vec{R_J}} \tag{2.32}$$

where $\overrightarrow{R_J}$ is the reciprocal lattice vector. The structure factor contains information about interaction between the particles. In case of non-interacting particles in a dilute solution the structure factor is equal to 1. The SAXS measurements were performed with well diluted nanoparticles solution.

While SAS is not sensitive to the atomic electron density variation, the scattering length density $\rho(\vec{r})$ can be approximated by a constant in nanoparticles. The $\rho(\vec{r})$ of the spherical nanoparticle with radius of R_0 can be expressed as:

$$\rho(\vec{r}) = \begin{cases} \rho, & |\vec{r}| \leq R_0 \\ 0, & |\vec{r}| > R_0 \end{cases} \tag{2.33}$$

In spherical coordinates (symmetric), we have $d^3\vec{r} = r^2 sin\theta d\theta \cdot d\phi \cdot dr$. In Cartesian coordinates, we have $d^3\vec{r} = dx \cdot dy \cdot dz$. By performing the integral in equation 2.31 above, we can get the form factor of a sphere and cubic nanoparticle:

$$F(\vec{Q})_{sphere} = \int \rho(\vec{r}) e^{-i\vec{Q}\cdot\vec{r}} d^3\vec{r} = \int_0^{2\pi} d\phi \int_{-1}^{1} sin\theta d\theta \int_0^R \rho e^{-i\overrightarrow{Q}\cdot\vec{r}} r^2 dr \tag{2.34}$$

$$F(\vec{Q})_{sphere} = \frac{4\pi R^3}{3} \rho \frac{3[\sin(QR) - QR\cos(QR)]}{(QR)^3} \tag{2.35}$$

$$F(\vec{Q})_{cubic} = \int \rho(\vec{r}) e^{-i\vec{Q}\cdot\vec{r}} d^3\vec{r} = \iiint \rho e^{-i\vec{Q}\cdot\vec{r}} dx \cdot dy \cdot dz \tag{2.36}$$

$$F(\vec{Q})_{cubic} = \frac{8\rho}{a^3 Q_X Q_Y Q_Z} \sin\frac{a}{2} Q_X \sin\frac{a}{2} Q_Y \sin\frac{a}{2} Q_Z \tag{2.37}$$

Where R is the radius of sphere and *a* is the edge length of a cube. The form factor is not only dependent on the shape of the particle, but also on its size. The calculated form factors for different size and shape of particle are shown in Fig. 2.8(a, b). Hence, the particle shape and size can be distinguished and obtained by SAS experiment.

For so-call monodisperse nanoparticles, all particles have the same size equal to the nominal radius. In reality, the size of a nanoparticle deviates from the nominal radius, i.e. particles are polydispersed. **The particle size distribution** needs be taken into account during analysis of SAS data. The form factors of individual nanoparticle are summed up to obtain the average scattering pattern over entire scattering volume. Because every size produces form factors with their minima at different scattering angles, the sum of all form factors will no longer contain well determined minima. In order to describe this effect, the standard Gaussian distribution was employed in SAS data analysis. The effect of size distribution on the scattering pattern is simulated in Fig. 2.8(c). It clearly shows how the form factor minima are smearing out with increase of the polydispersity. The actual small angle x-ray scattering (SAXS) data (Fig. 2.8(d)) of average radius of

7.8 nm nanoparticles confirms the effect of the size distribution on the scattering pattern. We also note that in experiment smearing is due to the finite instrument resolution which will be taken into account during the data analysis.

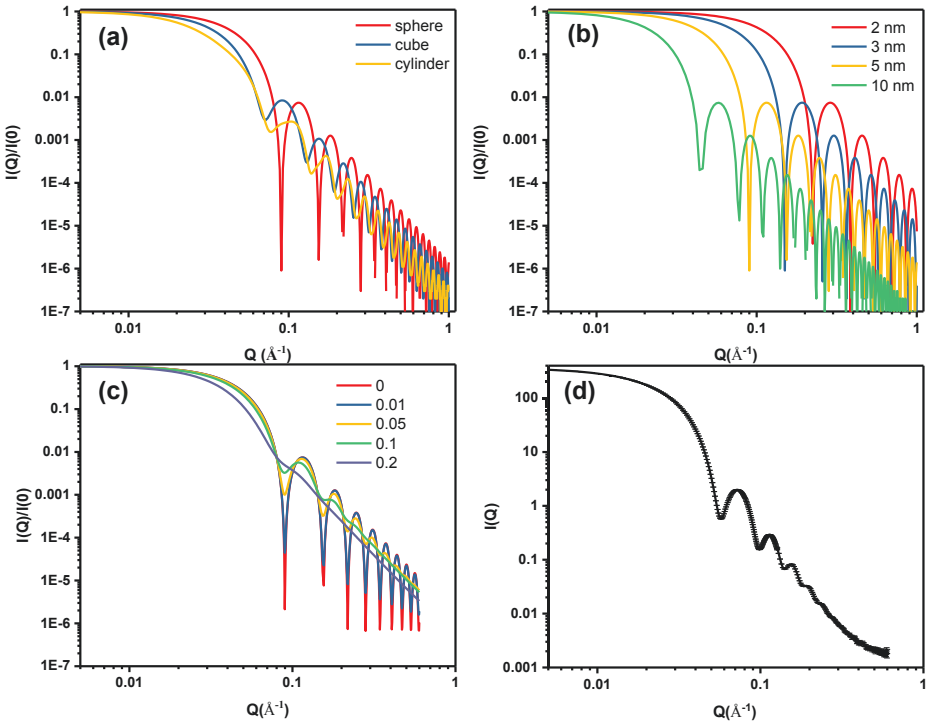

Fig. 2. 8 (a) The calculated form factor of sphere (R = 5 nm), cube (a =10 nm) and cylinder (R = 5 nm, h=10 nm). (b) The calculated form factor of a sphere with different radius. (c) The calculated form factor of the spherical particles with varying degree of polydispersity (σ/R= 0, 0.01, 0.05, 0.1 and 0.2). (d) Experimental SAXS data of the spherical nanoparticles with an average radius of 7.8 nm

2.3.3 Scattering under grazing incidence

The scattering under grazing incidence geometries is used instead of transmission SAS to characterize nanoparticles deposited on a substrate. When incident angle of the incoming beam is extremely small (blow 1°), it makes a large footprint on the sample surface. The scattering geometry for the grazing incidence scattering is presented in Figure 2.10. The incoming beam enters the sample under a shallow angle α_i, and the scattered beam is determined by specifying two angles for the in-plane component $2\theta_f$

and out of plane component α_f. The components of the scattering vector $\vec{Q}$ are thus given by:

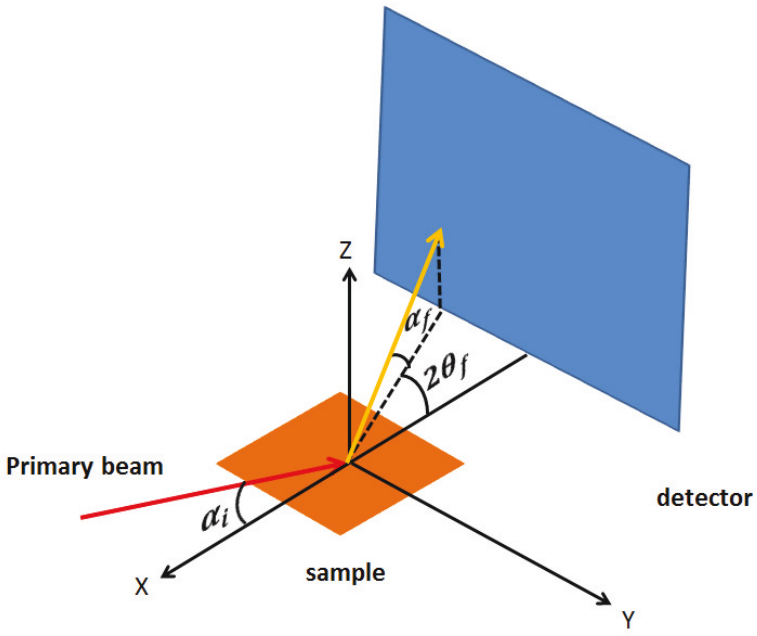

Fig. 2. 9 Sketch of the grazing incidence scattering geometry of the principle scattering setup. α_i and α_f are incident and exit angles in the scattering plane. $2\theta_f$ is the in-plane angle between incident and scattered wave vector.

$$\vec{Q} = \overrightarrow{k_f} - \overrightarrow{k_i} = \begin{pmatrix} Q_x \\ Q_y \\ Q_z \end{pmatrix} = k \begin{pmatrix} \cos\alpha_f \cos 2\theta_f - \cos\alpha_i \\ \cos\alpha_f \sin 2\theta_f \\ \sin\alpha_f + \sin\alpha_i \end{pmatrix} \tag{2.38}$$

There are several scattering methods under grazing incidence angles. In the following section, the specular/off-specular reflectivity and grazing incidence small angle scattering will be introduced.

2.3.2.1 The specular and off-specular reflectivity

The reflectometry techniques are important tools in the characterization of nanoscale structured interfaces on the size range from 1 up to ~5000 Å. In the reflection geometry, a tightly collimated beam is directed at the sample surface under study, with an incident angle α_i (Fig. 2.9). The specular reflectivity provides only the information along the z-

component of Q vector at $\alpha_i = \alpha_f$ and $2\theta_f = 0$. The scattering vector reduces to $Q_z = \frac{4\pi}{\lambda} sin\,\alpha_i$. The data is typically plotted as a function of the momentum transfer (Q_z) perpendicular to the surface of a film. When the incident beam impinges on an interface, which is located between two different materials with different refractive index ($n(\lambda) = 1 - \delta(\lambda) + i\beta(\lambda)$), the beam will split into transmitted and reflected beams. The Snell's law ($n_1 \cos\theta_i = n_2\, cos\,\theta_t$) is used to describe the relationship between the angles of incidence and refraction at the interface between two different materials as shown in Fig. 2.10(a). Because the refractive index is below 1 for most of the materials, a total external reflection occurs when the incident angle α_i is smaller than the critical angle α_c. The critical angle can be calculated from the dispersion part δ of the refractive index or scattering length density (SLD) ρ of the material as:

$$\alpha_c(\lambda) = \sqrt{2\delta(\lambda)} = \lambda\sqrt{\frac{\rho}{\pi}} \tag{2.39}$$

At low incident angles, the normalized intensity is close to unity as the total reflection condition is fulfilled ($\alpha_i < \alpha_c$). The reflectivity starts rapidly decreasing above the critical angles of materials. For $\alpha_i > \alpha_c$, the reflectivity curve falls off rapidly with a decay of Q_z^{-4} (for a single interface). The Fresnel equations (or Fresnel coefficients) describe the ratios of the amplitudes of reflected and transmitted beam, when incident on an interface between different media. E_i stands for the amplitude of the wave of the incident beam. E_r and E_t are the amplitudes for the reflected and transmitted beams. The amplitude coefficients of reflection and transmission, *r* and *t*, are defined as:

$$r = \frac{E_r}{E_i}, t = \frac{E_t}{E_i} \tag{2.40}$$

If the incident and reflected beams are travelling in same media, the reflectivity R is defined by the modulus of the corresponding amplitudes. When the incident beam and transmitted beams are in different media with different refractive index, the transmissivity T is proportional to t^2.

$$R = |r|^2, T = \frac{n_2\, cos\,\theta_t}{n_1\, cos\,\theta_i}|t|^2 \tag{2.41}$$

$$T + R = 1 \tag{2.42}$$

Two calculated specular reflectivity curves for monolayer of Fe and Fe-Si multilayer are displayed in Figure 2.10(b). For $\alpha_i > \alpha_c$, the reflectivity intensity decreases and so-called Kiessig fringes are observed due to interference effects. The width of the Kiessig fringes is correlated with the film thickness d_{film}. Therefore, the total film thickness can be approximated by:

$$d_{film} = \frac{2\pi}{\Delta Q_{Kiessig}} \tag{2.43}$$

where $\Delta Q_{Kiessig}$ is the distance between two neighboring minima of the Kiessig fringes at higher angles (where refraction can be neglected). For the multilayer sample, Bragg reflections are observed as additional features, which provide the information about a single multilayer repetition thickness.

$$d_{repetition} = \frac{2\pi}{\Delta Q_{Bragg}} \tag{2.44}$$

$$d_{film} = N * d_{repetition} \tag{2.45}$$

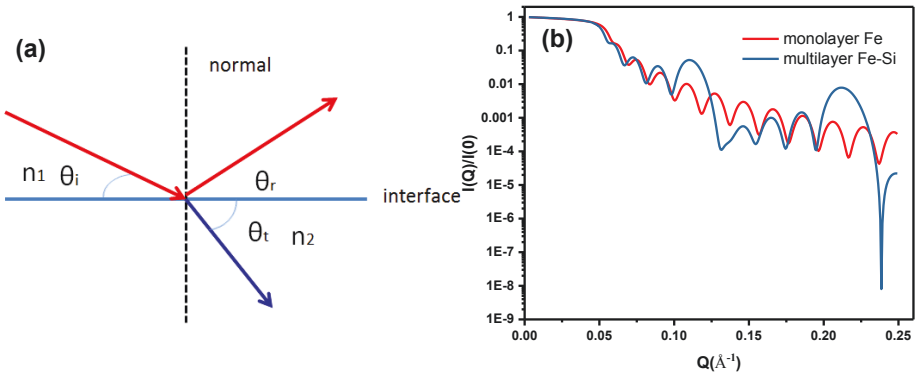

Fig. 2. 10 (a) Variables used in the Snell law and Fresnel equations. (b)The calculated specular reflectivity curves of a Fe monolayer of 30 nm thickness and a Fe-Si multilayer of 6 nm with 5 repetitions.

Consequently, a number of N repetition of the multilayer unit leads to (N-2) Kiessig fringes in between two Bragg reflections. For an accurate determination of the sample thickness, the roughness of interface between two materials needs be taken account. The Kiessig fringes are damping by the interface roughness and finite instrument resolution.

For the off-specular reflectivity ($\alpha_i \neq \alpha_f$ and $2\theta_f = 0$), the scattering vector is

$$Q_x = \frac{2\pi}{\lambda}(cos\,\alpha_f - cos\;\alpha_i) \tag{2.46}$$

$$Q_z = \frac{2\pi}{\lambda}(sin\,\alpha_f + sin\,\alpha_i) \tag{2.47}$$

Compared to specular reflectivity, lateral correlations of a sample along Q_X contribute to the additional intensity in the off-specular reflectivity. Thus, the off-specular reflectivity can provide a depth-resolved information on the lateral structures.

2.3.2.2 Grazing incidence small angle scattering

The grazing incidence small angle scattering (GISAS) has developed as an advanced thin film characterization method that enabled the detection of the 3D film morphology. GISAS usually requires a 2D position-sensitive detector to collect the intensities at $\alpha_i \neq \alpha_f$ and $2\theta_f \neq 0$. Taking into acount of the smallness of those three angles, the scattering vector in GISAS geometry is given by:

$$\vec{Q} = \overrightarrow{k_f} - \overrightarrow{k_i} = \begin{pmatrix} Q_x \\ Q_y \\ Q_z \end{pmatrix} = k \begin{pmatrix} \left[{\alpha_i}^2 - {\alpha_f}^2 - \left(2\theta_f\right)^2 \right]/2 \\ 2\theta_f \\ \alpha_f + \alpha_i \end{pmatrix} \tag{2.48}$$

The scattering vector provides the structural information about the sample in x, y and z directions. This makes GISAS a very powerful tool for characterization of self-assembled structures on the structured surfaces. If we study thin film samples in transmission geometry, the reduced scattering volume provides only limited information about sample structure. By switching the transmission geometry to a reflection geometry using grazing angles, the scattering volume is enlarged and structures on the film surface can be probed. A shallow incident angle of typically $\alpha_i < 1^\circ$ is normally used in GISAS experiments. The beam is projected into a long stripe over the sample surface (e.g. a 500 µm beam at 1° incidence is projected to 28 mm). Due to the small angles in GISAS geometry the 2D detector probes the sample information mainly in the Q_y and Q_z direction, because $Q_x \ll Q_y, Q_z$. Putting some more clear figures in equation 2.48 leads to $\lambda = 1.34\,\text{Å}$, $\alpha_i = \alpha_f = 0.2^o$, $\theta_f = 0.5^o$ to $Q_x = 0.07 \times 10^{-2}\,\text{Å}^{-1}$, $Q_y = 0.08\,\text{Å}^{-1}$, $and\ Q_z = 0.03\,\text{Å}^{-1}$. It is easy to tell Q_x is two orders of magnitude smaller than $Q_y\ and\ Q_z$.

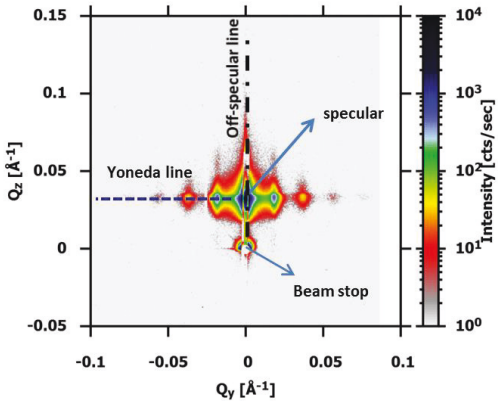

Fig. 2. 11 A typical example of GISAXS data. The color visualizes differences in the scattered intensity.

The characteristic GISAXS data for 2D self-assembly nanoparticles is shown in Fig. 2.11. Due to the high intensity of the direct beam, it is always shielded with a beam stop. The specular peak, appearing at $\alpha_i = \alpha_f$ following the law of reflection, can become so intense that it needs to be blocked with a point-shaped beam stop or even a rod-shaped beam stop. The purpose of the beam stop is to block all scattering along the off-specular line in order to protect 2D detector from oversaturation and at the same time increase the contrast in the data. An additional characteristic feature of GISAS is the so-called Yoneda line ($\alpha_f = \alpha_c$) arising at the critical angle of the film [23]. Because there is no out of plane scattering contained in Q_y component, we can simply apply Bragg's law in Yoneda line without any correction.

In the case of incident angle close to and below the critical angle, one cannot ignore multiple scattering. For the weak multiple scattering the Born Approximation is no longer applicable. The refraction effects need to be taken into account, because the wave vectors inside the film differ from those in the vacuum. Moreover, the reflection at the film-substrate interface needs to be considered in the grazing incidence geometry. The Distorted-Wave Born Approximation (DWBA) takes into account that the incident and reflected waves interfere to form a standing wave [24]. The standing wave then serves as the reference wave, which scatters from the nanostructures on the substrate. The DWBA has to be applied for a quantitative evaluation of the GISAS intensities. In the frame of the DWBA model, the potential can be split into two parts:

$$U(\vec{r}) = U_1(\vec{r}) + \delta[U(\vec{r})] \text{ with } |\delta[U(\vec{r})]| \ll |U_1(\vec{r})| \quad (2.49)$$

And $U(\vec{r})$ is treated as a perturbation $\delta[U(\vec{r})]$ to the reference system $U_1(\vec{r})$ that can be solved by some other method. The "distorted" wave (due to $U_1(\vec{r})$) is written based on the equation 2.18:

$$\Psi_1(\vec{r}) = \Psi(\vec{r})_i + \int G_0\left(\vec{r} - \overrightarrow{r'}\right) U_1\left(\overrightarrow{r'}\right) \Psi_1\left(\overrightarrow{r'}\right) d^3\overrightarrow{r'} \tag{2.50}$$

$\Psi_1(\vec{r})$ will work as incident wave and be perturbed by $\delta[U(\vec{r})]$. By applying Born approximation, the $\Psi(\vec{r})$ is calculated as:

$$\Psi(\vec{r}) = \Psi_1(\vec{r}) + \int G_1\left(\vec{r} - \overrightarrow{r'}\right) \delta[U(\vec{r})] \Psi_1(\vec{r}) d^3\overrightarrow{r'} \tag{2.51}$$

The diffuse scattering in GISAS is described by DWBA, which includes four terms of both scattering and reflection processes: (1) only scattering from density fluctuations; (2) scattering followed by reflection on the substrate; (3) reflection on the substrate followed by scattering and (4) first reflection on the substrate, then scattering, and followed by another reflection on the substrate.

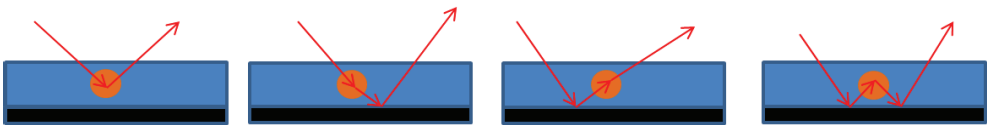

Fig. 2. 12 Possible scattering paths under grazing incidence used in DWBA model.

The open source software package named BornAgain [25] was used to simulate and fit scattering data of X-rays and neutrons in GISAS geometry using DWBA formalism.

2.3.4 Polarized Neutrons

Because the neutron has a magnetic moment (spin (± 1/2)), it will also interact with magnetic moments in the sample or with magnetic field. Polarized neutron scattering is used to separate the nuclear scattering and magnetic scattering. This section will give a simple introduction in the spin dependence of neutron scattering. Polarizers and analyzers are required to manipulate and detect the neutron spin. The polarizer is to polarize the initially beam by absorbing the unwanted spin state or selective reflection. The polarization of a polarized neutron beam (P) is defined by the number of neutrons with spin up ($n_\uparrow$) and down ($n_\downarrow$) states as:

$$\mathrm{P} = \frac{n_\uparrow - n_\downarrow}{n_\uparrow + n_\downarrow} \tag{2.52}$$

The analyzer is located between the sample and the detector to analyze the polarization of the scattered beam. The detector can count the neutron reached on the detector no matter which spin state it is. With the help of the analyzer that only allows the neutron

with specific direction to pass through, different spin states neutron can be detected. Spin flipper is the device to modify the spin direction. π-flipper can rotate 180 ◦ of the spin direction. Combining polarizer, analyzer and flipper, four different scattering channels can be obtained: Non spin-flip: ↑↑, ↓↓. and Spin-flip: ↑↓, ↓↑. M is the Fourier transform of the real space magnetization density. The components of any magnetic dipole field parallel ($\mathrm{M}_Q^{\parallel}$) to the scattering vector will cancel out and only the components perpendicular ($\mathrm{M}_Q^{\perp}$) to the Q are observable (Fig. 2.13 (a) and (b)). The neutron polarization component may change after scattered by a magnetic dipole as shown in Fig. 2.13(c). The component of P parallel to $\mathrm{M}_Q^{\perp}$ remains unchanged while the component of P perpendicular to $\mathrm{M}_Q^{\perp}$ reverses its sign.

When we perform polarized neutron measurements, we chose P ∥ y-axis and Q ∥ z-axis. Considering all possibilities for neutron spin state before and after the scattering process, and by decomposing $\mathrm{M}_Q^{\perp}$ in its components we obtain magnetic scattering amplitude [21]:

$$\mathrm{A(Q)} = -\frac{\gamma_n r_0}{2\mu_B}\begin{cases} \mathrm{M}_{Q_y}^{\perp} & (\uparrow\uparrow) \\ -\mathrm{M}_{Q_x}^{\perp} & (\uparrow\downarrow) \\ \mathrm{M}_{Q_x}^{\perp} & (\downarrow\uparrow) \\ -\mathrm{M}_{Q_y}^{\perp} & (\downarrow\downarrow) \end{cases} \tag{2.53}$$

where γ_n is the gyromagnetic factor for the neutron and r_0 is the classical electron radius. However, the z component cannot be measured because the Q is parallel to z-axis. Different scattering components can be separated by analyzing the data from different channels.

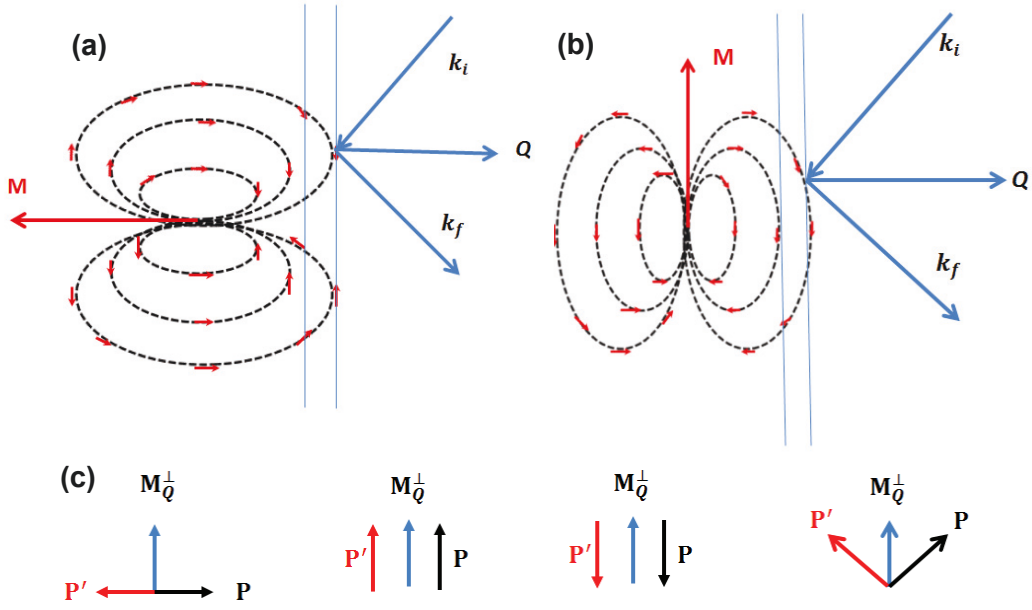

Fig. 2. 13 The magnetic field line configuration for M parallel (a) and perpendicular (b) to the scattering vector *Q*. For $\mathbf{M} \parallel \boldsymbol{Q}$, magnetic dipole field amplitudes show destructive interference, for $\mathbf{M} \perp \boldsymbol{Q}$ constructive interference. (c) Change of initial polarization P to final polarization P': the component perpendicular to $\mathbf{M}_Q^\perp$ reverses sign, the parallel component of P is invariant.

Chapter 3 Experimental methods and instruments

In this chapter, the methods and instruments used to prepare samples and investigate the complex assemblies are described. Two self-assembly systems with nanoparticles in different dimensional structure are fully characterized with a variety of techniques. Microscopy techniques characterize the morphology of nanoparticles in real space. For example, Scanning Electron Microscopy (SEM) provides information about the 2D self-assembly of nanoparticles on the surface of the substrate on scale of 10 μm^2. Transmission Electron Microscopy (TEM) provides structural information about nanoparticles on atomic scale. Both methods can give information about the size, size distribution and the shape of single particles. Atomic Force Microscopy (AFM) is used to obtain the surface height profile and phase images of the samples as well as to independently check the 2D self-assembled nanoparticles structure, providing complementary information to SEM data. AFM phase image is an important tool for the structural characterization of nanocomposite film. These methods give a local view on the 2D self-assembly and 3D nanocomposite film surface structures in real space and yield important sample parameters such as the center-to-center distance between two nanoparticles.

Scattering methods are used to obtain the average correlations on a large sample area with depth resolution. A depth resolved structural characterization over a large sample area can be achieved with X-ray and neutron scattering experiments. For this work, a study of the morphology and size distribution of nanoparticles in a solution was done with Small Angle X-ray Scattering (SAXS). 2D self-assembly of nanoparticles and 3D nanocomposite film were investigated by Grazing Incidence Small Angle X-ray Scattering (GISAXS) in either lateral or specular directions, giving the information about the structure of the samples. Magnetic structure and magnetic correlations in our samples were investigated by using Polarized Neutron Reflectometry (PNR) and Grazing Incidence Small Angle Neutron Scattering (GISANS) methods. In contrast to x-rays, polarized neutrons are able to probe the magnetic structure and magnetic correlations between magnetic nanoparticles. PNR can give us the nuclear and magnetic Scattering Length Density (SLD) information of nanocomposite film. BornAgain software was used to model both experimental x-ray and neutron scattering data [1]. The magnetic properties were probed with a magnetic property measurement system (DynaCool). All the information about instruments presented here is taken from the referenced websites and publications.

3.1 Scanning Electron Microscopy (SEM)

The SEM operates in the reflection mode, scanning a focused electron beam over the sample and measuring the flux of scattered electrons to create an image. SEM can provide a higher resolution due to the wavelength electrons which is much smaller than the wavelength of light. The accelerated electrons hit the sample surface and cause the emission of signals from of the material being hit. These signals include secondary electrons, low-angle backscattered electrons and high-angle backscattered electrons, which are acquired for observation of the surface structures. Depending on different examined materials and their topography, a monochrome SEM image with corresponding brightness values can be obtained with a penetration depth of about 10 nm. The image contains information about the topography as well as about the material composition, because electron interaction is element dependent. In the present thesis, all SEM images were collected from a Field Emission Scanning Electron Microscope SU8000 (HITACHI). The SU8000 features a top detector along with a semi-in-lens type of objective lens and also includes an upper detector, which provides highly efficient SE signal detection. Because of the poor electrical conductivity of the organic shell around the nanoparticles, it can easily be charged up in a short time. In order to achieve higher resolution and avoid oversaturated charging for SEM images, acceleration voltages of 3 or 5 kV at working sample-detector-distance of 8 mm were used. Only the upper detector has been used during all measurements. This method allowed us to obtain a first surface sensitive characterization of the sample and access its quality without destroying or cutting the sample. The same samples were used for further neutron scattering measurements where intact and large sample sizes were required.

3.2 Transmission Electron Microscopy (TEM)

TEM uses a highly coherent electron beam that passes through a thin, electron transparent specimen. The transmitted electron beam can be used to record images in the real space or take diffraction patterns in the reciprocal space. In our study, an FEI Tecnai G2 F20 microscope was used to reveal essential information about the size and morphology of the single nanoparticle on a nanoscale. The TEM operates at 200 kV accelerating voltage and it is equipped with a thermal (Schottky) field-emission gun. The microscope objective lens is the FEI Tecnai “Super Twin” lens type and the spherical aberration coefficient Cs = 1.2 mm permits a CTEM point resolution of 2.4 Å. The specimens were prepared from drop casting of a low concentrated nanoparticles suspension onto a carbon- coated copper grid.

3.3 Atomic Force Microscopy (AFM)

AFM is a highly surface sensitive technique that allows us to see and measure surface structure with unprecedented resolution and accuracy. In this work, all AFM images were taken in a standard tapping mode in air. Tapping mode operates by scanning a tip attached to the end of an oscillating cantilever that lightly 'taps' the surface only for a short time during scanning, thus avoiding the issue of lateral forces and drag across the surface. The cantilever is oscillating at or slightly below its resonance frequency. The tip-to-sample distance is changed by Z-piezo to maintain at the chosen cantilever amplitude without changing the drive frequency. Typical amplitudes of oscillation are in the range of tens of nanometers, and thus very small compared to the cantilever length (~ 100 μm). When the probe approaches the sample, it experiences an attractive force (van-der-Waals interaction) and is pulled toward the surface until contact is made. From that point on, the repulsive interaction forces (Coulomb interaction) dominate the response. The force curve is shown in Figure 3.1. The probe can then be retracted and additional information can be extracted from that trace. And the movement of the Z-piezo when plotted as a function of (x, y) becomes the sample topography. This mode has advantages of obtaining high resolution images of easily damaged or stick surface samples. For this study a Bruker MultiMode8 AFM was used. The possible lateral resolution is mainly determined by tip shape and size. For a higher resolution a sharper tip is required. A cantilever with 8 nm tip radius is used at 300 kHz (RTESPA-300, Bruker Nano Inc.) The NanoScopeAnalysis software was used to apply filter commands to correct images and analysis functions to get Fourier transformation, 2D or 3D images.

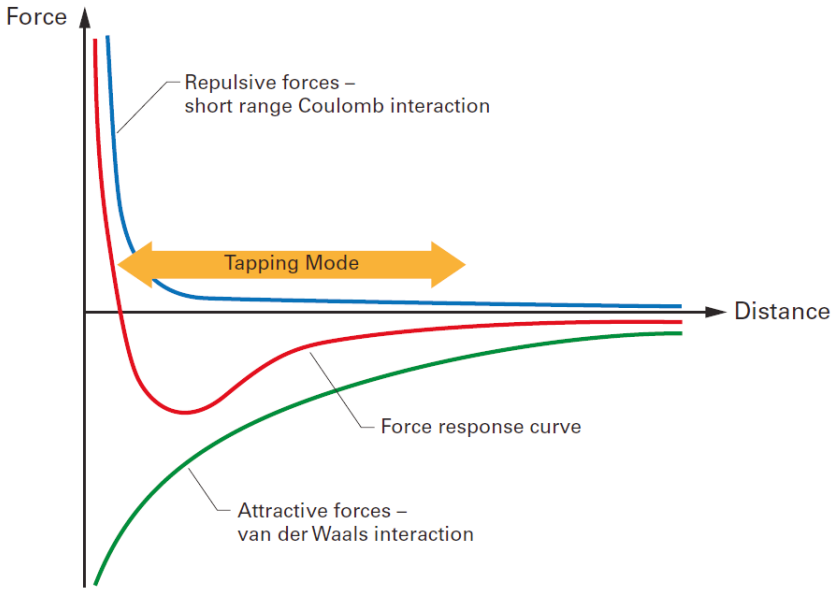

Fig. 3. 1 Force curve highlighting the motion of an oscillating cantilever in TappingMode.

3.4 Gallium Anode Low-Angle X-ray Instrument (GALAXI)

GALAXI is high brilliance laboratory small angle X-ray scattering instrument at Jülich Centre for Neutron Science (JCNS), Forschungszentrum Jülich. GALAXI was designed for x-ray scattering studies of chemical correlations in bulk materials and of structures deposited on a surface at nanometer and mesoscopic length scales [2]. The instrument is capable of performing GISAXS experiments in reflection mode at grazing incidence, as well as SAXS experiments in transmission geometry. Fig. 3.2 shows the main components of GALAXI. Metaljet source is used to produce x-ray radiation. An electron beam hits the liquid metal jet, which is composed of a GaInSn alloy, and x-rays of wavelength λ = 0.134 nm are produced. The x-ray beam with 0.3 mrad divergence has a flux of 10^9 photons/mm^2·s at the sample position. It is comparable or even higher than the flux obtained at a comparable beamline on the second generation synchrotron x-ray source. The x-rays from the source are guided through a vacuum system to the sample by the use of various slits to achieve a monochromatic and sufficiently collimated/focused beam. Using two slits S1 and S2 separated by 4 m distance, the x-ray beam can be collimated with an inclination of 0.4 °. After that, a third slit S3 is used to reduce the background. The beam size can be adjusted by the last set of slits in front

of the sample position. The optimized S3 slit size provides a well collimated beam with the size 0.7 x 0.7 mm^2. The scattered photons are detected by a Pilatus 1M 2D position sensitive detector with 169 x 179 mm^2 active area. Two translation and two rotation motors are installed to align the sample and change the angle of incidence. Different Q-ranges can be probed by changing the detector distance between 0.8 to 3.5 m in 5 steps, and thus structures between 2 and 100 nm sizes can be studied.

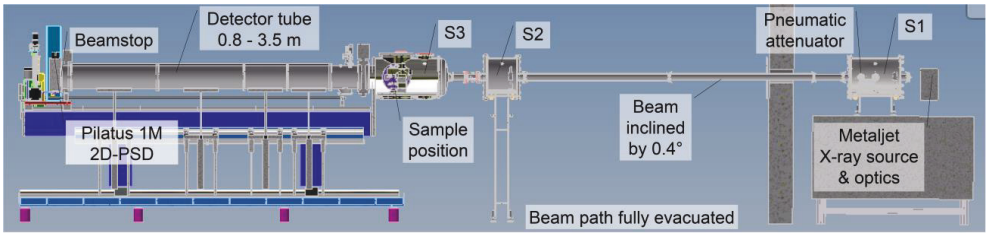

Fig. 3. 2 Schematic drawing of GALAXI with its main components. The beam direction is from right to left. Taken from [2].

SAXS was employed to give information of the averaged size, size distribution and particle shape. For SAXS measurements, which use transmission geometry as shown in Fig 3.3 (a), the nanoparticles are diluted in a solvent and sealed in a glass or quartz capillary. The 1D SAXS profiles were fitted by using SasView software package [3]. The fluorinated ethylene propylene (FEP) was used as a reference sample to calibrate the x-ray flux.

GISAXS was used to determine structures of the assemblies in the nanometer range. A schematic view of the GISAXS geometry is shown in Figure 3.3 (b). In this measurement geometry, average information over a large sample area can be collected as a beam footprint cross the sample surface. The incident angle (α_i) was set to 0.18 °, which was well above the total reflection angles (critical angles) of nanocomposite film and below the total reflection angles (critical angles) of substrates, so that the x-ray beam was penetrating the entire films. Thus, the data collected in this geometry contain the information throughout the full depth of the nanocomposite film. The strong primary beam and specularly reflected beam in GISAXS experiments can damage or saturate the detector. In order to diminish those effects the round beam stop to shield the primary beam and a long, rectangular shaped Si beam stop to shield reflected beam were used during the experiments. The reference sample silver behenate (AgBH) was used to calibrate the accurate sample-to-detector distance.

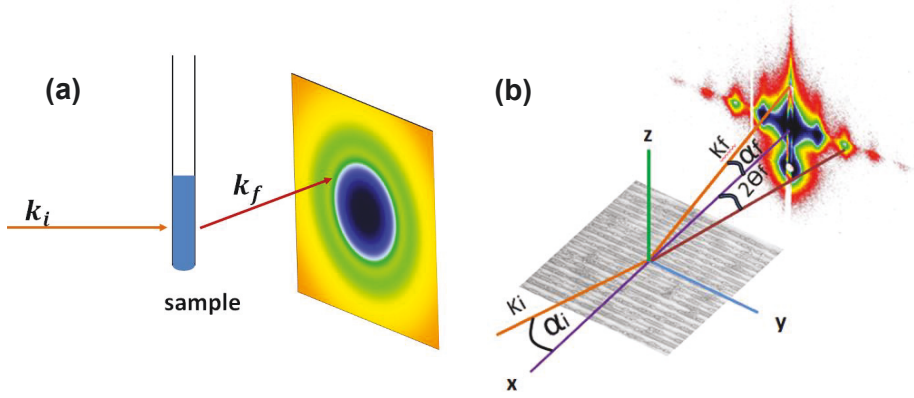

Fig. 3. 3 The schematic view of the (a) SAXS and (b) GISAXS geometry. The x-ray impinges on the sample with a shallow incident angle (α_i), and an exit beam with an angle of α_f is recorded on a 2D detector.

3.5 MARIA@MLZ

MARIA is the neutron reflectometer with polarisation analysis, which is operated by JCNS at MLZ in Garching. It was designed for the investigation of thin magnetic layered structures down to the monolayer scale and lateral structures [4]. Along with the reflectometer mode in the horizontal scattering plane, MARIA can be used in the GISANS mode with additional resolution in the vertical direction. Such design allows the GISANS, reflectivity and Off-specular scattering measurements with polarized neutrons just at one instrument. The schematic illustration of MARIA is shown in Figure 3.4. The instrument is optimized for the measurements of 1 x 1 cm samples with small focused beam at λ = 4.5 Å in a vertical orientation with a maximum incident angle of 180° and outgoing detection angle ranging from -14° to 100°. MARIA is equipped with a velocity selector with a wavelength resolution of $\Delta\lambda/\lambda$ = 10% and with a vertically focusing guide. MARIA provides polarisation analysis in standard operation mode, where the beam is polarised by a polarising guide (z-geometry; 4.5 Å < λ < 10 Å) and analysed by a wide angle ^{3}He-cell. The main instrument parameters of MARIA are listed in Table 3.1. At the sample position, a hexapod with an additional turntable (360°) is installed, which can take a load up to 500 kg. In the standard configuration magnetic fields are provided up to 1.3 T (Bruker electromagnet) and cryogenic temperatures down to 4 K (He closed cycle cryostat).

MARIA was used to perform GISANS and PNR measurements of nanocomposite film and GISANS of 2D nanoparticles self-assembly. In order to avoid background due to incoherent scattering from hydrogen, deuterated block copolymer was used for the

sample preparation. All measurements were performed at different field with λ = 6 Å. This wavelength was chosen as an optimum compromise between sufficient resolution and high enough neutron flux.

Table 3. 1 Main Instrument parameters of MARIA.

Resolution	10 %
Wavelength	4.5 Å < λ < 10 Å
Polarized flux	5 x 10^7 n · cm^{-2} · s^{-1}
Optimal sample size	10 x 10 mm^2
Reflectometry Q-range	Qz： 0.002 $Å^{-1}$ – 3.2 $Å^{-1}$, Qx： 6 x 10^{-5} $Å^{-1}$ – 0.001 $Å^{-1}$
GISANS Q-range	0.002 $Å^{-1}$ – 0.2 $Å^{-1}$

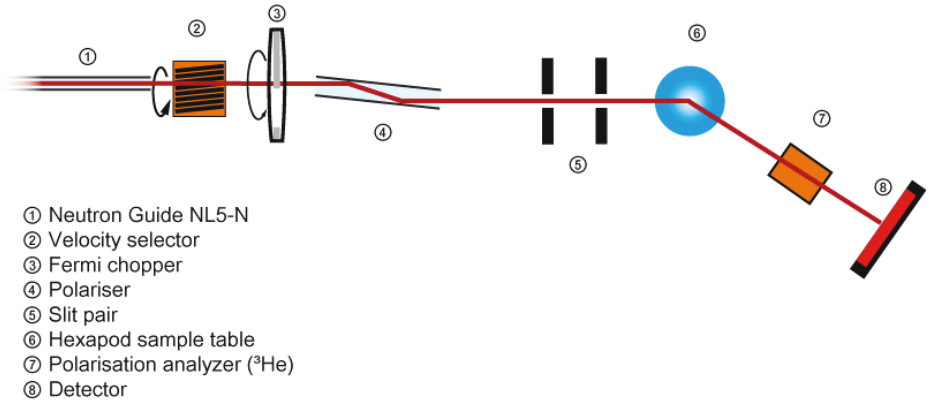

Fig. 3. 4 Schematic drawing of MARIA. Taken from [4].

3.6 Magnetometer

The macroscopic magnetization of 2D nanoparticles self-assembly and nanocomposite film systems have been studied using a vibrating sample magnetometer (VSM) option mounted on DynaCool (Quantum Design). The DynaCool consists of the following main components: cryostat assembly, CAN Module bay, pump cabinet, computer, cryocooler compressor assembly and Helium gas bottle and regulator. The system uses a single, two-stage pulse tube cryocooler for both the superconducting magnet and the temperature control system, providing an efficient, low vibration environment for sample measurements that simultaneously provides lower maintenance costs. The DynaCool equipped with a 9 T superconducting magnet for measurements in the temperature range 1.8 K to 400 K.

The VSM option consists primarily of a VSM linear motor transport (head), a coilset puck and pickup coils. The basic measurement is accomplished by oscillating the sample near a pickup coil and synchronously detecting the voltage induced. By using a compact gradiometer pickup coil configuration, a relatively large oscillation amplitude (1–3 mm peak) and a frequency of 40 Hz, the system is able to resolve magnetization changes of less than 10^{-6} emu at a data rate of 1 Hz. More details about the VSM can be found in the Vibrating Sample Magnetometer (VSM) Option User's Manual. The sample is cut into 5 x 5 mm^2 and is inserted inside a special sample holder, which has very low background. In the data analysis, a strong diamagnetic contribution originating from the Sapphire substrate was subtracted. Important magnetic characterizations of the investigated nanoparticles and nanocomposite film, including magnetization saturation, remanence and coercivity, were extracted from the measured magnetic moments.

Chapter 4 Iron oxide nanoparticles and sapphire substrate

4.1 Iron Oxide Nanoparticles

Magnetic nanoparticles have been studied for many years because of their many applications, such as magnetic storage media [1], magnetic separation [2], drug delivery and permanent magnetic nanocomposites [3]. The finite size effect and high surface area-to-volume ratio are main properties that give rise to many applications in those fields. In this work, we also investigated the particles of two different sizes: 5 nm and 28 nm.

The spherical 5 nm iron oxide nanoparticles (ON5) were bought from Ocean NanoTech [4] and were used in our 3D nanocomposite films. This specific size was chosen to match the structure of the nanocomposite film. Prior to applications in the film, nanoparticles were dispersed in chloroform ($CHCl_3$) at the concentration of 25 mg/ml.

The cubic iron oxide nanoparticles (28 nm, NP28) used for 2D self-assembly were dispersed in n-hexane (C_6H_{14}). The size of NP28 will determine which substrate we can use. The samples were obtained from the group of Marina Spasova at University of Duisburg-Essen [5]. The synthesis of the NP28 was carried out through decomposition of a preformed iron oleate complex at high temperature. The method relies on the original paper by Park and co-workers [4], but with a careful choice of solvent (squalene ($C_{30}H_{50}$)) and using the presence of remaining sodium oleate ($C_{18}H_{33}NaO_2$) to induce formation of cubes, rather than spheres [5].

This section will provide a description of structural properties of several iron oxide nanoparticles with a focus on their morphological characterization. The information about particle shape, size and size distribution was obtained. Moreover, magnetic properties of the stand-alone ON5 and NP28 samples were determined.

4.1.1 Characterization

TEM images were obtained using a FEI Tecnai G2 F20 microscope operated at 200 kV. The specimens were prepared by depositing a drop of a dilute dispersion of nanoparticles on carbon-coated copper grids and allowing the solvent to evaporate rapidly.

Small-angle X-ray scattering (SAXS) measurements were performed on the GALAXI instrument at Jülich Centre for Neutron Science (JCNS). The Pilatus 1M detector [8] with 981 x 1043 pixels of 0.172 mm pixel size was set up at distances of 830 and 3530 mm from the sample position. The wavelength was 1.34 Å. The beam size was set to 0.7 x 0.7 mm. ON5 nanoparticles were dried first and were redispersed in toluene for 0.1 vol % concentration. NP28 nanoparticles were dispersed in n-hexane with 0.1 vol % concentration. The fluorinated ethylene propylene (FEP) was used as a reference sample to calibrate the x-ray flux. All measurements were carried out in vacuum.

The magnetic measurements using a Quantum Designs Physical Property Measuring System (PPMS-dynacool) equipped with a superconducting magnet and a vibrating sample magnetometer (VSM) option, were carried out on a small amount (ca. 5 µl) of a chloroform dispersion dried on silicon wafer with a concentration of ca. 25 mg/ml of nanoparticles. The M-H curves were measured using a maximum field of 5 T.

4.1.2 Results and Discussion

4.1.2.1 TEM data

The shape, mean size and the size distribution of the NPs have been characterized by TEM. Fig. 4.1 (a) shows TEM image of ON5. The nanoparticles are of spherical shape with an average diameter of 5.5 nm. The size distribution histogram of NPs was estimated from counting of 100 individual particles. The estimated polydispersity (PD) was 0.09 σ/D, where σ is a standard deviation and D is the diameter of a particle. We approximated the round corner cubic nanoparticles (Fig. 4.1(b)), with a simpler spherical shape and estimated the average diameter of 28.2 nm and the PD of 0.08.

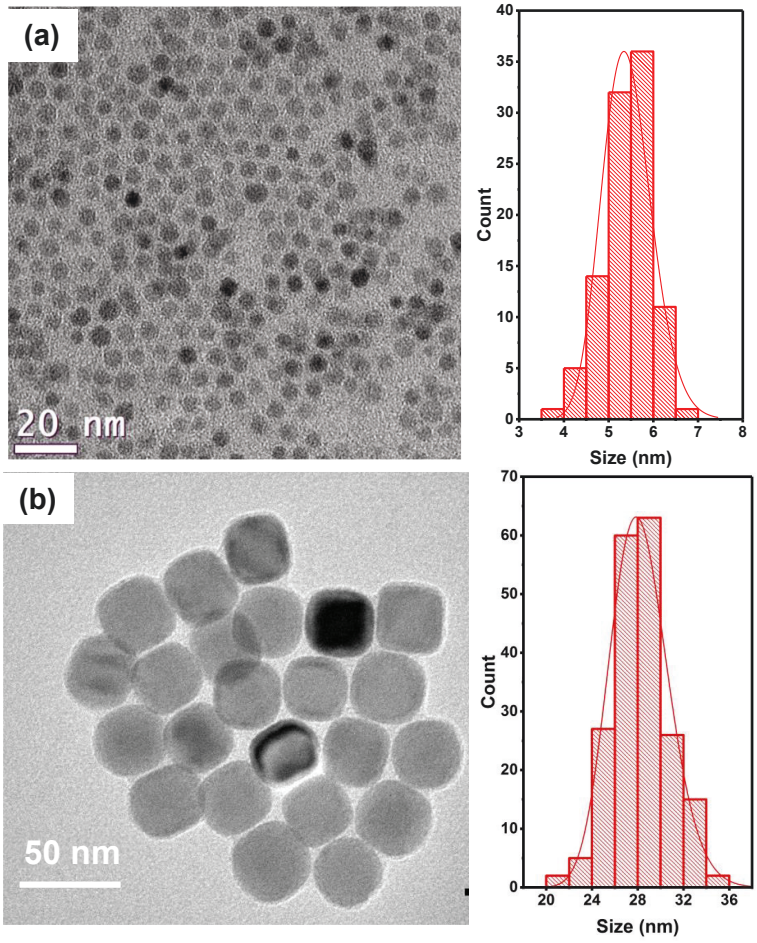

Fig. 4. 1 TEM images and corresponding size distribution histograms of sample (a) ON5 and (b) NP28. The solid line is the fit to lognormal distribution function.

4.1.2.2 SAXS data

The volume averaged SAXS measurements were used for a more precise determination of the size and size distribution of the nanoparticles. For these measurements, samples were diluted in toluene (ON5) and hexane (NP28). The detector images of GALAXI instrument converted into Q space are shown in Fig 4.2 (a) and (b) for both samples. The circle and rectangle low intensity area are the shadow

from the beam-stop, which was used to protect the detector from over saturation. These regions were excluded from the data analysis.

In order to quantitatively analyze the detector images, the intensity was radially averaged from the background-subtracted 2D data (Fig. 4.2 (c) and (d)). Both 1D data sets were refined against the spherical form factor. In case of cubic nanoparticles, our TEM data (Fig.4.1 b) showed that such simplification is justified, as particles can be described as spheres in the first approximation. The fitting of 1D patterns were done with SasView software packages [9]. The quality of the fits is shown in Fig. 4.2 (c, d).

The size and size distribution obtained from refinements are 5.6 (PD: 0.13) nm and 30.6 nm (PD: 0.07), for ON5 and NP28 samples, respectively. The dimensions obtained with refinements of SAXS data are in good agreement with our TEM results.

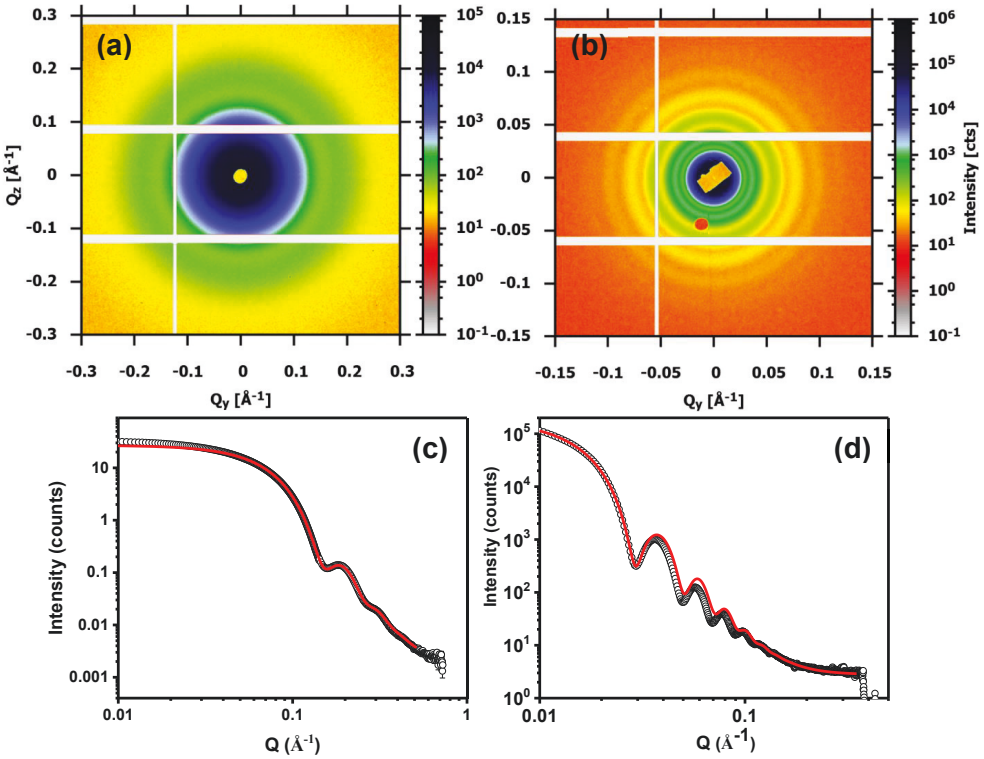

Fig. 4. 2 SAXS pattern of (a) ON5 and (b) NP28. The zero intensity lines are coming from the gaps between detector modules. The 1D SAXS spectra of (c) ON5 and (d) NP28 were radially averaged. Refinements of spherical form factors are presented by red solid lines.

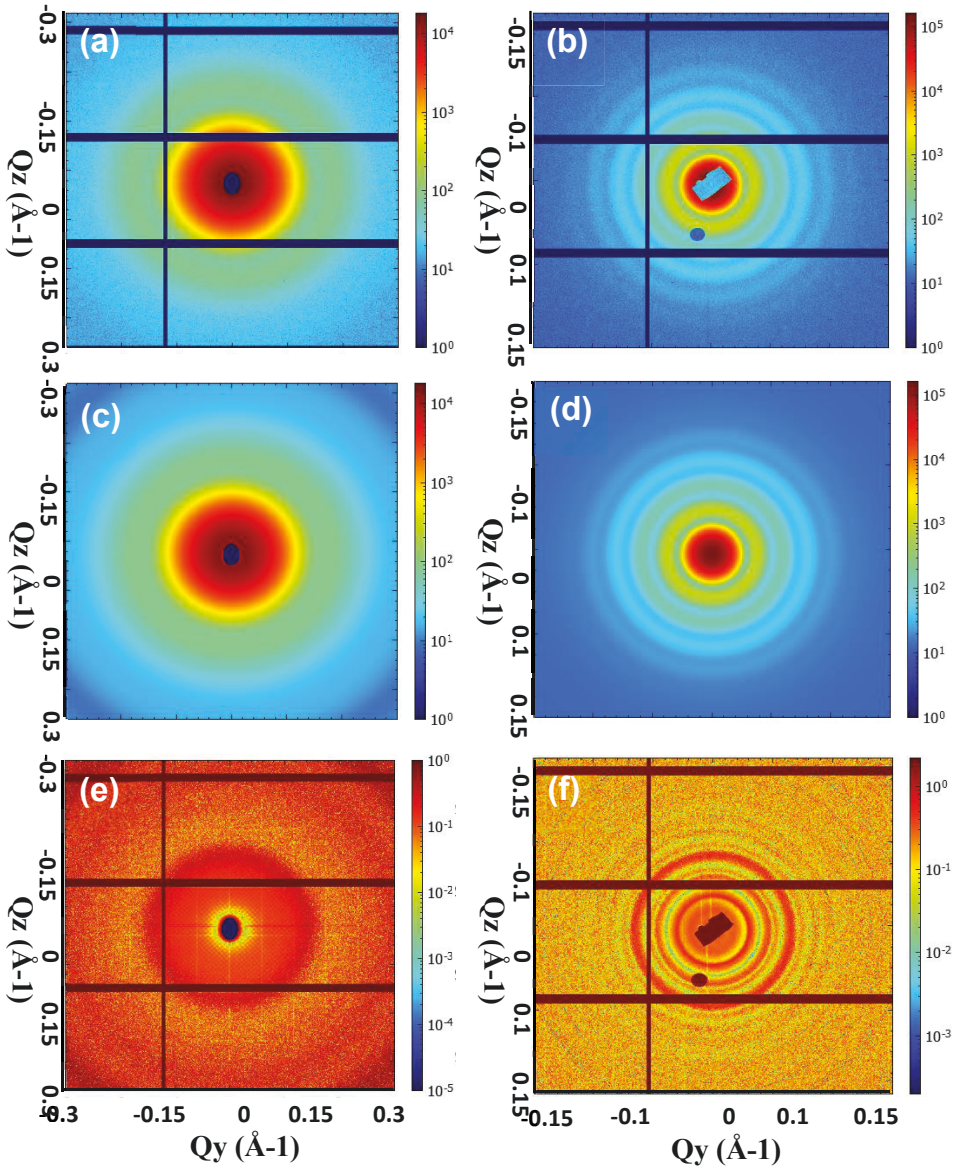

Fig. 4. 3 Raw 2D SAXS patterns of (a) ON5 and (b) NP28. The BornAgain refinements of SAXS of (c) ON5 and (d) NP28. Difference between raw data and refinement of ON5 and NP28 refinements are presented by red solid lines in (e) and (f).

We further modeled the SAXS patterns using the framework of the Born approximation (BA) by using BornAgain software package that allows to modeling an entire 2D detector image of GALAXI (Fig.4.3). We used the PD values obtained from 1D refinements with SasView as entry parameters for BornAgain model. By refining the 2D SAXS pattern with a spherical form factor, we obtained an averaged diameter of 5.6 nm and 30.2 nm for ON5 and NP28 samples, respectively. Both values are in excellent agreement with refinements of 1D profiles. The difference between measurements and refinements were shown in Fig. 4.3 (e) and (f). For ON5 and NP28, the difference is evenly distributed. There is no asymmetric difference which could come from the nanoparticles shape anisotropy. We use the SasView refined averaged size and polydispersity. The simulations of entire 2D scattering pattern from stand-alone nanoparticles reveal no anisotropy effects caused by inter-particle interactions or shape anisotropy. The form factors obtained from 2D refinements of both samples in BornAgain were used during more complicated simulations and refinements of GISAXS data of self-assembled nanostructures in composite films and sapphire substrates.

4.1.2.3 Magnetization data

The temperature- and field-dependent magnetization measurements were performed after drying ON5 and NP28 nanoparticle suspension on a Si substrate, in the temperature range from 5 K to 300 K and a magnetic field up to 5 T. Fig. 4.4 (a) shows the ZFC/FC magnetization curves of ON5 iron oxide nanoparticles measured at 200 Oe. The blocking temperature is around 14 K. The ZFC and FC curves merge and decrease at the same rate right above the blocking temperature. Fig. 4.4(b) shows the hysteresis loops recorded at 5 K and 300 K for ON5 sample. At 300 K the ON5 nanoparticles shows zero remanence and zero coercivity, indicating that the ON5 nanoparticles are in a superparamagnetic state. Below the blocking temperature, at 5 K we find a coercive field of ~60 Oe and higher saturation magnetization, characteristic of ferrimagnetic or ferromagnetic state.

Fig. 4.4 (c) shows the ZFC and FC magnetizations as a function of temperature from 5 to 300 K for the NP28 nanoparticles deposited on a Si substrate. As can be seen in the ZFC curve, the magnetization increases rapidly above 200 K, which matches the Néel temperature of wüstite (FeO), and hits FC curve at about 300 K. Below 200 K, the Verwey transition (magnetite crystal lattice changes from a monoclinic structure to the cubic inverse spinel structure) at T_V = 125 K has been observed which indicates that majority of the phase in this sample is magnetite. The FC magnetization is nearly constant with increasing temperature from 5 K to 200 K followed by a rather sharp increase up to 250 K. Above this temperature, the magnetization decreases smoothly. The hysteresis loops recorded at 5 K and 300 K of NP28 nanoparticles are shown in Fig. 4.4 (d). Even at room temperature, the NP28 sample shows small coercivity (~120 Oe),

indicating that the blocking temperature is above 300 K. The composition of NP28 sample is more complex compared to ON5 and likely includes several iron oxide phases, evident from our magnetization measurements and from previous reports on the same [5]. However, understanding the exact composition of NP28 sample is beyond the scope of this work.

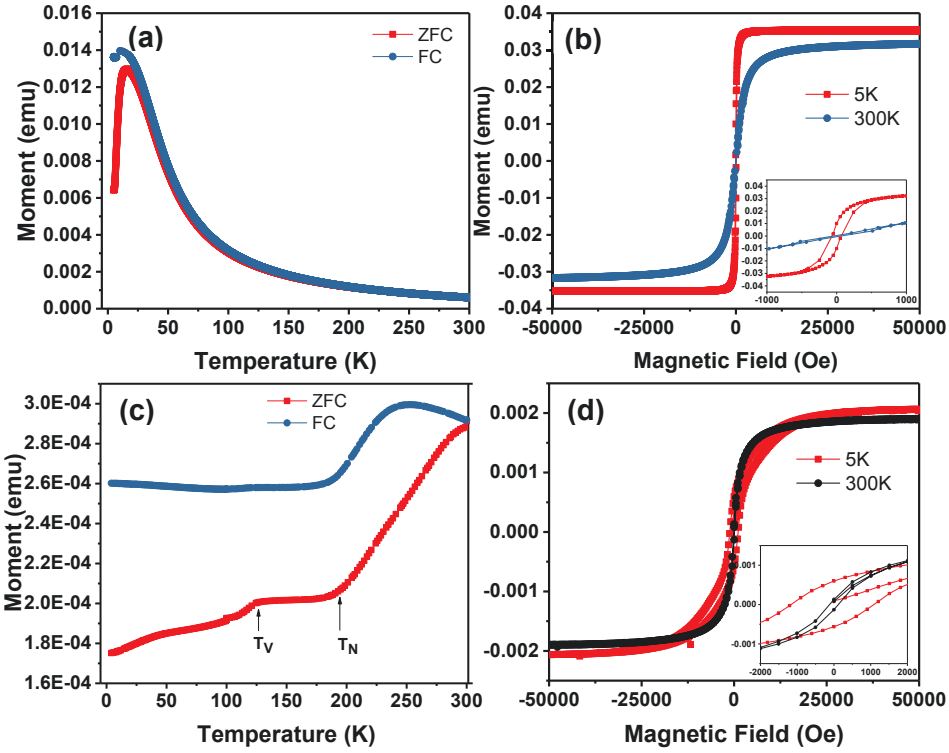

Fig. 4. 4 (a) M-T at 200 Oe and (b) M-H at 5 and 300 K of ON5. (c) M-T at 200 Oe and (d) M-H at 5 and 300 K of NP28 at 200 Oe. Inset in (b) and (d) shows an enlarged view around zero field.

4.2 Sapphire substrates

In this work, we used the patterned sapphire as template to guide nanoparticles self-assembly into 2D and 3D nanostructures. Thermal annealing was employed to produce patterned sapphire. Sapphire with a hexagonal structure (Fig. 4.5) has a high melting point of 2040 °C. The M-plane (10-10) has a very high surface energy density, which means it is an unstable surface [10, 11]. When M-plane of sapphire is annealed at

elevated temperatures (below the melting point), the M-plane needs to minimize its surface free energy by rearranging into facets of more stable (-1 1 0 1) and (1 -1 0 2) planes [10, 12, 13]. The angles of (-1101) and (1-102) planes to (10-10) plane are 32.4 ° and 17.6 °, respectively. The saw-toothed topography over the entire surface is formed after the surface reconstruction, where the orientation of the facets is associated with the underlying single crystal. The dynamics of the pattern formation were described in five major stages: surface smoothing, individual facet formation, formation of facet domains, facet coalescence and facet coarsening [14]. The width and amplitude of the saw-toothed pattern can be controlled by varying the annealing temperature and time. Our main purpose was not to investigate the detailed dynamics of the pattern formation, but rather find appropriate parameters to produce some suitable substrates for self-assembly of ON5 and NP28 nanoparticles.

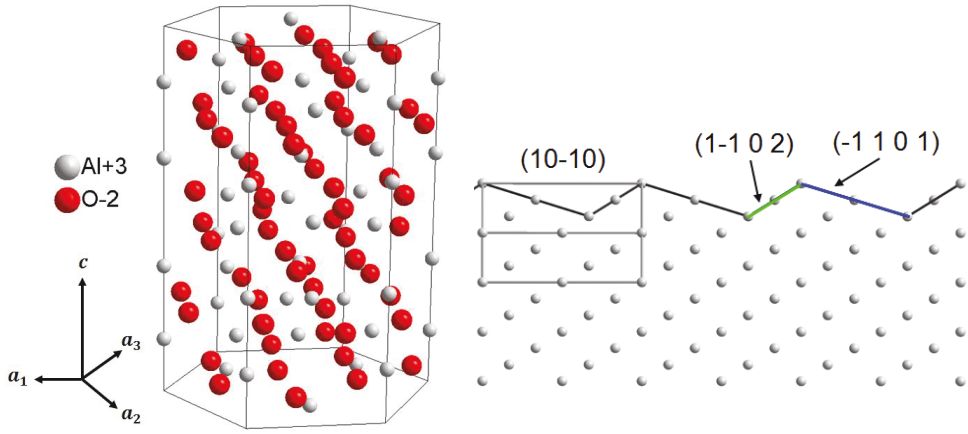

Fig. 4. 5 The crystal structure of sapphire and the schematic representation of the relevant planes.

4.2.1 Patterned substrate preparation

M-Plane sapphire wafers were purchased from SurfaceNet (Rheine, Germany). They were cut into 6 mm x 8 mm or 12 mm x 15 mm pieces. And different substrates were obtained by annealing in air at different temperatures (1350 °C, 1400 °C, 1450 °C or 1500 °C) for 24 hours.

4.2.2 Characterization

Atomic force microscopy (AFM) measurements were carried out at room temperature with a Bruker MultiMode8 AFM, under the tapping mode. The model of the probes used

in measurements is RTESPA-300. The spring constant of the cantilever is 40 N/m with a resonant frequency ~300 kHz.

Grazing incidence small-angle X-ray scattering (GISAXS) measurements of the substrates were performed on GALAXI. The experimental setup was similar to our measurements of nanoparticle solutions. A detector with 981 x 1043 pixels was set up at a distance of 3530 mm from the sample position. The incident wavelength was 1.34 Å and the incident angle between the primary beam and the sample surface was set to 0.2 °. AgBH (silver behenate) is used as the reference sample to calibrate the sample-to-detector distance. The intensities (I) are plotted with respect to Q, where $Q = \frac{4\pi}{\lambda} sin\,\theta$, λ is the wavelength of the incident x-ray beam, and 2θ is the scattering angle.

4.2.3 Results and discussion

The surface and topographical properties of patterned substrates annealed at various temperatures are presented here. Fig. 4.6 (a), (b) and (c) show AFM images of the sapphire substrate after annealing at 1300 (sap1300), 1400 (sap1400), 1450 (sap1450) and 1500 °C (sap1500) for 24 hours. We observed the transformation of unstable M-plane into saw-toothed topography over the entire surface at elevated temperatures. The variations of pitches size and some facet junctions which cannot be avoided come out randomly across the surface of the quasi-periodic saw-toothed substrate. Those phenomena were previously documented during pattern formation mechanisms [11]. The pattern formation evolves by five distinct stages that start with the nucleation and growth of individual facets. The formation of neighboring facets limits the growth of each facet in width which causes the variations of the width. The facets can grow until they collide with another facet lengthwise, which becomes the facet junctions. The cross sectional line scans (Fig. 4.6(e)) perpendicular to the saw-tooth pattern show the amplitude and shape of the saw-tooth change with temperature. The amplitude increases with temperature. The sap1500 sample shows sharper saw-tooth patterns than other samples. The sap1500 has an averaged width of the saw-tooth of 140 nm and the averaged amplitude (29.6 nm) was calculated based on the angular relationship between different planes. The averaged amplitude is able to accommodate cubic nanoparticles (NP28) and thus, sap1500 sample was chosen to be a substrate for guiding self-assembly of cubic nanoparticles.

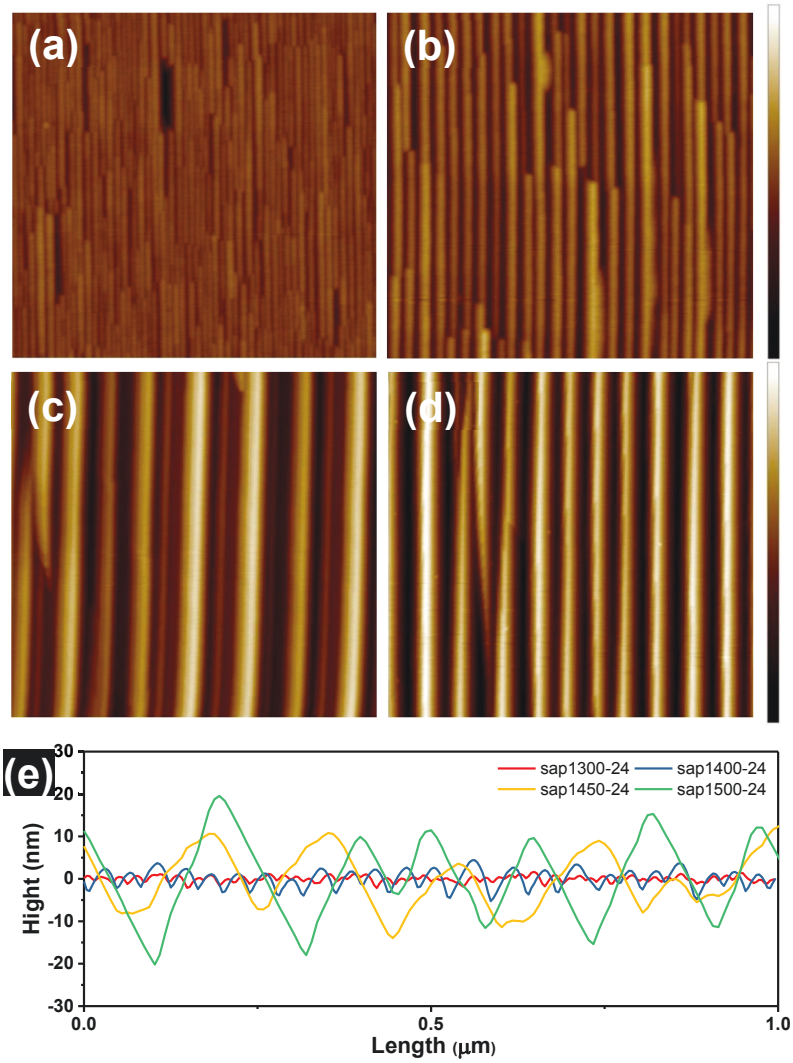

Fig. 4. 6 The AFM images of the faceted sapphire substrate annealed at (a) 1300 °C, (b) 1400 °C, (c) 1450 °C and (d) 1500 °C for 24 hours, respectively. The scan size was 1 x 1 μm for (a) and (b), and 2 x 2 μm for (c) and (d). The color bar indicates -10 to 10 nm for (a) and (b), -20 to 20 nm for (c) and (d). (e)The cross sectional line scan of the sapphire substrate annealed at different temperatures.

The GISAXS measurements were further employed for sap1500 sample, in order to obtain the averaged structural information over larger surface areas. The GISAXS measurements were performed at two different orientations of sap1500 substrate. In

one orientation, the incident beam was parallel to the saw-tooth patterns. The analysis of the scattering data in this orientation will provide the information about average width of the saw-tooth. Fig. 4.7 (a) shows the data where incident beam is parallel to the saw-tooth patterns. The averaged width of 146 nm was obtained by indexing Bragg peaks. The resulting amplitude was calculated to be 30.8 nm.

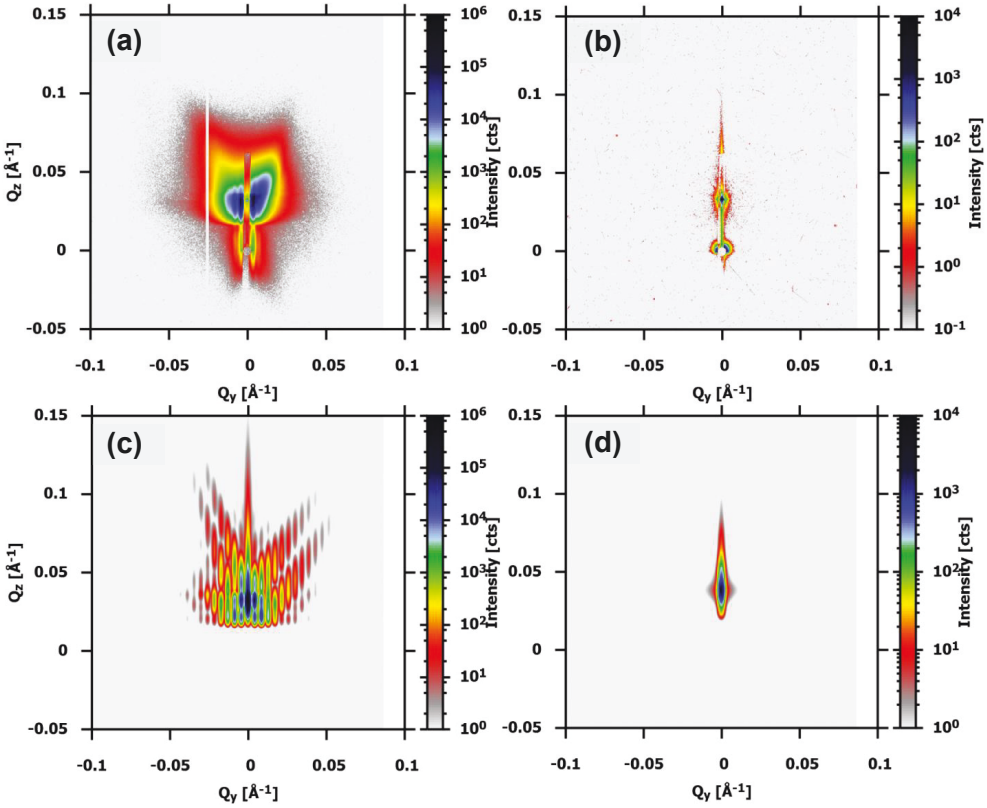

Fig. 4. 7 GISAXS collected with the incident beam (a) parallel and (b) perpendicular to the saw-tooth patterns at 0.2 °. The DWBA simulations of an ideal sample (c) parallel and (d) perpendicular to the saw-tooth patterns at the same incident angle.

The observed GISAXS patterns were modeled using software package of BornAgain based on DWBA (Fig. 4.7(c)). The modeled intensity showed narrower Bragg peaks than in the actual data. The experimental Bragg peaks in Fig. 4.7(a) were broader because of the saw-tooth pattern size distribution, facet conjunction and misalignment of saw-tooth, which would smear out the Bragg peaks. Those factors were not taken into account in the BornAgain simulation of the ideal sample.

Fig. 4.7 (b) shows the experimental GISAXS date with the stripes perpendicular to the incident beam. The majority of scattered intensity was confined in the off-specular line, as expected for this geometry. As the reciprocal lattice rotated with the sample geometry change and the scattering vector $Q_x \ll Q_y, Q_z$ based on the GISAXS geometry, there will be no Bragg peaks in the off-specular line when the magnitude of reciprocal lattice is larger than the scattering vector Q_x. The modeling of the data with BornAgain showed the same features (Fig. 4.7(d)). In the following chapter, all GISAXS data were collected in perpendicular geometry in order to avoid strong scattering from the patterned substrates that can hinder the scattering from self-assembled nanoparticles. We noted that all the necessary information of the self-assembly structural properties can be extracted from the measurements in perpendicular geometry.

4.4 Summary

The spherical ON5 nanoparticles (averaged size: 5.6 nm) are small enough to be embed in the nanocomposite films. They will be in a superparamagnetic state at room temperature. The sap1500 substrate (amplitude: 30.8, width: 146 nm) is a candidate for directing NP28 nanoparticles with 30.2 nm averaged size and narrow size distribution (0.07) self-assembly. In contrast to ON5 nanoparticles, NP28 nanoparticles will be in ferro/ferrimagnetic state at room temperature.

Chapter 5 Self-assembly of iron oxide nanoparticles guided by patterned substrates

5.1 Introduction

The self-assembly can be described as a process of arranging of individual 'bricks' into an ordered structure to build blocks. The self-assembly of nanoscale components is a promising method for nanofabrication. However, some methods, such as dip-coating [1], drop-casting [2] and spin coating [3], are unable to control the position and orientation of nanoparticles. Achieving such a high degree of control would require an additional directing factor. Directed assembly refers to the guided organization of particles with controlled alignment, location, and spacing. Numerous directed-assembly approaches have been developed to fabricate anisotropic ordered structures from dispersions of nanoparticles including application of electric fields [4], magnetic fields [5], and templates [6].

The template-directed self-assembly typically uses topographical patterns to guide the material assembly process. Hard templates can be considered as surface-modified substrates (in 1D, 2D, or 3D), containing special shape and periodic structure, which can selectively induce nanoparticle self-assembly. Based on the above concept, a series of methods has been developed to fabricate patterned substrates, including lithography [7], chemical etching [8], electrochemical reaction [9], thermal reconstruction [10] and so on. One great challenge is to fabricate nanoscale features over large areas in a simple way, at a low cost, and with a high throughput. Thermal reconstruction shows some advantages in fabricating hard templates [10-12]. M-plane (10-10) sapphire substrate surface is unstable, and spontaneously forms primarily (-1101) and (1-102) facets upon annealing at a high temperature [10-12]. After annealing at high temperature, the surface of M-plane sapphire will form saw-tooth patterns. The pitch and amplitude of saw-toothed pattern can be controlled by varying the annealing temperature. This chapter focuses on using patterned sapphire substrates, generated by a thermal reconstruction of M-plane sapphire wafers, to direct nanoparticles assemblies over a large surface area.

GISAXS and SEM had been used to investigate the self-assembled 2D structure. SEM is a direct way to visualize the self-assembly of nanostructures over a limited surface area. GISAXS is a powerful technique which provides the statistical average information over a large number of nanoparticles and larger surface area. Thus, GISAXS has a much higher statistical accuracy in description of self-assembled nanoparticles as compared to SEM. By combining those two methods, a better understanding of the 2D self-assembled nanostructures was achieved.

5.2 Sample Preparation

The magnetic nanoparticles (NP28) were separated on the sap1500 substrate to form 2D nanostructure by spin coating method. The different samples were fabricated by spin coating with spinning speed of 30 rps (revolutions per second) for 5 s with different volume of nanoparticles solution. After spin coating, the solvent was totally evaporated by drying at ambient conditions.

5.3 Results and Discussion

The SEM image of an empty sap1500 substrate is shown in Fig 5.1(a). Some facet conjunctions are randomly located on the surface, in agreement with AFM results shown in chapter 4. The sap1500 substrate is used as a hard template to direct NP28 nanoparticles assemblies. The sample (sap1500-1d30) is obtained by spin coating with spinning speed of 30 rps and one drop of solution (5 µl) on sap1500 substrate for 5 s (Fig. 5.1(b)). The images reveal that the most of the valleys are filled with NP28 nanoparticles. The nanoparticles form into 1D chains within the valleys. The chains are constituted of different number of nanoparticles and they have different lengths varying from the length of single particle to more than 1 µm. During the sample preparing process, the competition between the trap effect of the surface topography and the centrifugal force due to spinning determined the nanoparticle locations. And the capillary force between adjacent particles and the capillary force between particles and the valleys drove the nanoparticles to form one column closely packed configurations in the valleys during the evaporating. The characterized area in a typical SEM characterization is about 10 μm^2. In order to analyze the packing of nanoparticles on much larger template, GISAXS measurements had been employed. For GISAXS, the incident angle was fixed at 0.2 °, and the projection of the x-ray beam onto the surface is around 0.7 x 8 mm^2. The sample was aligned so that the direction of the x-ray beam is perpendicular to the ridge of patterned substrate. The GISAXS data collected in this configuration is shown in Fig. 5.1 (c) and (d). The scattering of the substrate can be extracted from the data along the off-specular line. The position and width of the Bragg peaks along Q_y direction contained the information about arrangement of nanoparticles

oriented parallel to the patterns. The detailed discussion of GISAXS measurements will be given in section 5.3.2.

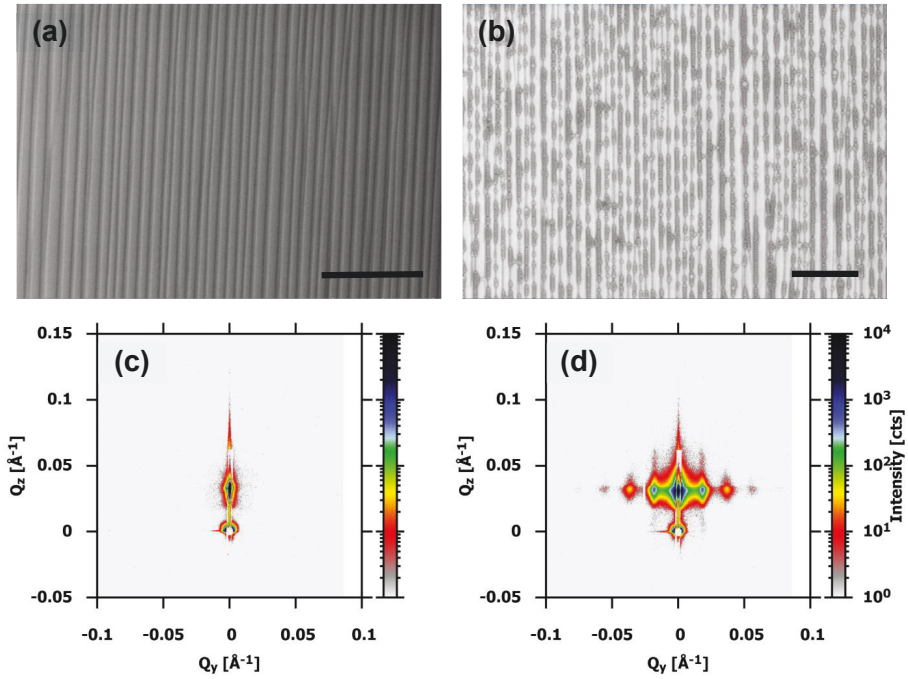

Fig. 5. 1 SEM images of (a) sap1500 and (b) sap1500-1d30 (scale bar: 1 μm). The GISAXS patterns of (c) sap1500 and (d) sap1500-1d30 with incident beam perpendicular to the ridge of patterned substrate.

In what follows, we will discuss the effects of various parameters on 2D self-assembly of NP28 nanoparticles.

5.3.1 The influence of patterned substrate

Different samples were fabricated by spin coating with spinning speed of 30 rps for 5 s on different substrates to study the influence of the substrate properties on the self-assembly. Since the amplitude of saw-tooth pattern on sap1300 substrate is too small to accommodate NP28 nanoparticles, only sap1400, sap1450 and sap1500 are used for the sample preparation. The SEM images in Fig. 5.2 (a), (b) and (c) show the influence of saw-tooth size on self-assembly. The nanoparticles only cover small parts of the sap1400, because the nanoparticle size is much larger than the amplitude of the saw-

tooth. There are some ribbons crossing the surface instead of arranged 1D chains along the valleys. Many areas are not covered with the nanoparticles at all. For the sap1450 substrate, nanoparticles are spread more evenly than on sap1400. When sap1500 is used, most of the nanoparticles are located within the valleys.

Based on SEM studies of various substrates we can conclude that due to the different size of saw-tooth, the trap effect of the surface topography is different. The centrifugal force overcame the trap effect of the surface topography and that leads to the escape of the nanoparticles from the valleys.

The GISAXS data are collected with the incident beam perpendicular to the ridge of patterned substrate. The line-cut at Qz = 0.032 $Å^{-1}$ (Yoneda line) for three different samples is presented in Fig. 5.2(d). The averaged center-to-center distances between nanoparticles obtained from GISAXS are 34.1, 34.1 and 34.5 nm, for sap1400, sap1450 and sap1500, respectively. And the line cuts show nearly same features, which indicate that the nanoparticles have similar arrangements, even on different substrates.

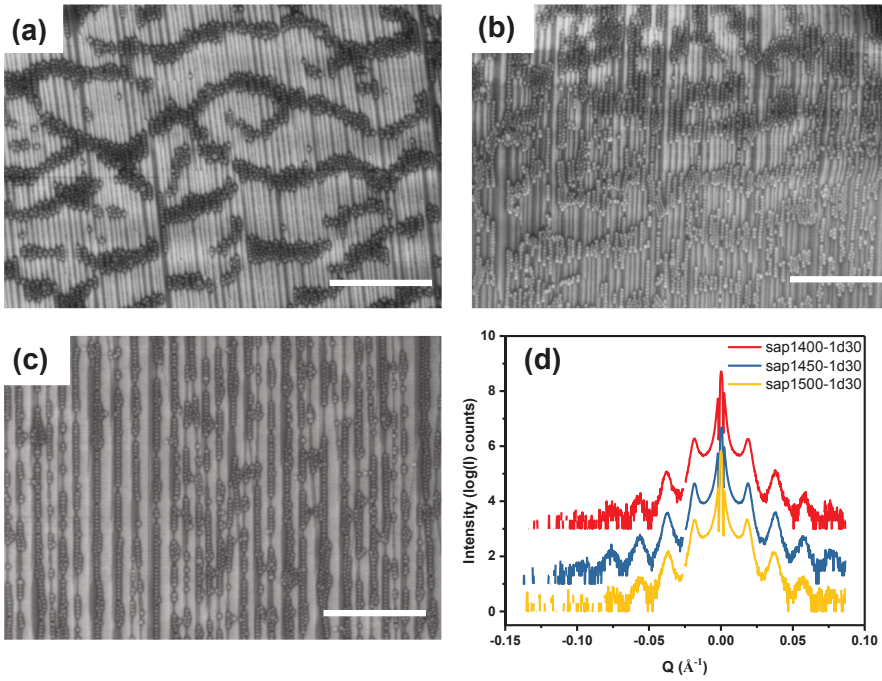

Fig. 5. 2 The SEM images of spin coating NP28 on (a) sap1400, (b) sap1450 and (c) sap1500 substrates. The scale bar is 1 μm. (d)The GISAXS line cut cross the specular peak.

5.3.2 The influence of suspensions volume

We studied effect of volume suspension on self-assembly of NP28 nanoparticles. Fig. 5.3 show samples obtained by spin coating with 5 µl (sap1500-1d30), 10 µl (sap1500-2d30), 15 µl (sap1500-3d30) and 20 µl (sap1500-4d30) of suspensions on sap1500 at the speed of 30 rps for 5 s, respectively. The suspension of nanoparticles was dropped on the surface by 5 µl (one drop) increments.

Adding 5 µl (sample sap1500-1d30) of suspension, results in formation of loosely packed quasi 1D chains within the valleys (see Fig. 5.3(a)). 10 µl (sample sap1500-2d30) of suspension form columns of chains along the valleys (Fig. 5.3 (b)). When the volume is increased to 15 and 20 µl, the nanoparticles are not only contained inside the valleys. Most of the surface of substrate is covered by the nanoparticles and the nanoparticles assemble into a hexagonal-like configuration (Fig. 5.3 (c, d)).

Common for all samples, we observe defects such as double-layers and vacancies sites (red circles in Fig. 5.3). These defects in the self-assembly of nanoparticles are a consequence of the quasi-periodic facet conjunctions and amplitude variations of sap1500 substrate.

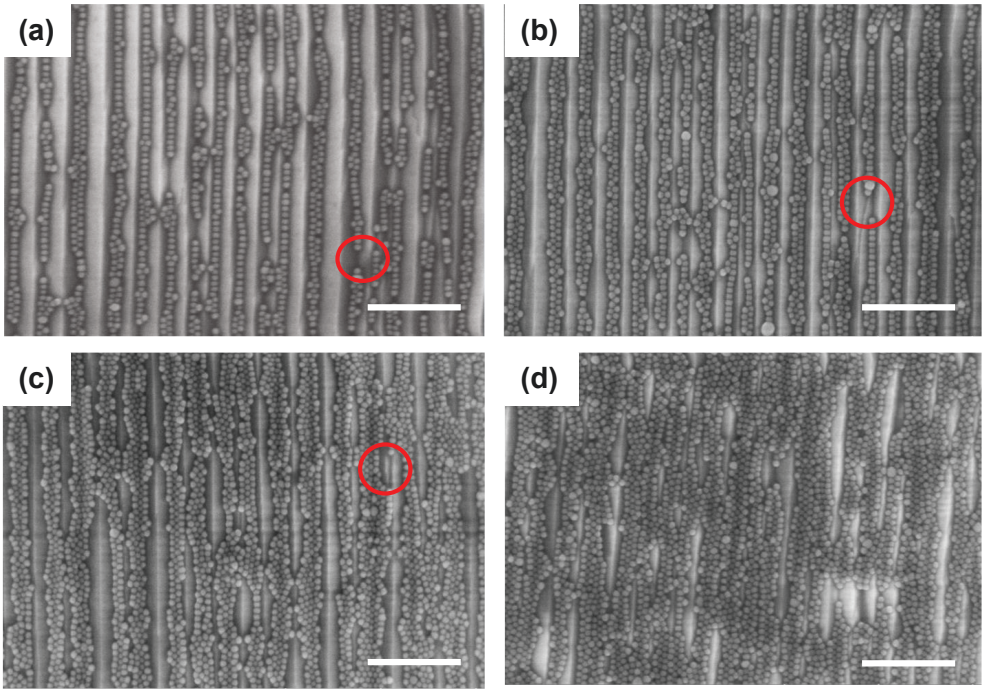

Fig. 5. 3 The SEM images of spin coating NP28 on sap1500 made with various suspension volumes: (a) 5 µl, (b) 10 µl, (c)15 µl and (d) 20 µl, respectively. The red circles indicate the facet conjunctions.

The GISAXS measurements have been performed with the incident beam perpendicular to the ridge of patterned substrate. The incident angle with respect to the substrate surface is 0.2 °. Fig. 5.4 shows the GISAXS patterns of four different samples. As the volume of suspension is increasing, the first order peak (Q_1, around 0.018 $Å^{-1}$) becomes broader and broader. The line-cut along Qy at Qz = 0.032 $Å^{-1}$ (Yoneda line) shown in Fig. 5.4 (e) gives more details on the change of the peak shape and its position. In agreement with 2D GISAXS data, 1D line-cuts confirm that sample with 5 µl volume suspension (sap1500-1d30) has the narrowest peak width.

In order to analyze the scattering data, the self-assembly structure has been simplified as 1D chain structure instead of 2D lattice, based on the relation between the position of four peaks ($Q_1 : Q_2 : Q_3 : Q_4 = 1 : 2 : 3 : 4$) shown in Fig. 5.4 (a). The position of all four peaks cannot be indexed with the hexagonal packed structure. The average inter-particle distance *d* is determined from the peak position in the reciprocal space, i.e. by $d = 2\pi/Q_y$. The averaged distance obtained from GISAXS is shown in Fig. 5.4 (f). The average center-to-center distance of four samples is 34.5 nm, 33.9 nm, 33.5 nm and

33.4 nm, for sap1500-1d30, sap1500-2d30, sap1500-3d30 and sap1500-4d30, respectively. Counting the organic shell outside the nanoparticles which is estimated to add an additional 1~2 nm thickness on the nanoparticle cores and the averaged particle size (30.6 nm), the nanoparticles in the valleys became close to each other, when higher volume suspensions is used.

While the peak shape could give the ordering of the particles arrangement, the laterally correlated nanoparticles arrangement is obtained by fitting the first Bragg peak (Q_1) along Qy direction with Voigt function. The Voigt function is a probability distribution given by a convolution of Lorentz and Gaussian distribution functions. Gaussian distribution function is used to describe the primary beam. The correlation length is calculated by $\xi = 2\pi/FWHM$, where FWHM is full width at half maximum of Voigt function. During the peak fitting, w_G (the full width at half maximum Gaussian distribution function) was fixed at 0.00125 $Å^{-1}$ which is the instrumental resolution value of GALAXI. The correlation length estimated in this way shows a decrease with increase of the average inter-particle distance. The correlation length decreases from three times (~110 nm) of particles diameter to two times (~80 nm), from the lowest to the highest concentration. This observation suggests that the ordering of the nanoparticles arrangement in the valleys is sufficiently low, and it can be easily broken by oversaturating the substrate with more nanoparticles. The GISAXS data clearly demonstrate that the structure of the nanoparticles assemblies depends on the suspension volume. At higher concentrations, more nanoparticles aggregate in the same valleys at the expense of shortening the correlation length.

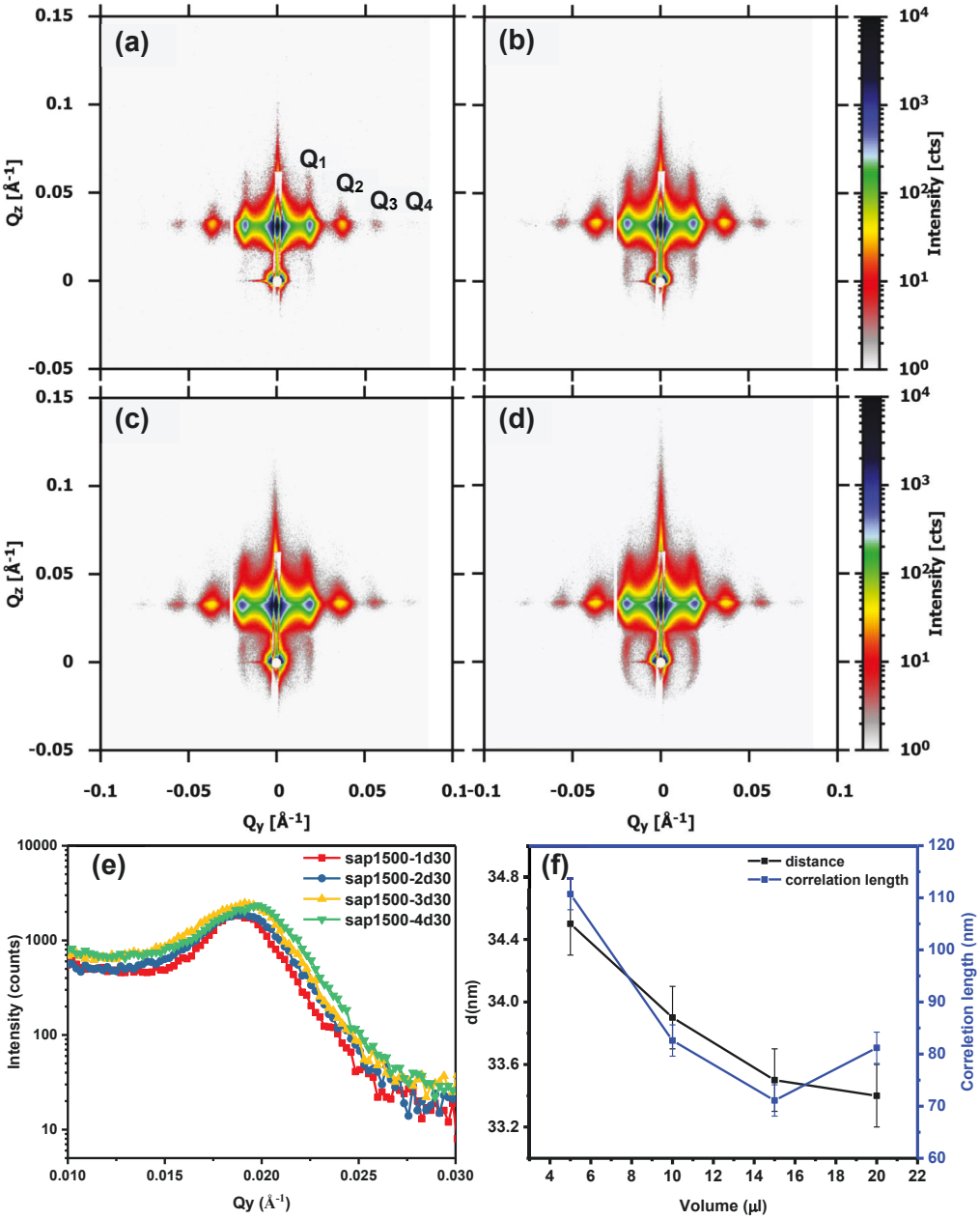

Fig. 5. 4 The GISAXS data of (a) sap1500-1d30), (b) sap1500-2d30, (c) sap1500-3d30 and (d)sap1500-4d30, respectively. (e) The line-cut at Qz = 0.032 Å^{-1}, and (f) the inter-

particle distance and correlation length of four different samples as a function of suspension volume.

5.3.3 2D data modeling with BornAgain

In order to quantitatively describe 2D assembly of our nanoparticles on extended surface area, the simulation and fitting of GISAXS data were performed within the frame of DWBA model. In our model, we assumed no long-range correlation between nanoparticles separated by the saw-tooth patterns. In other words, we assumed that the nanoparticles ordering in one valley is independent from the other ones, based on our SEM results. During the simulations and fittings, the 1D lattice interference function was chosen to limit the coherent scattering between particles in the 1D lattice. The spherical form factor was effective to describe the shape of NP28 nanoparticles that was proven by the refinements of 2D SAXS data (see section of 4.1.2.2). To simplify the simulations and fitting process, the perfect saw-tooth structures were defined by fixing the amplitude (30.8 nm) and width (146 nm) and no surface roughness was introduced.

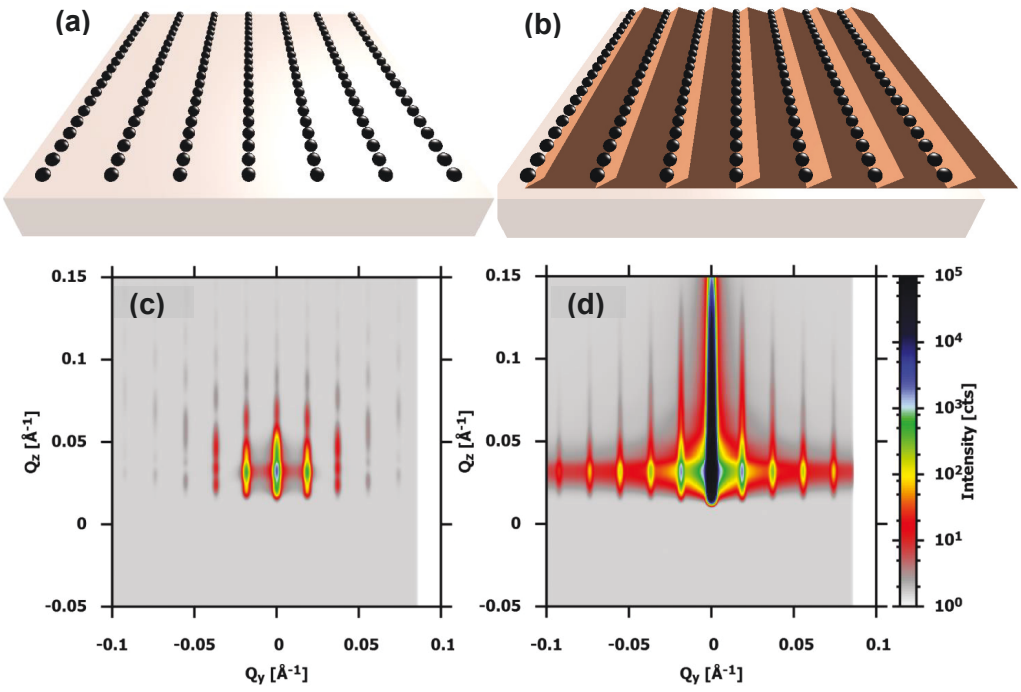

Fig. 5. 5 The ideal 2D lattice on (a) flat and (b) patterned substrate. The DWBA simulations of the ideal 2D lattice on (c) flat and (d) patterned substrate.

We start data analysis with the simulations of 2D ideal sample consisting of 1D chains, that do not interact with each other. Two different substrates, flat (Fig. 5.5 (a)) and patterned (Fig. 5.5 (b)), were used in the simulations in order to estimate the scattering pattern from the substrate. The simulations were done by setting the diameter of nanoparticles to 30.6 nm and PD = 0.07, according to our previous studies of stand-alone NP28 nanoparticles. A perfect 1D lattice along the x-axis with period of 34.5 nm was used and the incoming beam is perpendicular to the ridge of patterned substrate.

The simulation of array of nanoparticles on the ideal flat substrate sample (Fig. 5.5 (c)) displays a lot of satellite peaks, which correspond to the spherical form factor of nanoparticles. When the substrate changes to the patterned one, no satellite peaks show up but the shaper peak tails along Qz direction. And the repetition and intensity of peaks along Qy direction is enhanced. Even though, the patterned substrate contributed less scattering in Qy direction (Fig. 5.1 (c)), it still interferes with nanoparticles and affects the GISAXS pattern.

After the DWBA simulation of an ideal sample, the patterned substrate sample model is chosen to fit the GISAXS data of sap1500-1d30. The correlation length and the inter-particle distance are the main parameters during the fitting. The particle size, size distribution and form factor are set based on the BornAgain fitting of the SAXS measurement in chapter 4. The fitting script is attached in appendix B. The fitting GISAXS data and the difference (χ^2: 0.86) between measurement data and fitting data are presented in Fig. 5.6. Because the reflected beam and primary beam have been shielded by beam stop, this area (rectangle area in Fig. 5.6 (c)) had been excluded in fitting. The correlation length (106 ± 3 nm) and the inter-particle distance (34.1 ± 0.2 nm) obtained from the DWBA fitting match with the peak shape fitting by using Voigt function (~110 nm) and calculated inter-particle distance (34.5 nm) well. The substrate enhance effect is still very obvious along Qy direction because of highly uniform patterned substrate being used in fitting.

Table 5. 1 Parameters involved in the BornAgain simulation.

	Fe3O4	Sapphire substrate	
SLD_nuclear($Å^{-2}$)	6.9347e-06	5.7153e-06	fixed
Size (nm)	Diameter: 30.2 PD: 0.07	Length:146 Amplitude: 30.8	fixed
Center-to-center distance (nm)	34.1 ± 0.2		fitted
Correlation length (nm)	106 ± 3		fitted

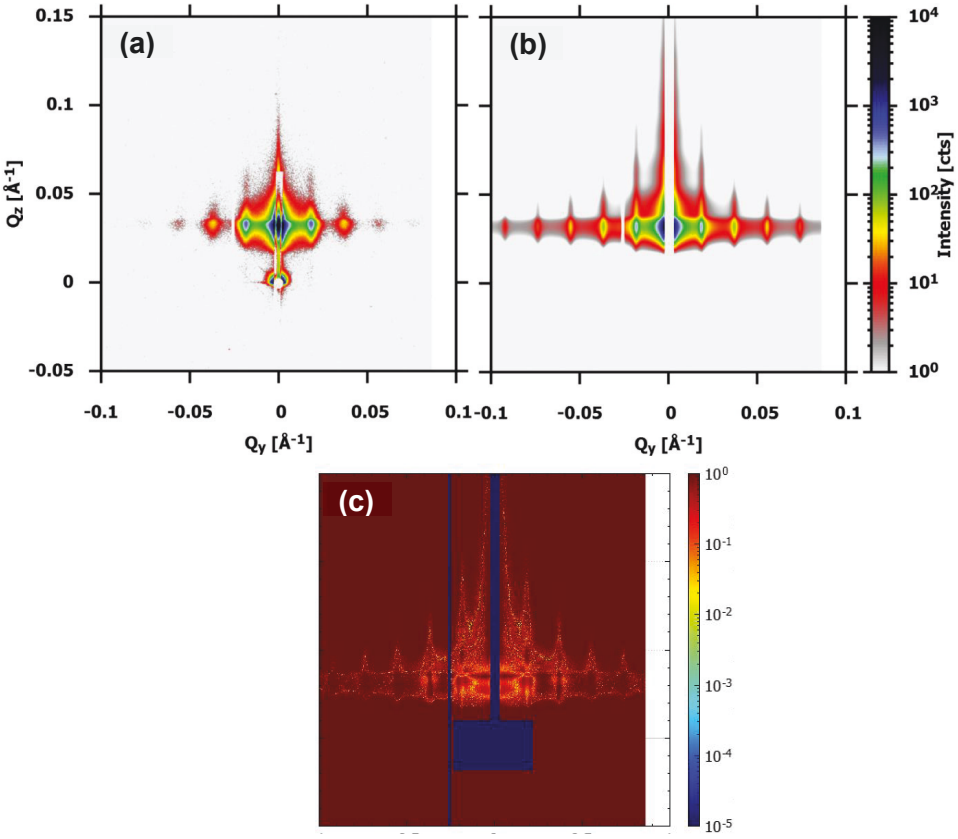

Fig. 5. 6 (a) The GISAXS data of sap1500-1d30. (b) The DWBA fitting of GISAXS data and (c) the difference between the measurement and fitting.

5.4 Summary

In summary, the thermally reconstructed M-plane sapphire substrate is used to guide the self-assembly of NP28 nanoparticles. The quasi-periodic saw-tooth structure could produce trap effect to balance the centrifugal force during the spin coating. Moreover, it can align and distribute nanoparticles into a 2D nanostructure with the facet geometry. Based on our experimental results, we conclude that the sap1500 sample (amplitude: 30.8 nm, length: 146 nm) is a good candidate to direct the self-assembly of NP28 nanoparticles with diameter of 30.6 nm. The study of the effect of suspension volume on the self-assembly reveals that adding more nanoparticles on the substrate shortens the correlation length. We found no evidence of the hexagonal ordering in the samples with a high suspension volume. The DWBA simulations reveal that the saw-tooth topography

does affect the GISAXS pattern even when the incident beam is perpendicular to the ridge of patterned substrate. The DWBA fitting results demonstrate the 2D lattice with 1D lattice interference function is a reasonably model to describe sample during scattering.

Finally, by carefully choosing the annealing temperature of the substrate, size of nanoparticles and suspension volume we are able to manufacture highly correlated 2D nanoparticle assemblies on a large surface area. The significance of this finding has not found potential applications.

Chapter 6 Guide Magnetic Nanoparticle Assemblies in Thin Films via Patterned substrates

6.1 Introduction

The block copolymers are able to form versatile nanoscale morphologies via microphase separation processes that make them as templates to guide nanoparticles self-assembly [1, 2]. Due to the large ratio of surface-to-volume ratio, nanoparticles can have tremendous advantages in their physical and chemical properties [3]. Hybrid nanocomposites based on a block copolymer matrix and embedded magnetic nanoparticles have attracted great interest, because they are ideal candidate materials for applications requiring superparamagnetism [4], magnetic sensors [5] or electromagnetic wave absorption [6].

After polystyrene-block-poly (4-vinylpyridine) (PS-b-P4VP) is blended with 3-pentadecylphenol (PDP) in the solvents, the comb-shaped supramolecular (Fig. 6.1 (a)) are obtained consisting of a polystyrene (PS) block and a supramolecular block of poly(4-vinylpyridine) (P4VP) hydrogen bonded with PDP. The block copolymers matrix, PS-b-P4VP(PDP)x, can have different morphologies (Fig. 6.1), such as lamellae, vertical cylinders, and horizontal cylinders [7-11]. The structural frameworks formed by PS-b-P4VP mixed with PDP can be tuned by adjusting the ratio of PS in the matrix. This can be achieved by choosing different molecular weight of PS-b-P4VP or adding a certain amount of PDP. The NPs in the nanocomposites are connected to P4VP(PDP)x with a hydrogen bond. The self-assembly of PS-b-P4VP mixed with PDP has been used to confine spherical nanoparticles, nanorods or nanodiscs in one-dimensional, two-dimensional or three-dimensional arrays [12-16].

Thermal annealing and solvent vapor annealing are very common methods to enable the self-assembly of the block copolymer based nanocomposites [17, 18]. Thermal annealing has to be performed above the glass transition temperature of both blocks and below the order-disorder transition temperature of the block copolymer. For several block copolymers, the small temperature windows and thermal stability limit the possibilities of thermal annealing, as for example the thermal stability of silicon containing blocks is expected to be relatively low [19]. In contrast, solvent vapor

annealing can be performed at room temperature. The solvent vapor can reduce the glass transition temperature and increase the polymer chain mobility when the block copolymer based nanocomposite is exposed to a solvent.

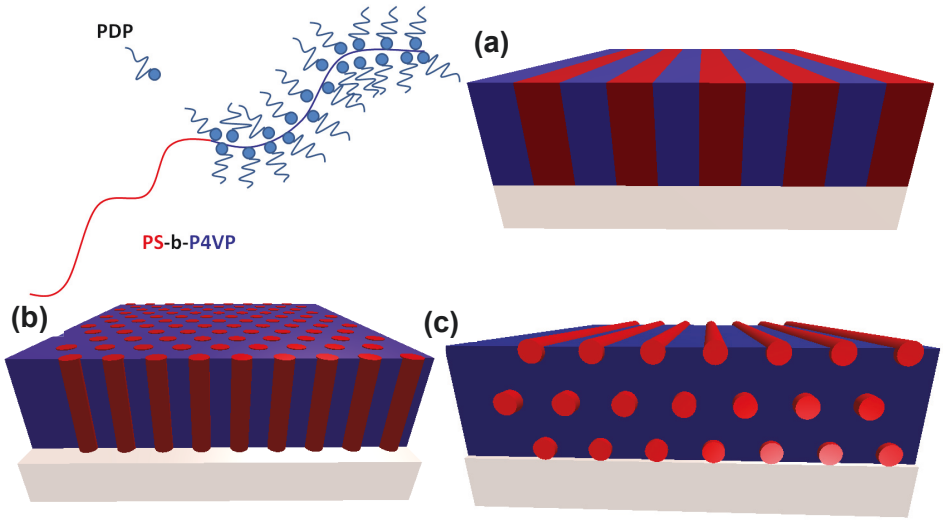

Fig. 6. 1 The schematic drawing of the nanostructure of PS-b-P4VP(PDP)x thin films after solvent annealing, (a) lamellae (b) vertical cylinders and (c) horizontal cylinders. The PS domains are red and the P4VP(PDP)x domains are blue.

In order to control the macroscopic structure of block copolymer based nanocomposites, faceted substrates have been developed to control the macroscopic alignment of microdomains in thin films [12, 20-21]. Thermal reconstruction offers a highly attractive choice and an inexpensive means of generating nm-scale substrate patterns for guided nanocomposites self-assembly. Park *et al.* introduced the use of a thermal reconstructed saw-tooth sapphire substrate to guide the self-assembly of PS-b-PEO films. Cylindrical microdomains of PEO were oriented normal to the film surface with long-range quasi-crystalline order [22]. The saw-tooth sapphire substrate has also been used to direct 3D Au nanoparticles assemblies in PS-b-P4VP(PDP)1.7 thin films [12]. The results show that by using saw-toothed substrates, thin films of nanocomposites containing 3D NP arrays with a long range order can be readily obtained. 3D NP arrays, aligned perpendicular to the ridge of the saw-tooth substrate, were fabricated in films with thicknesses less than 200 nm on saw-tooth substrate.

In this chapter, we show that thin films of nanocomposites containing 3D magnetic NPs arrays with a well-defined orientation can be obtained by using saw-toothed sapphire substrates. Our aim was to prepare highly ordered nanostructures by optimizing the

sample preparation process. The structure of nanocomposite film was characterized by a combination of atomic force microscopy (AFM) and grazing-incident small angle X-ray scattering (GISAXS).

6.2 Methods

6.2.1 Sample preparation

Polystyrene- block-poly(4-vinylpyridine) (PS-b-P4VP) (number average molecular weight, Mn_{PS} = 19 kg * mol^{-1}, Mn_{P4VP} = 5.2 kg * mol^{-1}, Mw/Mn = 1.10, where Mw is the average molecular weight) was purchased from Polymer Source (Montreal, Canada). 3-n-Pentadecylphenol (90%) (PDP) and chloroform ($CHCl_3$) were purchased from Sigma-Adrich. Iron oxide nanoparticles (ON5) with the average diameter of 5.6 nm were purchased from Ocean Nanotech. The nanoparticles were dispersed in chloroform at the concentration of 25 mg/ml. All chemicals and materials were used as received with no further purification. Supramolecular solution was prepared by dissolving the appropriate amounts of PS-b-P4VP block copolymer and PDP in chloroform (PS-b-P4VP(PDP)1.7). The concentration of polymer was maintained at 1 wt % to ensure homogeneous complex formation, and the solution is stirred overnight at room temperature. The nanoparticle suspension was mixed with a supramolecular solution by vigorous shaking. The ratio of the NP solution and supramolecular solution was carefully controlled as 8 % weight percentage. Thin films were prepared by spin-coating the mixed solutions onto sap1500 substrates with spinning speeds ranging from 30 to 70 rps. For solvent vapor annealing, samples were annealed using 120 µl of $CHCl_3$ injected inside a 100 ml top-capped jar at room temperature for 2 ~ 10 minutes. When solvent vapor annealing was completed, the jar was opened and the chloroform solvent vapor in the jar was allowed to freely evaporate.

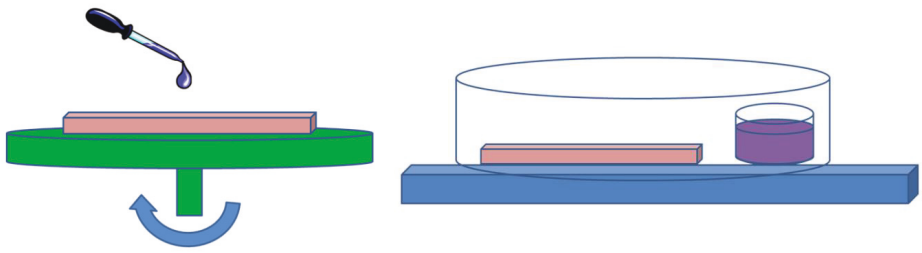

Fig. 6. 2 The schematic representation of the spin coating and solvent vapor annealing.

6.2.2 Characterization

AFM measurements: AFM imaging was performed on a Bruker MultiMode8 AFM under the tapping mode. The model of the probes used in measurements is RTESPA-300. The spring constant of the cantilever is 40 N/m with a resonant frequency ~300 kHz.

SEM measurements: SEM was employed in order to obtain the film thickness. The sample was soaked in liquid nitrogen for 10 s and broke into half to get cross-section SEM image.

GISAXS measurements were performed on Gallium Anode Low-Angle X-ray Instrument (GALAXI) in Jülich Centre for Neutron Science. A Pilatus 1M 2D position sensitive detector with 981*1043 pixels was set up at a distance of 3530 mm from the sample. The incident wavelength was 1.34 Å and the critical angle between the primary beam and the sample surface was set to be 0.18 ◦ and the exposure time for each measurement was 1800 s for consistent data acquisition. The intensities (I) were plotted as a function of Q, where $Q = \frac{4\pi}{\lambda} sin\,\theta$, λ is the wavelength of the incident X-ray beam, and 2θ is the scattering angle. The azimuthal angle (ψ) dependent GISAXS were performed from -30 ◦ and 30 ◦.

Magnetization measurements were performed using a Quantum Design Physical Property Measuring System (Dynacool) equipped with a superconducting magnet and a vibrating sample magnetometer (VSM) option. **Temperature dependent** magnetization measurements (zero-field-cooling (ZFC) and field-cooling (FC)) were carried out between 5 and 300 K with a heating rate of 1 K/min in an applied magnetic field of 200 Oe, during cooling in either applied field or in zero field. **Field dependent** magnetization measurements were performed at 5 and 300 K with 1 T.

6.3 Results and Discussion

6.3.1 Film thickness

During the film preparation procedures, three parameters were important to control the film thickness: spinning speed, volume and concentration of a supramolecular solution. In order to ensure homogeneous mixture, the concentration of polymer was maintained at 1 wt %. The effect of the volume and spinning speed had been considered. When the volume changed from 5 to 12 µl, the spinning speed was fixed as 30 rps. While varying spinning speed, the 5 µl of solution was chosen. The thickness of the nanocomposite film was measured with a cross-section SEM. The cross-section SEM images of nanocomposite films produced by 5 µl 30rps (260 (3) nm, Fig. 6.3 (a)) and 5 µl 50 rps (127 (3) nm, Fig. 6.3 (a)) show a uniform thickness. Arrows indicate the film thickness,

which is the distance between the silicon substrate and the film top surface. As the volume increases, the thickness of the film decreases from 260(3) nm to 147(3) nm monotonically, as shown in Fig. 6.3 (c). A non-linearly decrease was found in the speed-dependent thickness (Fig. 6.3 (d)). A patterned sapphire substrate is more efficient when film thickness is less than 200 nm [12], 5 μl with 50 rps was chosen to fabricate thin films.

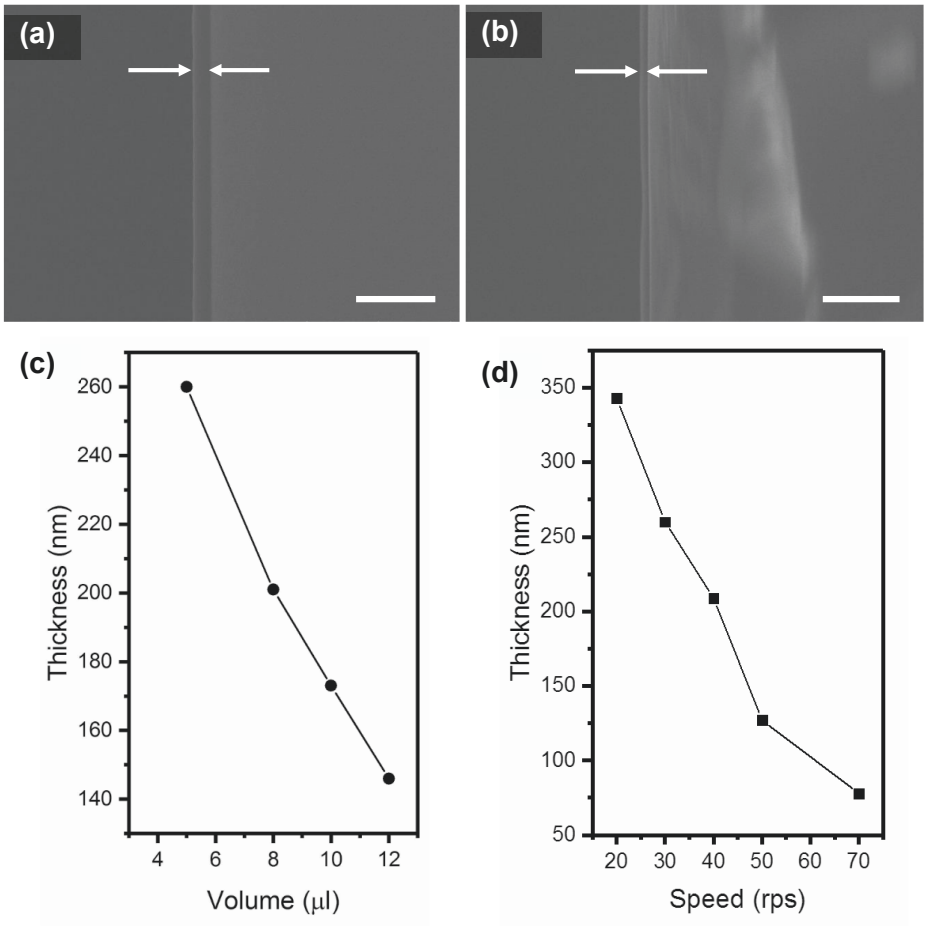

Fig. 6. 3 Cross-section SEM images of sample in spinning speed (a) 30 rps and (b) 50 rps with 5 μl. The film thickness is pointed out with arrows and the scale bar is 1 μm. Thicknesses of the films changed with (c) volume and (d) spinning speed.

6.3.2 Nanocomposite structure

Fig. 6.4 (a) and (b) show the AFM height and phase image of the nanocomposite films as prepared with spin coating. In the AFM phase images, the light regions correspond to the PS domain and the dark regions correspond to the P4VP(PDP)1.7 domain. The tiny light dots represent nanoparticles. The images indicate that the film was in a non-equilibrium state because of the fast solvent evaporating process, in which the structure was fixed in rather short time. The Fourier transform inserted in Fig. 6.4 (a) displays an isotropic sphere which corresponds to no preferred orientation in the film. Root mean square average surface roughness (Rq) is 0.614 nm. The GISAXS measurements indicate two weak and broad Bragg reflections at ± 0.0245 $Å^{-1}$. The position of the peaks provides the averaged distance between nanoparticles, which is found to be 25.6 nm. The correlation length of 70 nm is obtained from the Voigt function fitting of the peak shape along Qy direction. Such irregular morphology may not be desirable for applications. Therefore, a proper post-treatment, such as solvent vapor annealing process, is required to allow the film to rearrange.

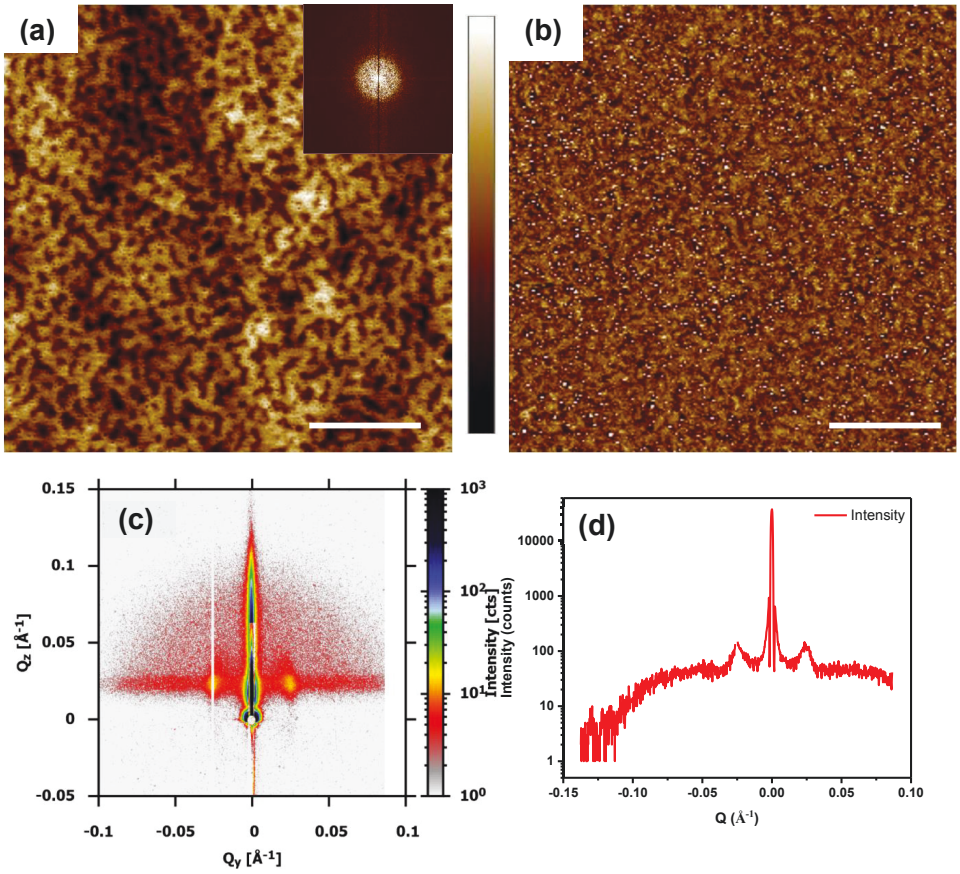

Fig. 6. 4 (a) The AFM height image. The insert is a 2D Fourier transform. (b) The AFM phase image of the as-prepared film. The scale bar is 500 nm. The color scale bar for height image is -2 to 2 nm and for phase image is -5 to 5. (c) GISAXS at 0.1 ◦ and (d) the line cut crossed Yoneda line (Qz= 0.024 Å^{-1}).

6.3.3 Orientation parameter

In order to quantitative analyze the film quality, the orientation parameter (S) was introduced [23]. For a 2D system, the orientation parameter is calculated using the following equation：

$$S = 2\{\sum I(\psi)cos^2(\psi) \mid \sum I(\psi)\} - 1 \quad (6.1)$$

Where $I(\psi)$ is the scattering intensity of the first-order peak at the azimuthal angle (ψ). The azimuthal angle dependent GISAXS were done between -30 ◦ and 30 ◦. The

original point (ψ = 0 °) is set as where the incident beam perpendicular to the ridges of the saw-tooth pattern. Incident angle 0.1 ° was chosen which is smaller than the critical angle of the film (~ 0.16 ° in literature) and the sapphire substrate (0.25 °). In this configuration, only surface structures are being probed. We used the orientation parameter of surface to qualify the order of the sample nanostructures. When the sample is rotated, increasing ψ, the first order Bragg peak intensity varies with the azimuthal angle (Fig. 6.5).

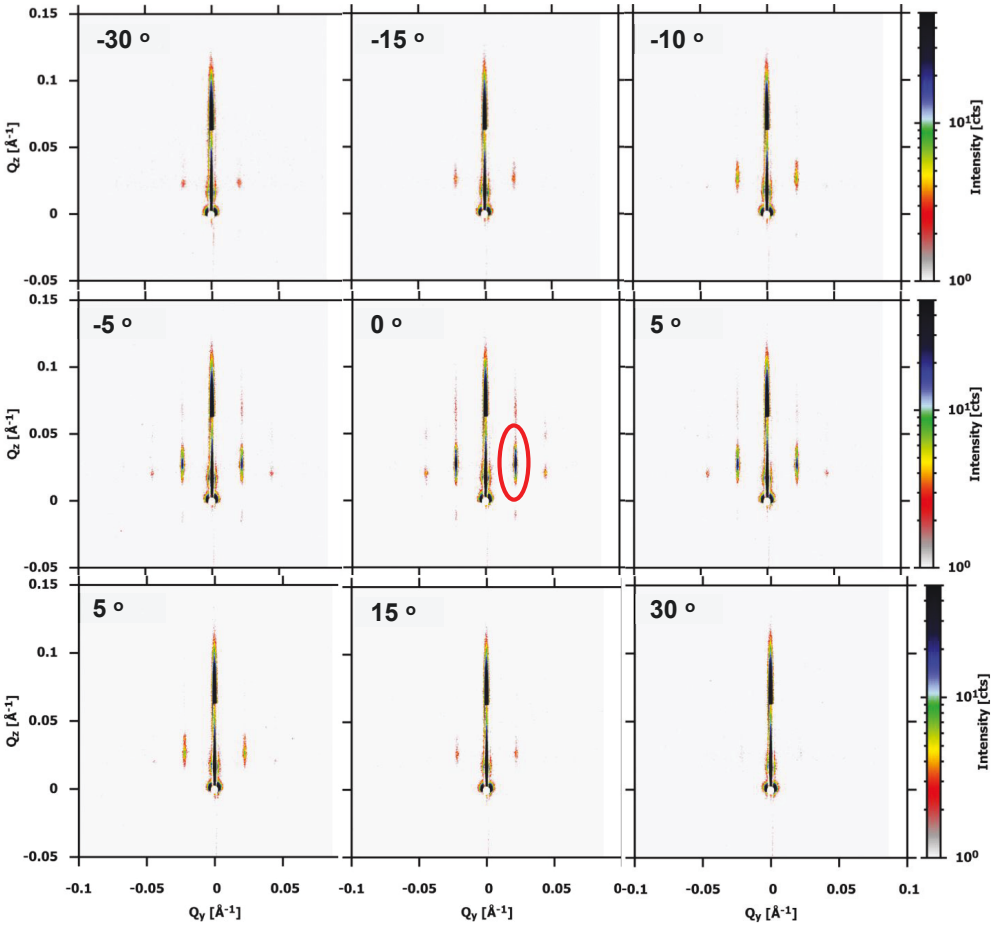

Fig. 6. 5 The azimuthal angle dependent GISAXS were done between -30 ° and 30 °. The red circle indicates the first order peak.

The first order Bragg peak intensity with the azimuthal angle is plotted as circles (in Fig. 6.6). We assume that the intensity ($I(\psi)$) follows a Lorentz distribution. The fitted curve

in solid red was used in the equation (6.1) to get orientation parameter (S). When S = 1, the horizontal cylinders are in the same orientation. The value of S is more closed to 1, which means the horizontal cylinders are in the highly alignments.

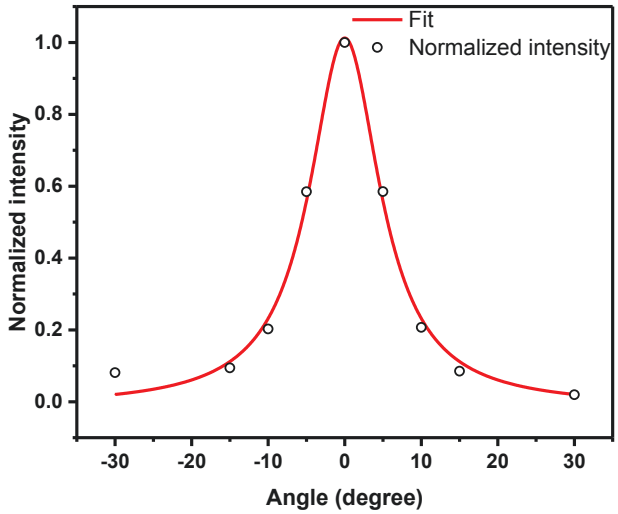

Fig. 6. 6 The normalized scattering intensity of the first order peak was determined from −30 ° to 30 °. Lorenz distribution fitting is shown as in solid red line.

6.3.4 The solvent vapor annealing process

The solvent vapor annealing used in this work describes a process of the film being exposed to the solvent vapor in a capped jar for several minutes followed by a free evaporation. Different samples followed the same annealing process but changing the time maintained in the jar. The solvent vapor annealing can be divided in three stages: solvent uptake, solvent concentration equilibration and drying. As the film uptakes the solvent, the solvent swells the film. The glass transition temperature of the block copolymer will decrease and the block polymer diffusivity will increase as the nanocomposites/solvent system reaches equilibration. When the capped jar is open, the solvent desorption will freeze the structure within the film. There are two important factors: annealing time and solvent volume. All preparation steps prior to the solvent vapor annealing were identical: 5 µl supramolecular solution was spin coated onto the sap1500 substrate at 50 rps.

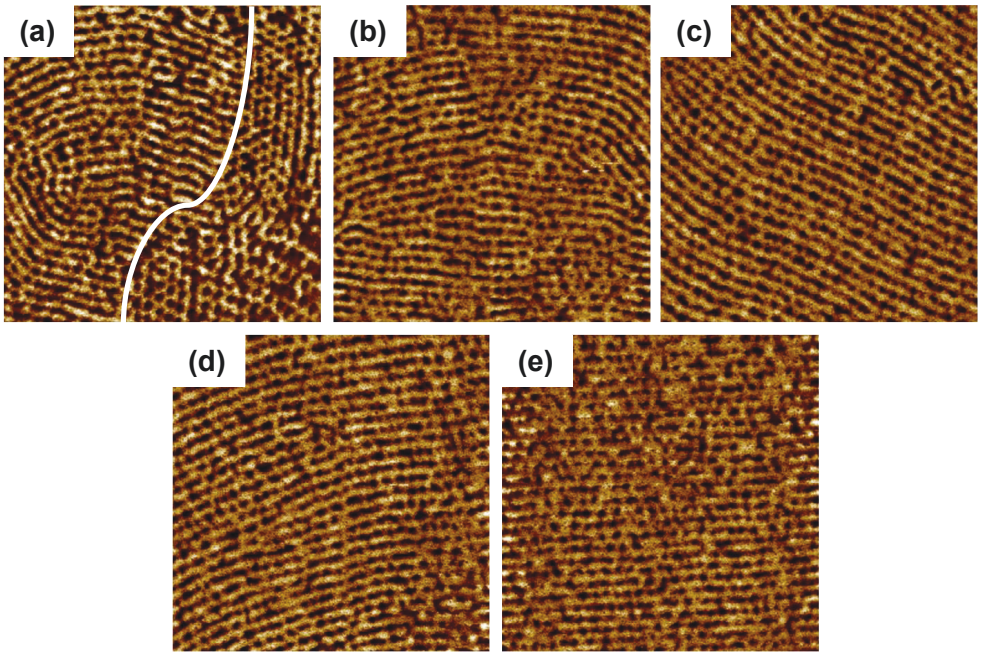

Fig. 6. 7 AFM phase images of the film annealed with 60 µl solvent for (a) 2, (b) 4, (c) 6, (d) 8 and (e) 10 minutes, respectively.

In Fig. 6.7, the AFM phase images show the morphology of film annealed with 60 µl for different times. It is easy to distinguish horizontal and perpendicular cylinders in Fig. 6.7 (a). As annealing time is increasing, there is no major difference from AFM images and surface morphologies in horizontal cylinders arrangements. Root mean square average surface roughness (Rq) is 2.15 nm, 0.667 nm, 0.506 nm, 0.722 nm, and 0.401 nm for annealing time of 2, 4, 6, 8 and 10 minutes, respectively. After 4 minutes, the roughness is quite stable until 10 minutes. The effect of increasing time was investigated by the azimuthal angle dependent GISAXS. The first peak intensity profiles (Fig. 6.8 (a)) indicates a clear azimuthal angle dependence of intensity distribution variations. The orientation parameter and the first peak intensity profiles are presented in Fig. 6.8. The S increased from 0.85 for 2 minutes to 0.96 for 6 minutes, and decreased slowly to 0.92 after 10 minutes annealing.

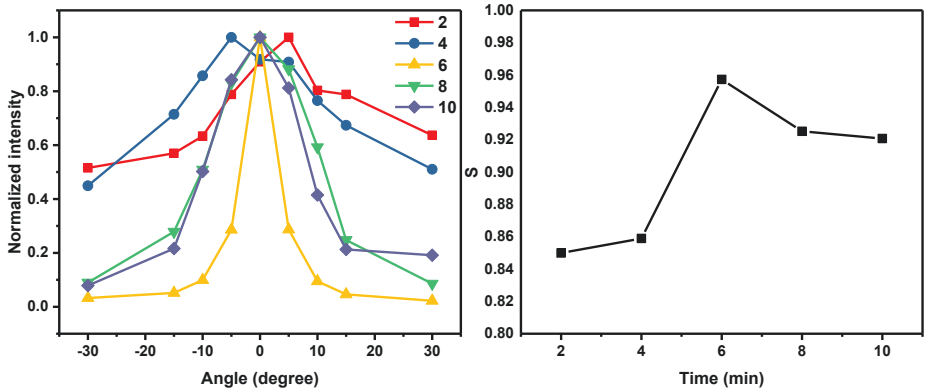

Fig. 6. 8 (a) The normalized intensity profiles and (b) orientation parameter (S) of films annealing with 60 µl solvent.

As the solvent volume is increased to 120 µl, only the image of the film annealed for 10 minutes show a difference from the other four films (Appendix D). Rq are 0.592 nm, 0.598 nm, 0.469 nm, 0.499 nm, and 0.481 nm for annealing time of 2, 4, 6, 8 and 10 minutes, respectively. The film surface is in the same state from 2 to 10 minutes. When 200 µl solvent has been injected in the jar, the AFM phase images cannot provide clear structural difference (Appendix chapter 6). Rq are 0.417 nm, 0.401 nm, 0.558 nm, 0.482 nm and 1.108 nm for annealing time of 2, 4, 6 and 8 minutes, respectively. When the time exceeds 8 minutes, the surface becomes rough. All different samples treated by different annealing parameters are listed in the Table 6.1.

Table 6. 1 The annealing parameters.

		Annealing solvent volume (µl)		
		60	120	200
Annealing time (minutes)	2	×	×	×
	4	×	×	×
	6	×	×	×
	8	×	×	×
	10	×	×	

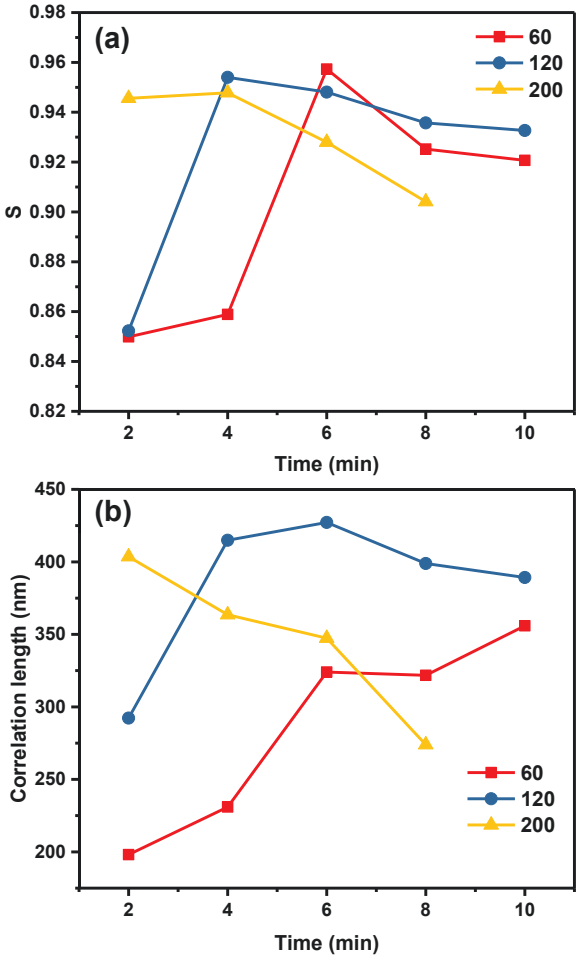

Fig. 6. 9 The annealing solvent volume and annealing time dependence of (a) orientation parameter and (b) correlation length.

The intensity of the first order peak in GISAXS at different azimuthal angles was used to obtain the orientation parameters, and the first order peak shape could be used to calculate correlation length. The Voigt function was employed to fit the first order peak at ψ = 0 to get the correlation length. The orientation parameter and correlation length at different annealing solvent volume and annealing time are shown in Fig. 6.9. The film is not in equilibrium right after solvent exposure. And it took short time to reach the

maximum orientation parameter when the volume increased. This is due to the diffusion limitation which can control the time needed for the film to reach equilibrium situation. The correlation length of the film annealed with 60 µl solvent is raising as a function of time from 200 to 350 nm. For 120 µl solvent, a peak value (430 nm) appears at 6 minutes which is delayed compared to the orientation parameter. The correlation length drops slowly when 200 µl solvent is taken. The correlation length alteration gives the clue that the film must absorb enough solvent to induce mobility and allow rearrangement of the morphology. AFM images provide the direct real space morphology and GISAXS data are obtained by probed big area. Based on those two methods, the annealing parameter, 120 µl and 6 minutes, were selected for the rest of the work.

During solvent vapor annealing, the drying process is found to be also important in determining the final morphology of the films. Four different processes have been studied: (i) the sample is taken out immediately, (ii) stays in the jar for 1 min, (iii) 2 minutes and (iv) is allowed to freely evaporate after 6 minutes annealing with 120 µl solvent. Those different processes mean different solvent removal rates. Fig. 6.10 shows the AFM phase images and the corresponding Fourier transform images of three films: taken out immediately, after 1 minute and after 2 minutes of storage in the jar after 6 minutes solvent vapor annealing. The film taken out immediately (Fig. 6.10 (a) and (d)) exhibits disordered structure and isotropic ring similar as in the prepared film. When the film stayed in the jar for 1 min, the finger print morphology and discontinuous ring indicates the rearrangement has taken place. A regular horizontal cylinder pattern is achieved after 2 minutes. And the difference between Fourier transform images also indicates that the order of the structure changes quickly in 2 minutes. Fig. 6.10 (g) shows the first order peak intensity profiles. It is hard to distinguish the peak in 0 min rest sample. The peak distribution curve becomes narrower and sharper after resting in the jar. After 2 minutes rest in the jar, the orientation parameter value (0.86) is higher than annealed 2 minutes followed by free evaporation (0.85, in Fig. 6.9 (a)).

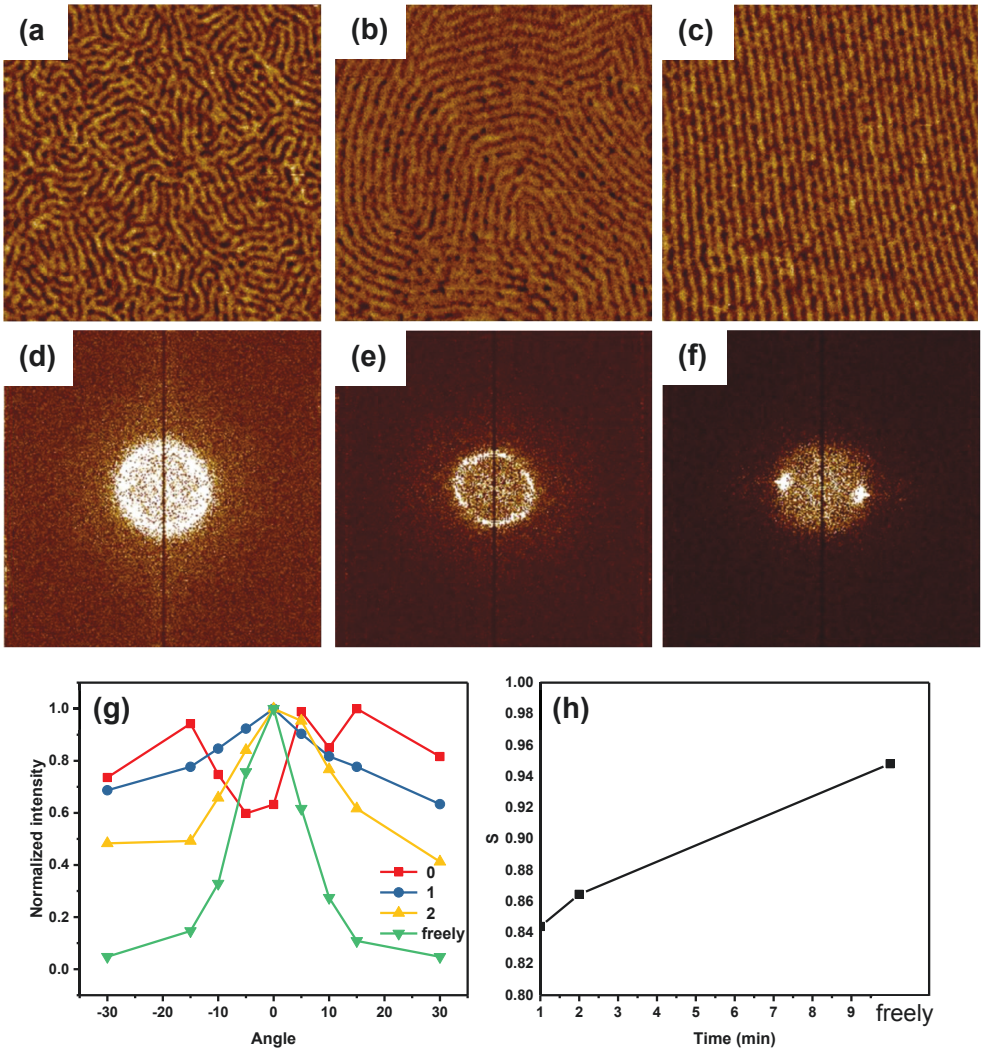

Fig. 6. 10 The AFM phase image and corresponding 2D Fourier transforms of sample resting in the jar for 0 min (a, d), 1 min (b, e) and 2 minutes (c, f) after 6 minutes solvent vapor annealing. The first order peak intensity profiles (g) and orientation parameter was obtained from the azimuthal angle dependent GISAXS.

6.3.5 3D structure

As an advanced thin film characterization method, GISAXS, provides two advantages: (1) average statistical information over the large illuminated area and (2) probed depth

as a function of the incident angle. GISAXS data were analyzed to obtain the lattice constants and the correlation length. While indexing the scattering patterns typically requires careful consideration of refraction and reflection interference, as for a qualitative evaluation of the reflection positions, a combination of Bragg's and Snell's laws was applied [24, 25]. The equation was derived on the base-centered orthorhombic lattice.

$$Q_z = k_{i,z} + \left\{\left\{(2\pi)^2 * \left(\frac{h^2}{a^2} + \frac{k^2}{b^2} + \frac{l^2}{c^2}\right) - Q_{||}^2\right)^{\frac{1}{2}} \pm \left[\left(k_{i,z}\right)^2 - \left(k_{Cfilm}\right)^2\right]^{\frac{1}{2}}\right\}^2 + \left(k_{Cfilm}\right)^2\right\}^{\frac{1}{2}} \quad (6.2)$$

$$k_{i,z} = \frac{2\pi}{\lambda} \sin \alpha_i \quad (6.3)$$

$$k_{Cfilm} = \frac{2\pi}{\lambda} \sin \alpha_{Cfilm} = \frac{2\pi}{\lambda}(1 - n_{film}^2) \quad (6.4)$$

Where $k_{i,z}$ is the Z component of the incoming wave vector in vacuum, and α_i is the incident angle. The Z component of the wave vector at the critical angle of the total external reflection, k_{Cfilm} in the polymer film, is related to the critical angles of total external reflectionα_{Cfilm} and the index of refraction n_{film}. The h, k, and l are the Miller indices in a base-centered orthorhombic lattice with lattice constants a, b and c. The position of $Q_{\|}$ was fit. From the equation 6.2, Q_z is strongly dependent on the incident angle. Incident angle dependent GISAXS (Fig. 6.11) were performed to obtain the structural and optical refraction information. When the incident angle changed from 0.1 ◦ to 0.145 ◦ and 0.18 ◦, the splitting of the Bragg peaks was observed. All features in GISAXS pattern obtained at 0.27 ◦ (Fig. 6.11 (d)) which was above the critical angle of sapphire (0.25 ◦) were located along Yoneda line. Above the critical angle of the substrate, parts of the primary beam will penetrate nanocomposite film but also the substrate. In the figure, it is not really a Yoneda line, but a band which indicates the contribution from the scattering angle α_f between the critical angle of the film and the substrate. The first Bragg peak is at Qy = 0.0223 Å^{-1} which is used to determine a lattice constant a = 28.2 nm ($a = 2\pi/Q_y$). The line cuts at Qy = 0.0223 and 0.0446 Å^{-1} along Qz direction show the tendency of Bragg peak positions changing following the increasing of the incident angle.

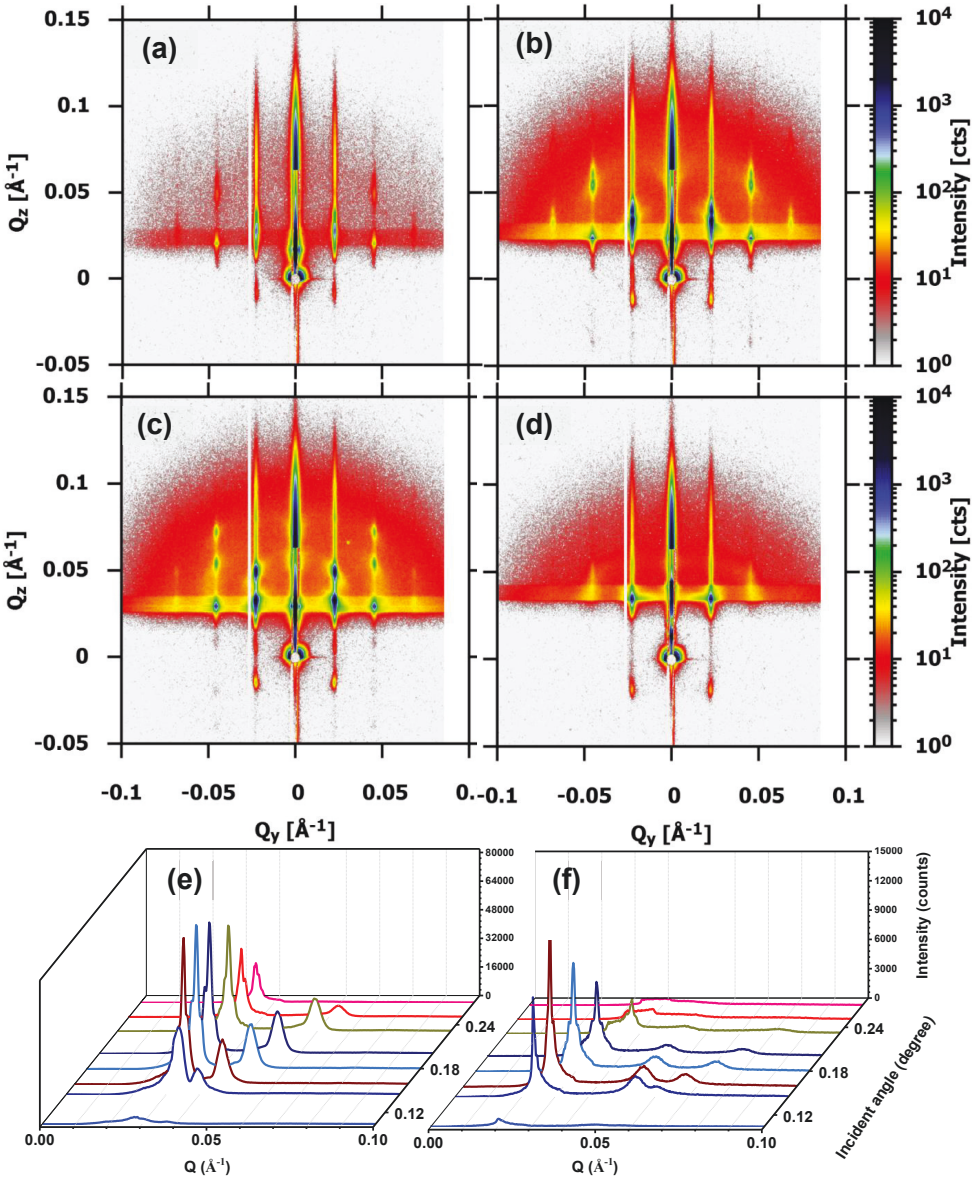

Fig. 6. 11 GISAXS measurements at different incident angles (a) 0.1 °, (b) 0.14 °, (c) 0.18 ° and (d) 0.27 °. The line cuts along Qz direction at Qy (e) first peak 0.0223 Å^{-1} and (f) second peak 0.0446 Å^{-1}.

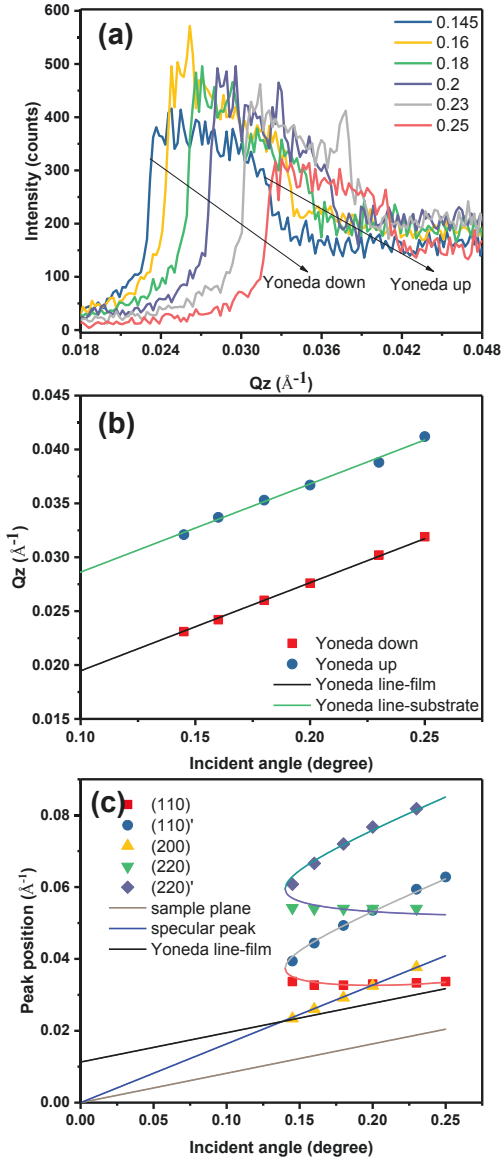

Fig. 6. 12 (a) The Yoneda band position changes with the incident angle (b) the position fitting of Yoneda line and (c) the indexing of the nanocomposite film. Theoretical

positions of sample plane and specular peak are indicated as grey line and blue line, respectively.

According to the scattering setup and geometry, the change of incident angle was achieved by rotating sample while the primary beam was fixed. The following equations were obtained:

Sample plane: $Q_{plane} = \frac{2\pi}{\lambda} \sin \alpha_i$ (6.5)

Specular peak: $Q_{specular} = 2 * \frac{2\pi}{\lambda} \sin \alpha_i$ (6.6)

Yoneda line of film: $Q_{Cfilm} = \frac{2\pi}{\lambda} \sin \alpha_i + \frac{2\pi}{\lambda} \sin \alpha_{Cfilm}$ (6.7)

Yoneda line of substrate: $Q_{Csubstrate} = \frac{2\pi}{\lambda} \sin \alpha_i + \frac{2\pi}{\lambda} \sin \alpha_{Csubstrate}$ (6.8)

As the Yoneda band contains the contribution from the scattering angle α_f between the critical angle of the film and the substrate, the down and up limitations of Yoneda band are useful to determine the critical angle of the film and the substrate. The shift of Yoneda band is presented in Fig. 6.12 (a). The equation 6.7 and 6.8 are employed to fit the critical angle (Fig. 6.12 (b)). The critical angles are 0.138 ± 0.001 ◦ and 0.249 ± 0.001 ◦ for the nanocomposite film and the sapphire substrate, respectively. The fitting result of the sapphire is consistent with the theoretical prediction. The fitting of the peak position based on the equation 6.2 are shown in Fig. 6.12 (c). Only the data above the critical angle of the film and under the critical angle of substrate are used. In agreement with all peak positions, the lattice parameter of b = 29.4 ± 0.5 nm and the critical angle of the nanocomposite film $\alpha_{Cfilm} = 0.14 \pm 0.001^{o}$ are determined. The critical angle of the nanocomposite film obtained from two fitting equations is in a good agreement with each other.

6.3.6 BornAgain Simulation

In order to obtain the quantitative analysis of GISAXS data, the GISAXS pattern of the nanocomposite film was simulated using the Distorted Wave Born Approximation (DWBA) formalism implemented in the program BornAgain. 2D GISAXS pattern was simulated directly, and horizontal and vertical line cuts were obtained from 2D images. The film was modeled as one mesocrystal on a substrate. No interference function was used during the simulation which means there is no decay function. Considering the limited resolution of GALAXI instrument, the film is defined by one mesocrystal with width: 500 nm, length: 500 nm and height: 150 nm as primary parameters. The mesocrystal is composed of iron oxide nanoparticles, PS cylinders and P4VP(PDP)1.7 matrix as shown in Fig. 6.13. The lattice parameters are defined by using results of

GISAXS indexing (a: 28.2 nm, b: 29.4 nm). The mean diameter of the nanoparticles (5.6 nm) and the size distribution (PD: 0.13) are obtained from the SAXS measurements. The size distribution is not taken into account during simulations. The PS cylinder diameter was set to 10 nm [26]. Refractive indexes (Table 6.2) of all materials were calculated based on the elements and densities. From the information in Table 6.2, the contrast mainly comes from the difference between nanoparticles and whole polymer film. The rough substrate is used instead of the patterned substrate to simplify the sample model.

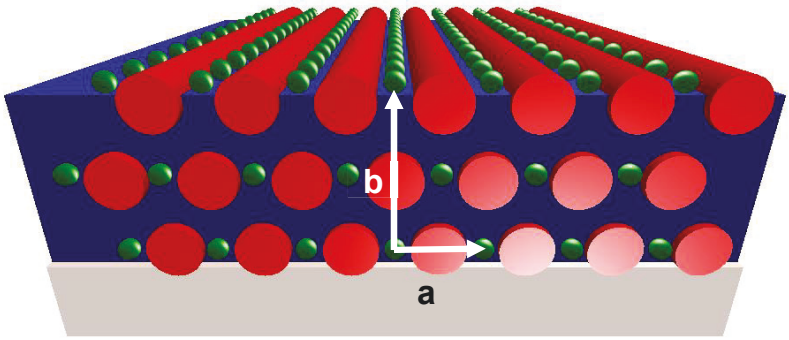

Fig. 6. 13 The schematic drawing of the sample model. In this schematic, the PS cylinder is in red and the P4VP(PDP)x matrix is in blue and nanoparticle is in green.

Table 6. 2 Refraction index ($n = 1 - \delta + i\beta$)

materials	δ	β
Fe_2O_3 nanoparticle	1.20 e-05	8.34 e-07
PS cylinder	2.61 e-06	2.78 e-09
P4VP(PDP)1.7 matrix	2.6 e-06	3.0 e-09
Sapphire substrate	9.57 e-06	8.46 e-08

In order to simulate the effects of the instrument resolution, the wavelength was set as 1.34 Å without any distribution. The beam divergence is neglected during simulations. The resolution function of the detector is chosen to be 2D Gaussian. For the scattering background, the constant background is set as 2 counts per pixel.

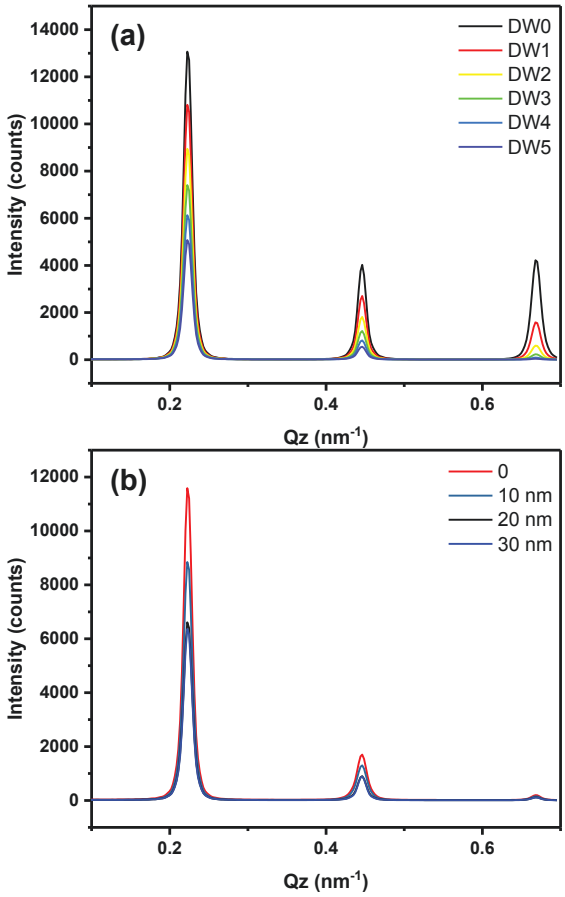

Fig. 6. 14 Different (a) DW factors and (b) roughness of simulation based on the sample model.

The main reason that could cause the decay of scattering intensity with Q observed in our samples is the roughness of the substrate, film thickness variations and the nanoparticles position uncertainty. To find patterns highly similar to the experimental GISAXS patterns, those three parameters were tuned in a reasonable range. Usually, Debye-Waller (DW) factor [27] is used to describe the attenuation of x-ray scattering caused by thermal motion. In this simulation, Debye-Waller factor is used to describe the displacement of nanoparticles around the lattice points in 3D. For more details, the settings can be found in the appendix. Different DW factors and roughness are

simulated to provide an insight into how sample quality causes the scattering pattern change. The average displacement of nanoparticles is the square root of DW factor. By increasing the DW factor from 0 to 5, the intensity drops quickly with Q (Fig. 6.14 (a)). DW factor only influences the intensity. By varying roughness from 0 to 30 nm, the results show that the roughness can decay the intensity and the difference between 20 nm and 30 nm is very small (Fig. 6.14 (b)).

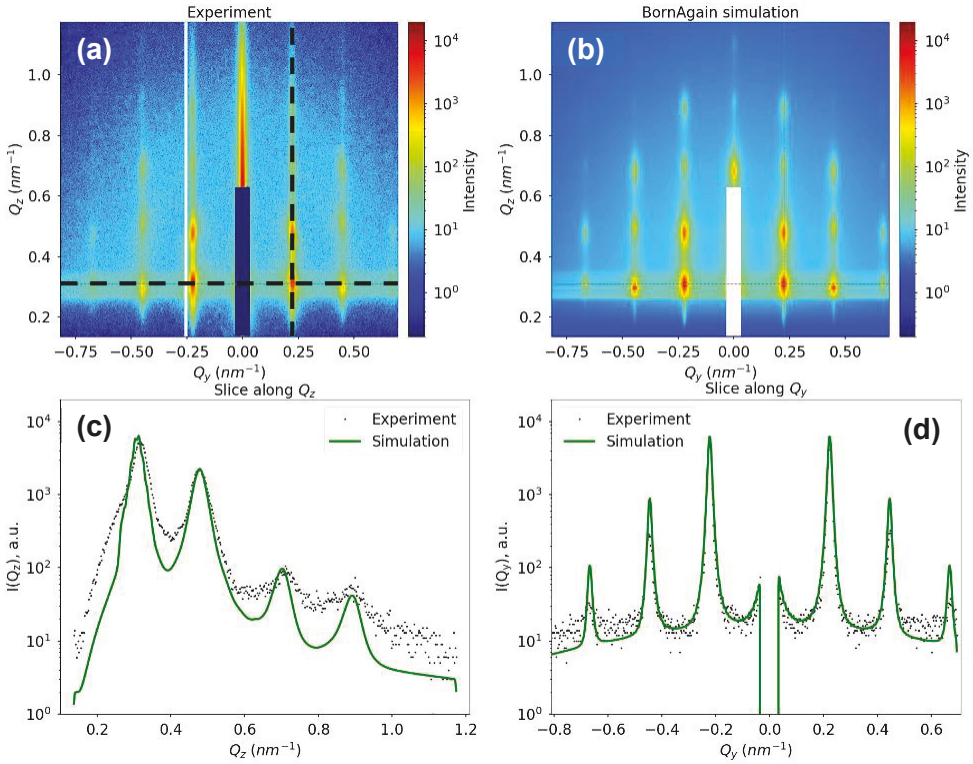

Fig. 6. 15 (a) The experimental data, (b) DWBA simulation with DW factor 3.8 and roughness 30 nm. Line cuts along (c) Qz = and (d) Qy = direction.

By carefully comparing the line cut along Qz direction, DW factor 3.8 was selected. The calculated amplitude of substrate sap1500 is 29.6 nm. In the optimized simulation, the roughness was set as 30 nm. All main parameters involved in this fitting are listed in the Table 6.3. The 2D GISAXS pattern of the film annealed with 120 µl chloroform for 4 minus was chosen for the simulation. According to such a model, the 2D pattern could be reproduced as shown in Fig 6.15(b). The simulation yields values of 90 nm for the average height and 500 nm for the width of the mesocrystal. Those two values

corresponded to the average correlation length in Qz and Qy direction. Considering the thickness variance, the height of the mesocrystal is described as a distribution from 30 nm to 150 nm. The vertical (Fig 6.15(c)) and horizontal (Fig 6.15(d)) line cuts at the positions are indicated as dash lines. The Qy lines cut of experiment and simulation are perfect overlapping. The peak positions are decided by the mesocrystal lattice and the height and width of mesocrystal determing the peak shape. Based on the DWBA simulation results, this one mesocrystal model can be used to decribe the sample properly and study the correlation length in-plane and out-of-plane quite well. The fitting script can be found in appendix C.

Table 6. 3 Main parameters involved in the fitting.

Parameter		Value	State
Film size	thickness	90 nm (averaged)	fitted
	width	500 nm	fitted
Lattice parameter	a	28.2 nm	fixed
	b	29.4 nm	fixed
nanoparticles	size	5.6 nm	fixed
	polydispersity	0.13	fixed
Roughness of substrate		30 nm	fitted
DW factor		3.8	fitted

6.3.7 Magnetic properties

From the temperature- and field-dependent magnetization measurements of dryed ON5 nanoparticles suspension on a Si substrate in chapter 4, the blocking temperature is found to be around 14 K in ZFC/FC magnetization curves measured at 200 Oe. At 300 K the ON5 nanoparticles are in a superparamagnetic state. Below the blocking temperature, at 5 K we found a coercive field of ~60 Oe. After ON5 nanoparticles are embeded in the block copolymer matrix, the unidirectional structure is achieved by solvent vapor annealing. To investigate the magnetic behaviors of the hybrid films, a Quantum Design magnetic property measurement system (PPMS) of Dynacool magnetometry was used. During magnetization measurements, the field was applied along two directions, parallel and perpendicular to the PS cylinders, in order to check whether the anisotropic structure resultes in magnetic anisotropy.

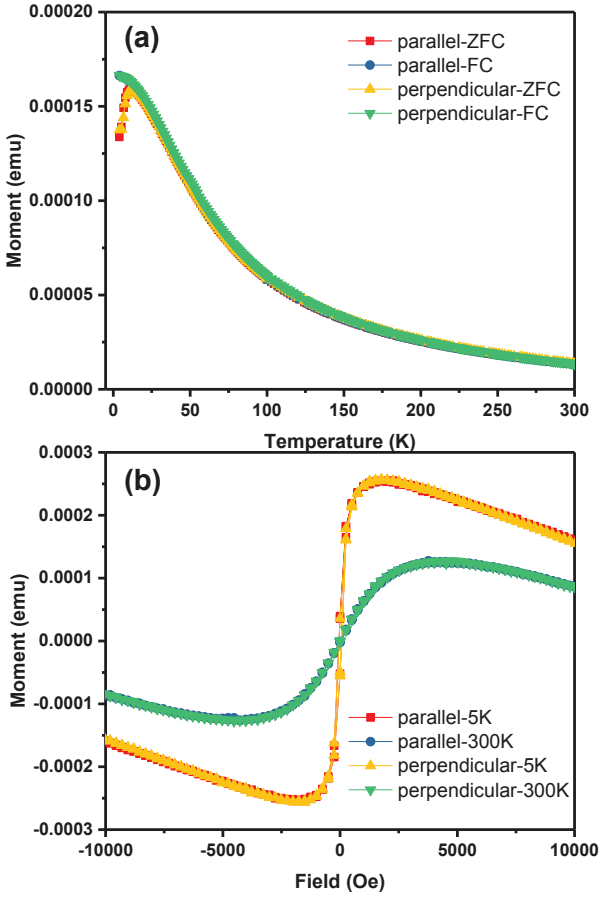

Fig. 6. 16 Magnetic moments measured as a function of (a) temperature and (b) the external magnetic field at directions of parallel and perpendicular to the PS cylinders.

Fig. 6.20 shows the temperature- and field-dependent magnetization measurements of the nanocomposites film. The temperature- and field-dependent curves are independent of the measurement direction. The blocking temperature is around 12 K in ZFC/FC magnetization curves measured at 200 Oe and a coercive field of ~60 Oe is found which are consitent with the results obtained from dryed ON5 nanoparticles. The behaviour of nanocomposite film is nearly the same as for free ON5 nanoparticles. The blocking temperture decreased down to 12 K, which might be a result of the magnetic dipolar interactions [28]. The dipolar interaction was much weaker in nanocomposites

films (corresponding energies of less than 1 K) with large particle-to-particle separation than in closely packed ensemble of nanoparticles (~ 20 K). As the magnetic dipolar interaction decreases, it is easier to break the blocked state and to reduce the blocking temperature. The field-dependent magnetization curves decay at high external fields region which is due to contribution from the diamagnetic sapphire substrate. The nanocomposite film still followes a superparamagnetic behavior at room temperature. Based on the magnetic measurements results, the estimated ON5 nanoparticles concerntration in the polymer matrix is ~5 wt % which is closed to desired value 8 wt %.

6.4 Summary

In the present chapter, nanocomposite films consisting of ON5 nanoparticles and structure guiding PS-P4VP(PDP)1.7 matrix were systematically studied with SEM, AFM, GISAXS, and magnetization measurements. After properly selecting the film preparation parameter, the film (thickness under 200 nm) could be fabricated by spin coating the supramolecular solution on the sap1500 substrate at 50 rps. The solvent vapor annealing process was explored. By varying the solvent volume and the annealing time, different morphologies were obtained. The azimuthal angle dependent GISAXS were employed, which provided the progress of solvent vapor annealing, including characterization of the orientation and correlation length. The orientation parameter and the correlation length could quantify the nanocomposite film quality. Meanwhile, the slowly drying process was also very important. A highly-ordered alignment of the nanoparticles in the block copolymer matrix was achieved via solvent vapor annealing in the jar with 120 µl chloroform for 6 minutes followed by freely evaporating. The optimized film had a high orientation factor as 0.94. These results illustrate that faceted patterned surfaces are effective in guiding NP assemblies normal to the substrate surface and can lead to hierarchically structured nanocomposite thin films with tunable directional properties over macroscopic distances to meet material needs for a wide range of NP-based devices.

As for a qualitative analysis of the GISAXS data, a combination of Bragg's and Snell's laws is applied to base-centered orthorhombic lattice. The critical angle of the nanocomposite film is 0.14 ± 0.001°. The lattice constants are a = 28.2 nm and b = 29.4 nm. The GISAXS data was simulated based on the DWBA theory for a quantitative understanding by the software package BornAgain, and the correlation length in-plane (500 nm) and out-of-plane (90 nm) are obtained from the simulation. The analysis of the GISAXS data provided valuable information for the rational design of nanomaterials. Notably, whether embedded or not, it did not change the magnetic properties which is quite interesting for the applications. The fabricated hybrid films are superparamagnetic, have no clear anisotropy, for potential applications in fields as diverse as magnetic sensors, and magnetic memory devices.

Chapter 7 Neutron scattering studies of magnetic and structural proprieties of nanocomposite films

7.1 Introduction

The doping of a block polymer matrix with magnetic nanoparticles produces nanocomposite materials with interesting magnetic properties, which can be used in applications such as magnetic sensors, target drug delivery, catalyst and magnetic storage devices [1-6]. By selectively depositing magnetic nanoparticles into one block of the block polymer matrix, a highly-ordered nanoparticles distribution within the polymer film could be achieved by thermal or solvent vapor annealing [7-9]. The film structure could be probed by using real-space techniques, such as atomic force microscopy (AFM) and scanning electron microscopy (SEM), and reciprocal-space scattering techniques, such as grazing incidence small angle x-ray scattering (GISAXS). However, these general methods are not sensitive to the magnetic order and magnetic correlations of nanoparticles within the block polymer matrix. Neutron scattering has been proven to be a very powerful tool for the investigation of magnetic materials because of the particular interaction of the neutrons with magnetic moment, described in details in chapter 2. Neutron scattering has the capability to distinguish protonated and deuterated polymers because of the large difference in scattering length between H and D (H: -3.74×10^{-6} Å^{-1}, D: 6.67×10^{-6} Å^{-1}). This is important for the contrast variation measurements and for reduction of the incoherent scattering from hydrogen, which is dominant in protonated block polymer samples. Moreover, polymer materials are not affected by radiation damage when probed with neutrons, in contrast to measurements using intense synchrotron beams.

The enhancement of the surface sensitivity by grazing incidence geometry, reflectivity and grazing incidence small angle neutron scattering is a powerful combination for investigations of nanostructures in thin films [10-12]. The neutron beam impinges onto the sample surface at a shallow incident angle, and the scattered intensity is collected using 2D detector to detect the signal at a different exit and an out-of-plane angles. We employed scattering methods for obtaining insights into the in- and out-of-plane structure of the nanocomposite film on a patterned sapphire substrate. We combined

grazing incidence small angle neutron scattering with polarized incident beam (PGISANS) and polarized neutron reflectometry (PNR) to access the information about structural arrangement of nanoparticles over a wide range of length scales in the lateral and transverse directions. The aim of our neutron studies is to investigate the magnetic structure of this new family of functional magnetic materials. The combination of neutron scattering results with x-ray scattering results and real-space techniques will help us to better understand the structure-property relationships in our samples.

7.2 Methods

7.2.1 Sample preparation

The deuterated Poly(styrene-b-4-vinyl pyridine) (dPS-b-P4VP) (number average molecular weight, MnPS = 19.5 kg mol^{-1}, MnP4VP = 5.5 kg mol^{-1}, Mw/Mn = 1.08, where Mw is the average molecular weight) and protonated Poly 4 Vinyl pyridine were purchased from Polymer Source (Montreal, Canada). The supramolecule solution was prepared by dissolving the appropriate amounts of dPS-b-P4VP di-block copolymer and PDP in chloroform (see chapter 6). Thin films were prepared by spin-coating the mixed solutions onto sap1500 (12 x15 mm) substrates with spinning speeds of 50 rps. For solvent annealing, samples were annealed using 120 µl of $CHCl_3$ injected inside a 100 ml top-capped jar at room temperature for 6 minutes. Once the solvent vapor annealing was completed, the vial was opened and the chloroform solvent vapor in the vial was allowed to freely evaporate. This optimized sample preparation process is described in chapter 6.

7.2.2 Experimental setup

The magnetic reflectometer with high incident angle (MARIA [14]), which is operated by JCNS at MLZ in Garching, was designed for the investigation of thin magnetic layered structures down to the monolayer scale. MARIA can be used in the reflectometer mode for studies of the lateral structures and GISANS mode with additional resolution in the perpendicular direction. Before GISANS and NR measurements, the sample position needs to be aligned. The sample was placed on a custom designed hexapod stage which can be moved both horizontally and vertically as well as tilted to specific angles. A preliminarily estimation of the sample position was done by using the laser to adjust the sample surface parallel to the beam. After this, the alignment was carried out using the neutron beam. By rotating the sample around the X and Y axis (see Fig.7.1), the sample was tuned complete parallel to the incident neutron beam. A series of scans through the sample height and angle were carried out, counting the neutron intensity at each point. The goal was to put the sample in the beam and find the position of the

sample at which the incident beam angle was 0 °. By changing the instrument measurement mode, MARIA is capable of collecting the GISANS and NR data. The incident beam is in the X axis and the applied field is along Y axis. The scattering vector Q is out of plane, along with Z axis. The wavelength resolution ($\Delta\lambda/\lambda$ at 6 Å) of MARIA is 10 % which typically ensures sufficient neutron flux.

To achieve the Qy resolution necessary for GISANS experiments, a narrow bar-shaped neutron beam must be used instead of the rectangular beam used for reflectivity experiments. In order to achieve that for GISANS experiment a cadmium mask was used. Its purpose is to cover the cold finger and reduce ambient neutron background. Only the direct beam, which passes through the sample and the sample holder in GISANS measurements, needs to be shielded with a beam stop to improve the background scattering from the detector.

The instrumental settings for PGISANS were as follow: wavelength of 6 Å ($\Delta\lambda/\lambda$: 10 %), 2 m for sample-detector distances, slit size of 2 mm x 8 mm and 0.6 mm x 8 mm and detector pixel size 0.6 mm x 0.6 mm, counting time 5 hours for polarizer flipper up and down state at 0.5 T. The instrumental settings for PNR were as follow: wavelength of 6 Å, slit size 0.6 mm x 42 mm, 2 m for sample-detector distances, slit size of 2 and 0.5 mm counting time 5 minutes for each point with polarizer flipper up and down, analyzer flipper up and down at different fields.

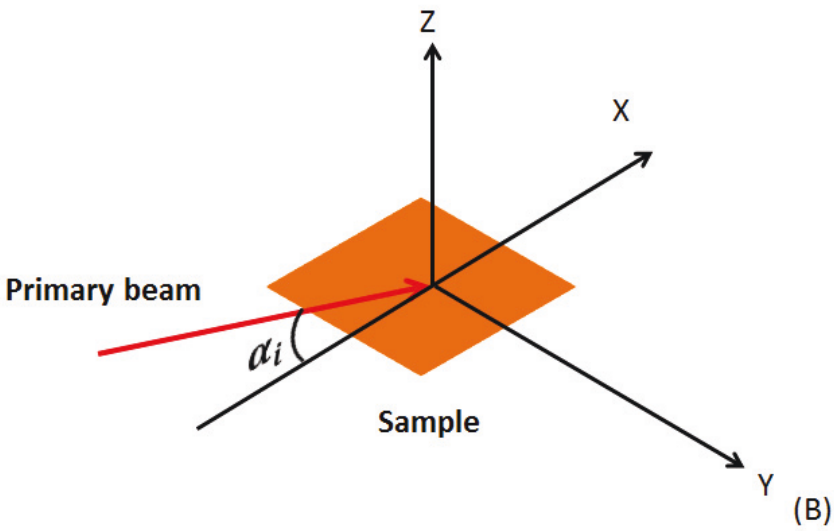

Fig. 7. 1 The scattering geometry of GISANS and PNR.

7.3 Results and Discussions

7.3.1 NR and GISANS of the empty substrate

The aim of these measurements is to characterize the empty substrate with neutron scattering, in order to identify the main scattering features of the substrate. This, in turn will simplify the analysis of the scattering data from an actual nanocomposite film.

We start discussion of with expected scattering features that follow from the scattering theory, described in Chapter 2. In a theoretical off-specular reflectivity map, there are several common trajectories: reflected, refracted and direct beam, as depicted in Fig. 7.2(a). The first one corresponds to $\alpha_f = 0$ and is traditionally referred to as the sample surface named as horizon in Fig. 7.2 (a). The specular reflectivity appears when $\alpha_f = \alpha_i$. The direct beam is found in the position of $\alpha_f = -\alpha_i$. The refracted beam shows a more complex trajectory, since below the critical angle, all neutrons have been reflected at the air-sample interface, $\alpha_{f,refracted} = 0$. Above the critical angle, neutrons start to penetrate inside the sample and there is a significant refraction. Moreover, for large incidence angles, the refraction effect becomes negligible, $\alpha_{f,refracted} \approx \alpha_i$, and the refracted and the direct beams overlap.

The measured off-specular map of the empty patterned sapphire substrate is shown in Fig. 7.2 (b). The measured map matches the theoretical trajectories quite well. The critical angle of sapphire is 0.46 ◦, as estimated from the equation 2.39. Above the critical angle of sapphire, neutrons penetrate inside the sample and substrate and the specular peak intensity significantly decreases. The Yoneda wings are clearly seen in the Fig. 7.2 (b). They are located at the critical angle of total reflection. The critical angle obtains from the off-specular map was 0.43 ± 0.005 ◦. The intensity enhancement of Yoneda wings in the diffuse map is due to the increase of the transmission coefficient at this angle.

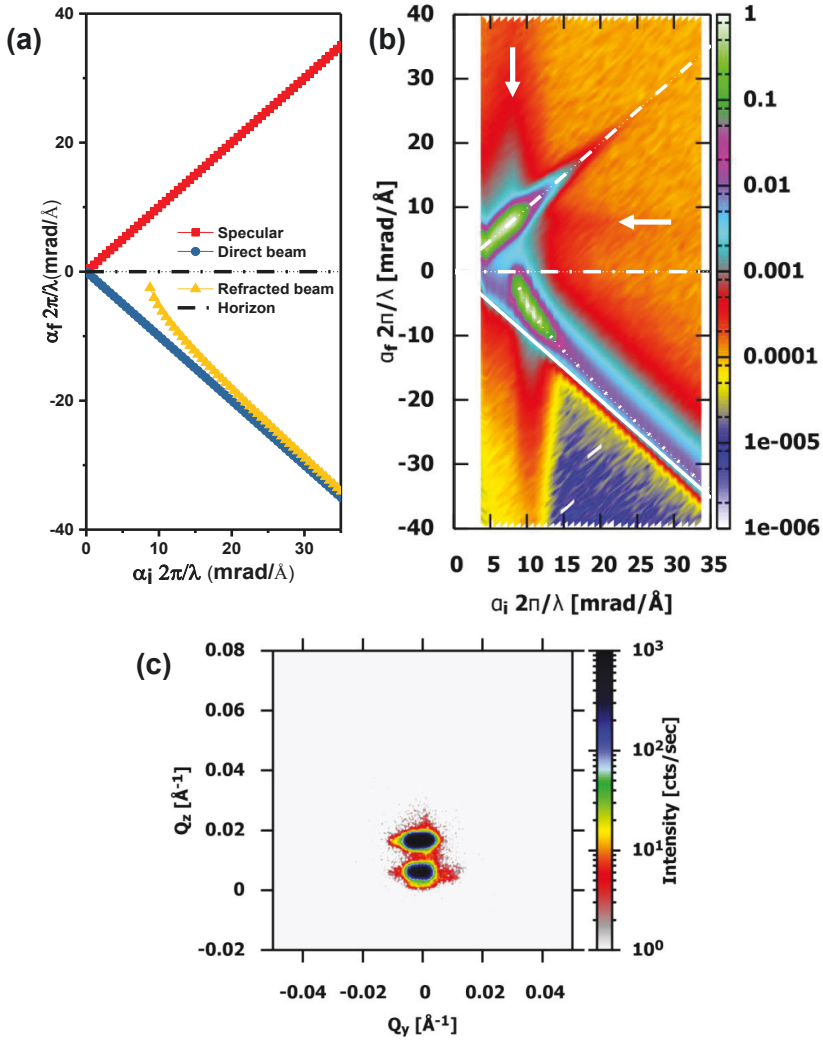

Fig. 7. 2 (a) The theoretical key trajectories in an off-specular reflectivity measurement: reflected, refracted and direct beam. (b) The off-specular map: specular is dashed line, direct beam is solid line, refracted beam is dotted line, and horizon is dashed-dotted line. The Yoneda wings are indicated with arrows. (c) The GISANS measurements of the empty patterned sapphire substrate.

7.3.2 Deuterated nanocomposite structure

In order to avoid background due to incoherent scattering from hydrogen, deuterated block copolymer was used for the sample preparation. The number average molecular weight of the deuterated block copolymer (dPS-b-P4VP) was chosen carefully to match the structure of the block copolymer (PS-b-P4VP) in chapter 6, there were some difference in number average molecular weight and Mw/Mn ratio. In order to compare the structural differences, pure polymer matrices without nanoparticles were synthesized. Two of the reference pure polymer matrix films were prepared and annealed using parameters described in chapter 6 (spin coating: 5µl, 50 rps; annealing: 120 µl, 6 minutes). The deuterated and nondeuterated versions of the same sample were synthesized as well, in order to confirm the structural integrity during deuteration. The AFM phase images of the pure polymer matrix films are shown in Fig. 7.3. The number of repetitions of PS cylinders is 28 ± 1 and 32 ± 1 for deuterated and nondeuterated pure polymer matrix, respectively. By using the AFM images, the estimated periods are 35 ± 2 and 31 ± 2 nm.

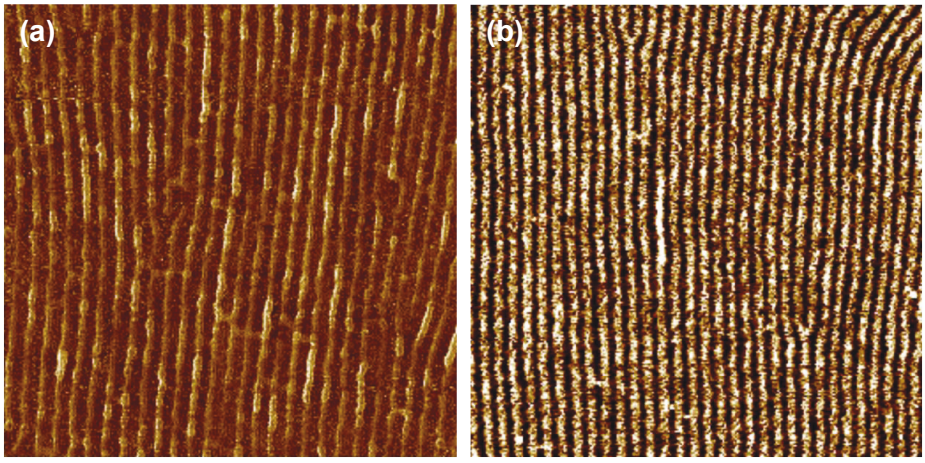

Fig. 7. 3 The AFM phase images of the (a) pure deuterated film and (b) nondeuterated polymer film. The scan size was 1 x 1 µm.

In order to see if deuteration of the films causes any structural changes as compared to nondeuterated (protonated), the deuterated nanocomposite film was prepared by using supramolecule solution with 8 wt % nanoparticles. The AFM phase image of deuterated nanocomposite film is shown in Fig. 7.4 (a). The incident angle dependent GISAXS measurements were performed. As shown in chapter 6, the Yoneda band could be efficiently used to obtain the critical angle of the film under study. The bottom position of Yoneda band was fitted using equation 6.6 (see Fig. 7.4 (b)). The critical angle obtained

from this fit is 0.145 ± 0.001 °. Similar to the analysis presented in chapter 6, for a qualitative evaluation of GISAXS data, the GISAXS data was treated using the combination of Bragg's and Snell's laws. The first Bragg peak is at Qy = 0.0196 Å^{-1} which corresponds to a lattice constant of a = 32 nm ($a = 2\pi/Q_y$). The peak positions at Qy equal to 0.0196 and 0.0392 Å^{-1} along Qz direction show the tendency of Bragg peak positions to shift with increase of the incident angle. All the fitting processes were applied to GISAXS data as described in chapter 6. The lattice parameter of b = 31.5 ± 0.5 nm is found, in agreement with all peak positions. Table 7.1 summarizes the results of fitting for the deuterated and nondeuterated samples. Clearly, the deuterated block polymer has a similar, but slightly larger framework as compared to the nondeuterated one.

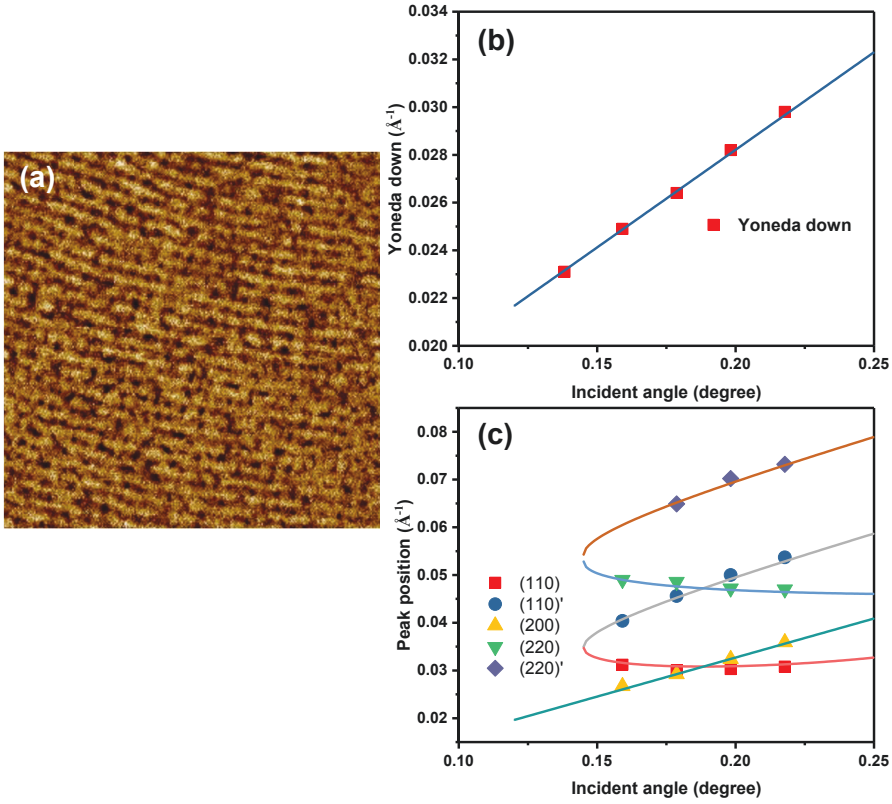

Fig. 7. 4 (a) The AFM phase image of deuterated nanocomposite film (scan size 1 x 1 μm). (b) The position fitting of Yoneda line. (c) The indexing of the nanocomposite film.

Table 7. 1 The lattice parameter and critical angle of deuterated and nondeuterated nanocomposite film derived from the fits.

	Nondeuterated film	Deuterated film
a (nm)	28.2	32
b (nm)	29.4 ± 0.5	31.5 ± 0.5
α_{Cfilm}	0.140 ± 0.001 °	0.145 ± 0.001 °

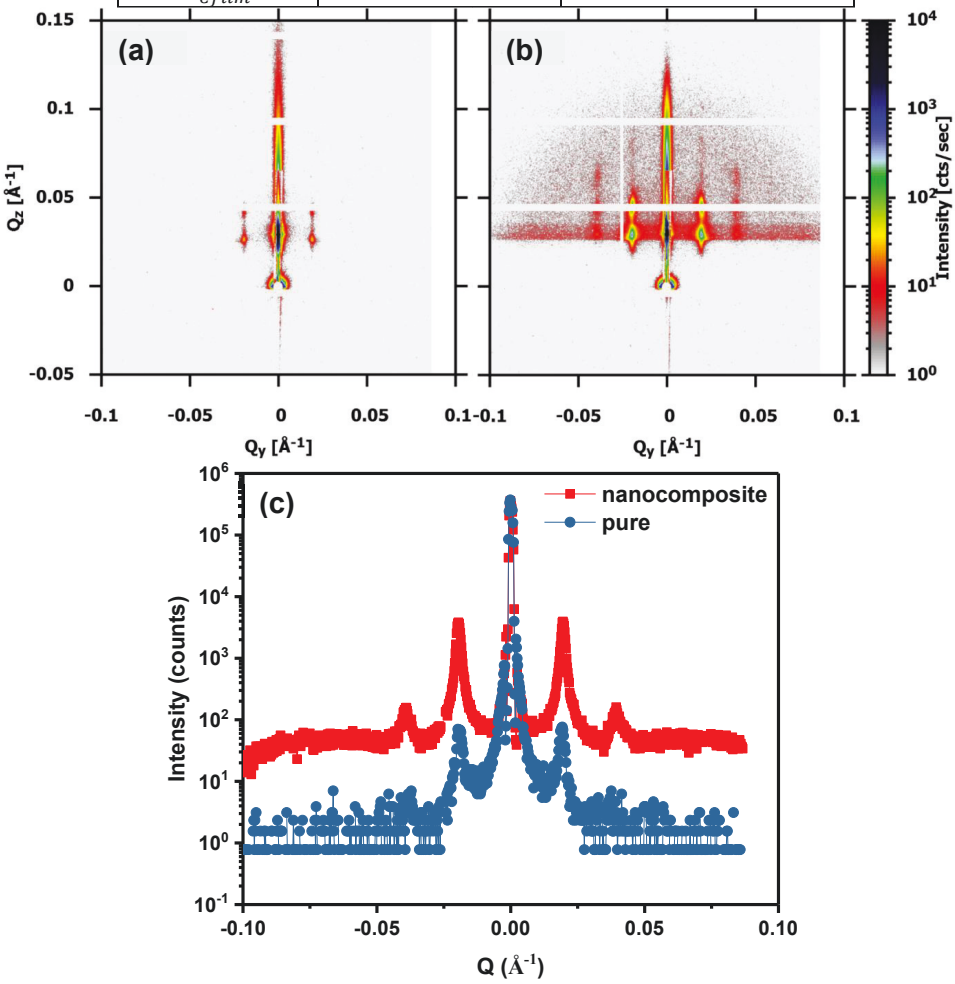

Fig. 7. 5 GISAXS data of pure polymer film (a) and nanocomposite film with 8 wt % nanoparticles (b). (c)The line-cut of those two data along Yoneda line.

In order to compare the contribution in the scattering, GISAXS measurements were employed. The GISAXS data of pure deuterated polymer film and nanocomposite film with 8 wt % nanoparticles are shown in Fig. 7.5. The incident angle was fixed as 0.2 ^{o}. As the nanoparticles have been doped in the nanocomposite film, more Bragg peaks show in the GISAXS map (in Fig. 5(b)) and the intensity also increase. The similar GISAXS map reveals that nanoparticles are located between deuterated PS cylinders. The line-cut along Yoneda line shown in Fig. 5(c) give a clear view of Bragg peak position and intensity profiles. The first Bragg peak of two GISAXS are at Qy = 0.0196 $Å^{-1}$. This demonstrates that the framework of polymer matrix remains the same after doping nanoparticles. And integrated intensity of first Bragg peak are 1035 and 41087, respectively. The x-ray SLD of nanoparticles and deuterated polystyrene are 42 x 10^{-6} and 9 x 10^{-6} $Å^{-2}$, respectively. The integrated intensity ratio is 1:39 which indicates that nanoparticles dominate the scattering process during GISAXS.

7.3.2.1 Uniformity check of sample by GISAXS

The sample of a larger size (12 x 15 mm) was used in the neutron scattering experiments in order to increase signal-to-background ratio. In order to check homogeneity of the sample, i.e. ensure that various parts of the sample are structurally similar, a number of GISAXS measurements were taken at various positions on the sample surface. The process included moving the sample along Y axis direction with finite steps and the intensities were collected. Fig. 7.6(a) shows the integrated scattering intensity as a function of the sample position along Y axis. The different positions (Py = -4, -2, 0, 1, 3, 5 and 7 mm) were chosen to perform actual GISAXS measurements marked as red stars in Fig. 7.6(a). The line cuts along Qy direction at Yoneda band of different GISAXS measurements are presented in Fig. 7.6(b). The line cut of Py = 7 mm, which is the edge of the sample, is different from others, because of substrate edge effects. During spin coating, surface tension makes it difficult for solution that is flowing radially outward to separate from the substrate. Thus a small amount of liquid can stay attached around the entire edge and result in thicker coatings in the edge. The 2D GISAXS of Py = -4, 1, 3 and 7 mm are depicted in Fig. 7.6(c-f). The data provide clear evidence that the sample structure is uniform within the area of 2 mm x 8 mm, which corresponds to the size of the neutron beam used in GISANS measurements.

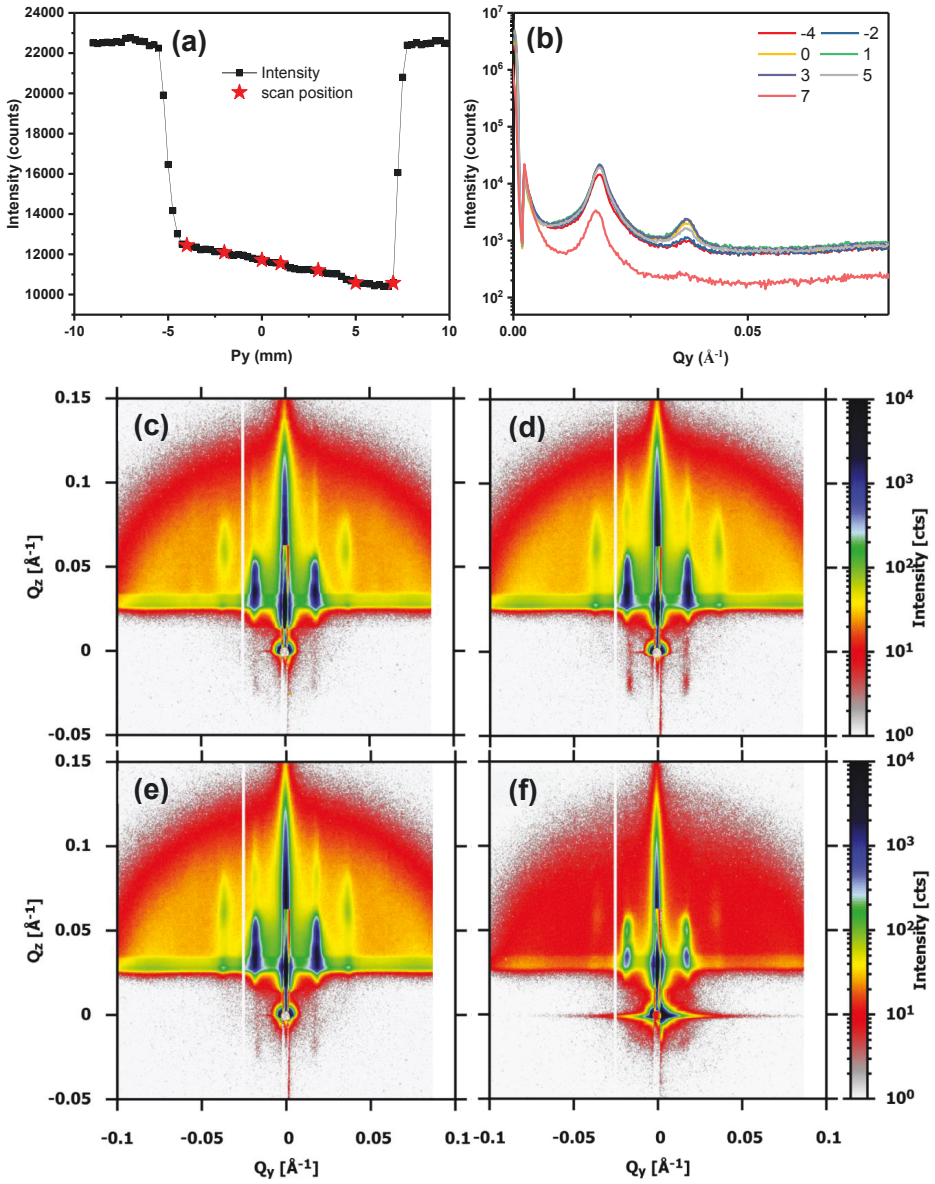

Fig. 7. 6 (a) The intensity as a function of Y position, (b)the line cut along Yoneda line 2D GISAXS pattern at Py = -4 mm (c), 1 mm (d), 3 mm (e) and 7 mm (f).

7.3.3 Neutron scattering results

The following section documents the neutron scattering experiments on the samples. The main results and experimental challenges are described. In the last chapter of this work, we will present an outline of how the experimental conditions might be improved for obtaining a higher quality data.

All SLDs [14] of compositions in the film are shown in Table. 7.2. After the deuteration, the SLD of PS block changes drastically and provides a sharp contrast for the neutron scattering experiments. In order to avoid any issues with aging of the sample, we prepared a fresh sample using exactly the same preparation procedure for each neutron beamtime.

Table 7. 2 The SLD of different component in the nanocomposite film.

		SLD nuclear($Å^{-2}$)	SLD(-i $Å^{-2}$)
PS	C8D8	5.72e-06	4.79e-13
	C8H8	1.34e-06	4.32e-11
P4VP(PDP)1.7	4VP	1.68e-06	6.69e-11
	PDP	1.93e-07	6.01e-11
Fe_2O_3		7.17e-06	2.81e-10
Al_2O_3		5.71e-06	3.02e-11

7.3.3.1 GISANS

The first GISANS beamtime was a feasibility test aimed to probe the interactions between 3D magnetic nanoparticles in order to better understand the resulting magnetic structure of nanocomposite films. The scattering geometry of GISANS is shown in Fig. 7.1. The sample alignment in reflection mode had started with a wavelength of 4.5 Å and several test measurements were performed in order to choose the proper incident angle. From the SLD of sapphire ($\alpha_c = \lambda\sqrt{\rho/\pi}$), the critical angle of this substrate was estimated to be 0.35 ◦ (λ = 4.5 Å). The GISANS measurements (Fig. 7.7) were carried out with a set of incident angle changing from 0.2 to 0.5 ◦ for 30 minutes in each configuration. As the incident angle is above the critical angle of the substrate (Fig. 7.7 (c) and (d)), partial neutron beam will transmit through the substrate. By comparing Fig. 7.7 (b) and (c), the scattering features are different because of less neutrons being reflected by the film.

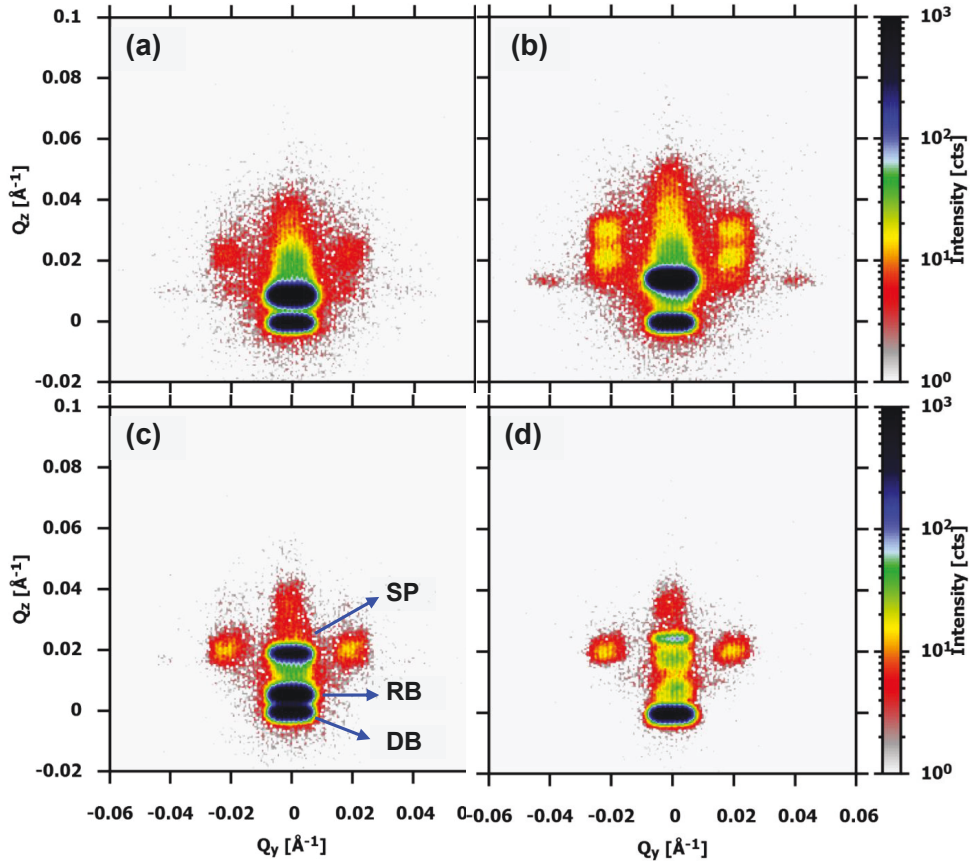

Fig. 7. 7 The GISANS data taken at incident angle of (a) 0.2 (b) 0.3 (c) 0.4 and (d) 0.5 °. The specular peak (SP), refracted beam (RB) and direct beam (DB) are indicated with solid arrows.

We chose the smaller step of 0.01 ° in the region of 0.3 to 0.35 ° in order to define the critical angle more precisely. The line cuts along the off-specular line are shown in Fig. 7.8(a). The transmitted beam could be clearly observed from 0.32 ° and its intensity increases with the change of incident angle. The 0.31 ° is the limit of the incident angle at which neutrons travel into the film and are reflected at the interface between film and substrate. Additionally, we found the specular peak position is not exactly the two times of the incident angle. This means the sample is slightly misaligned by at least ~0.01 °, which is not considered during the following measurements. The limitation of incident angle which could be used for GISANS is 0.31 ° with 4.5 Å, and this value would approximately change to ~0.42 ° with 6 Å according to the calculations. Two GISANS maps were collected with different wavelengths for 5 minutes show in Fig. 7.8(b) and (c).

The slit size was fixed 2 mm x 8 mm during both measurements. The first and second Bragg peak along Yoneda line locate at Qy = 0.02 $Å^{-1}$ and 0.04 $Å^{-1}$, respectively. Clearly, GISANS data taken with a wavelength of 6 Å has more clear Bragg peaks, due to the larger of scattering angle. Thus, the rest of the measurements were done with the wavelength of 6 Å.

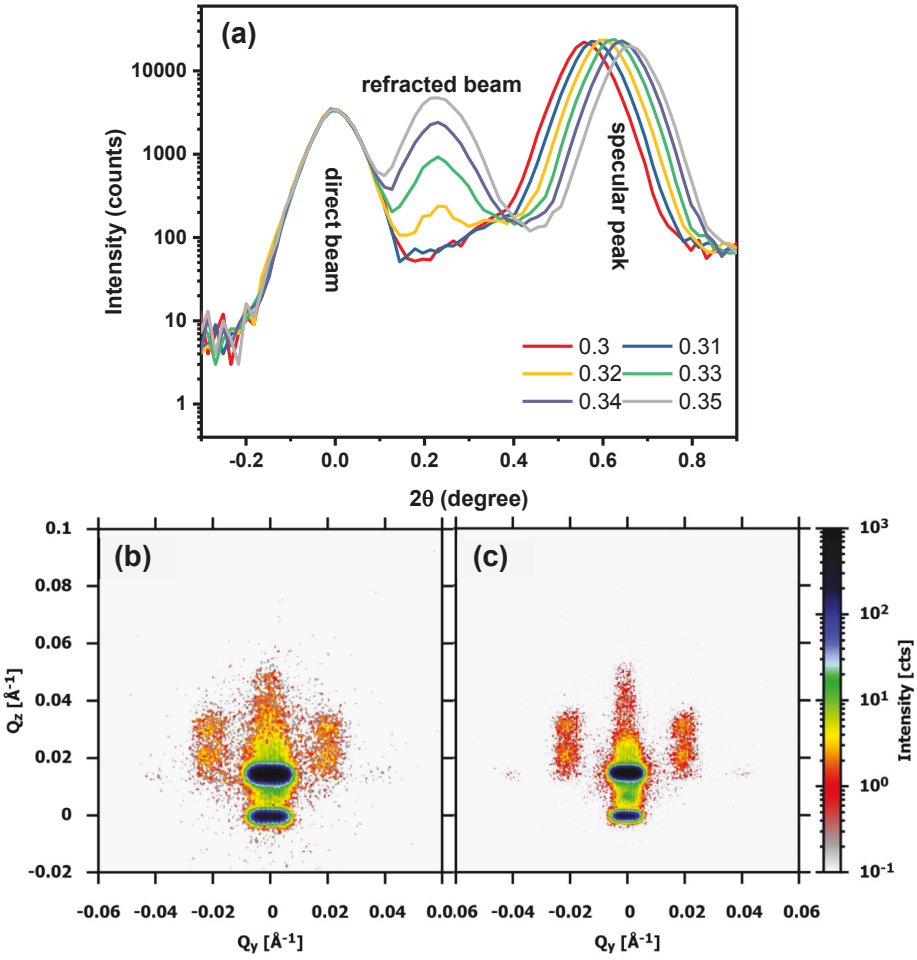

Fig. 7. 8 (a) The line cuts along specular line of GISANS at various incident angles from 0.3 to 0.35 °. The GISANS measurements performed at (b) 0.31 ° with λ = 4.5 Å and (c) 0.41 ° with λ = 6 Å. All data was taken at 300 K.

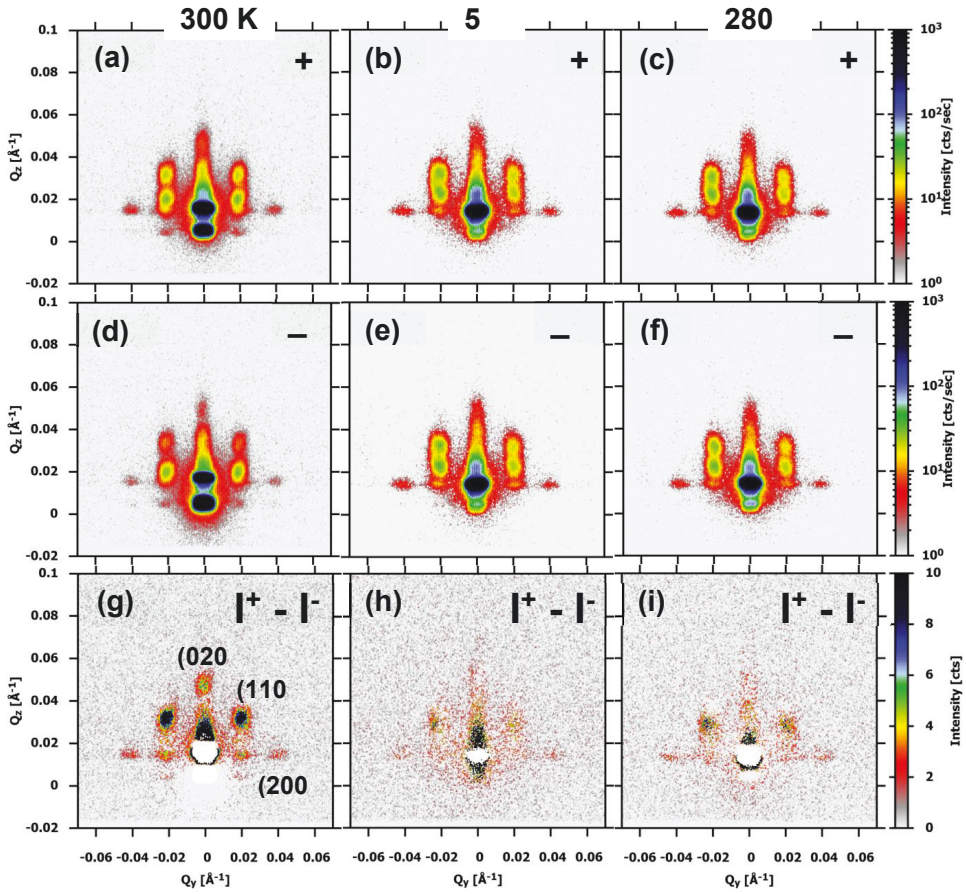

Fig. 7. 9 The PGISANS data at 300 K (a, d and g), 5 K (b, e and h) and 280 K (c, f and i) in the field of 0.5 T. The difference (I^+ - I^-) between scattering intensities of spin up (+) and spin down (-) is on the liner scale and the rest is on the log scale.

The PGISANS measurements were used to investigate the interactions between 3D-assembly of the magnetic nanoparticles. The PGISANS was measured at 5 K, 280 K, and 300 K using λ = 6 Å for each field with spin-up (I+) and spin-down (I-) channel for 3 hours. For two neutron polarizations, the neutron spin was parallel (+) or antiparallel (−) to the direction of the external field. No polarization analysis of the scattered beam was applied. In order to improve the resolution, the slit size was set to 0.6 mm x 8 mm. The PGISANS at 300 K was performed first in air with the applied magnetic field of 0.5 T which is limited by the instrument (see Fig. 7.9 (a), (d) and (g)). The incident angle was set to 0.42 ◦ which was close to the incident angle limit. The difference (I^+ - I^-) shows in Fig. 7.9(g) and the first and second peak along Yoneda line locate at Qy = 0.02 $Å^{-1}$ and

0.04 $Å^{-1}$, respectively. This result may indicate that there is an ordered magnetic structure, which is superimposed onto the framework structure. At this incident angle, the transmitted beam is still intense and interfered with the scattering intensity, we reduced the incident angle down to 0.4 ° for the remaining PGISANS measurements.

Table 7. 3 The integrated intensity of (110) peak at different temperature.

(110)	Incident angle	I+	I-	I+ - I-
300 K	0.42 °	8483 ± 74	4431 ± 75	4052 ± 105
5 K	0.4 °	9920 ± 68	9679 ± 71	241 ± 98
280 K	0.4 °	9410 ± 66	8986 ± 74	426 ± 99

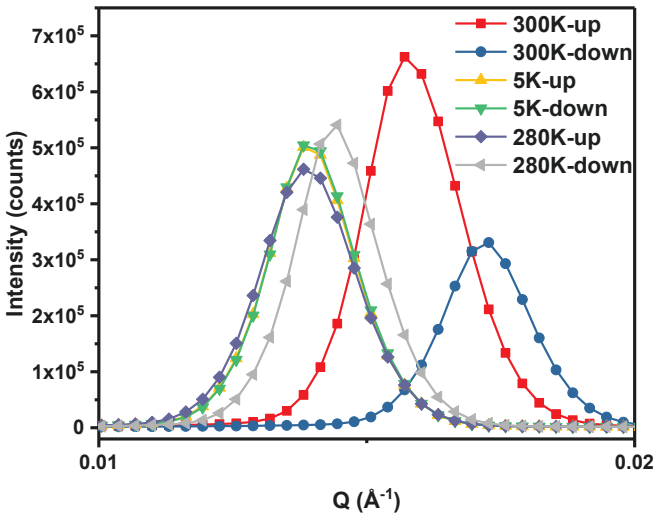

Fig. 7. 10 The specular speaks of GISANS at different temperature with 0.5 T.

The sample was cooled down to 5 K in zero field, after that the field of 0.5 T was applied and PGISANS measurements were taken. Then the sample temperature was increased to 280 K in zero field and the same magnetic field of 0.5 T was applied again. For the measurements at 5 and 280 K, the sample was inserted into the liquid He-cryostat with a high vacuum (< 1 mbar). Those data are presented in Fig. 7.9. The differences signals (I^+ - I^-) for 5 K and 280 K are shown in Fig. 7.9(h) and (i). The signal (I^+ - I^-) is proportional to the net mean magnetization along external magnetic field of the magnetic nanoparticles ensemble. As the temperature increasing, the difference of

Bragg peaks becomes more visible. But the difference of intensity doesn't change significantly. The integrated intensity of (110) peak at different temperature are listed in Table 7.3. The error bar was estimated by using the scattering intensity at the edge of detector. Because of low concentration of nanoparticles, magnetic SLD makes a very small contribution and the difference between spin up and spin down intensity of (110) peak at 300 K is not reasonable. The specular peak positions of those three measurements are shown in Fig. 7.10. By comparing the specular peak position of different spin state, we think the sample position was changed during the measurement at 280 and 300 K. And the specular peaks remain at the same position of the 5 K. As the signal-to-error ratio is not too high at 5 K, we don't estimate the magnetic SLD from the PGISANS data.

From Table 7.2, the nuclear SLD of the nondeuterated polymer matrix blocks (4VP and PDP) is comparable to the magnetic SLD of the nanoparticles (mSLD = 0.9e-06 $Å^{-2}$). Both of them are far away from the nuclear SLDs of the nanoparticles and deuterated PS cylinders. Because the volume fraction of deuterated PS cylinders is round 17 times of nanoparticles, GISANS signal is dominate by deuterated PS cylinders. There are two ways to increase magnetic scattering signals: doping more nanoparticles and using saturation field. The designed nanoparticles concentration is 8 wt%. And the real concentration is lower than this number based on the results in chapter 6. The GISANS data of nanocomposite film with 15 wt% is in the appendix E. High concentration of nanoparticles disorders the structure and less Bragg peaks show in the GISANS data. At this beamtime, the highest could be reached was 0.5 T.

7.3.3.2 PNR @ 5 K

Motivated by the first PGISANS measurements, we used PNR measurements to clarify the magnetic structure of our nanocomposite films. The PNR measurements will provide the depth-resolved SLD profiles of the nanocomposite film. The neutron reflectivity measurements were performed at room temperature with λ = 6 Å, for 30 seconds per point and with much larger slit size, as compared to GISANS: 1 mm x 42 mm. Both nondeuterated and deuterated nanocomposite films were used to do the test neutron reflectivity measurements (Fig. 7. 11(a) and (b)). The 2D map of the deuterated sample shows much sharper Bragg sheets, Bragg peaks and Yoneda wings. The background is also reduced as compared to nondeuterated sample, thus all of those different prominent features displayed in the Fig. 7. 11(b) indicates that the most of the scattered neutrons are coming from the deuterated PS components. In order to estimate the contribution of the substrate to the observed reflectivity, we plot the neutron reflectivity of the substrate together with nondeuterated and deuterated nanocomposite films as a function of the scattering vector Q (7.11(c)). The reflectivity of the deuterated sample shows a broad peak at around 0.038 $Å^{-1}$, while in the nondeuterated this peak is less

intense and shifted to a higher value of Q = 0.041 Å^{-1}. This observation is consisted with the lattice parameters of two samples obtained with GISAXS measurements.

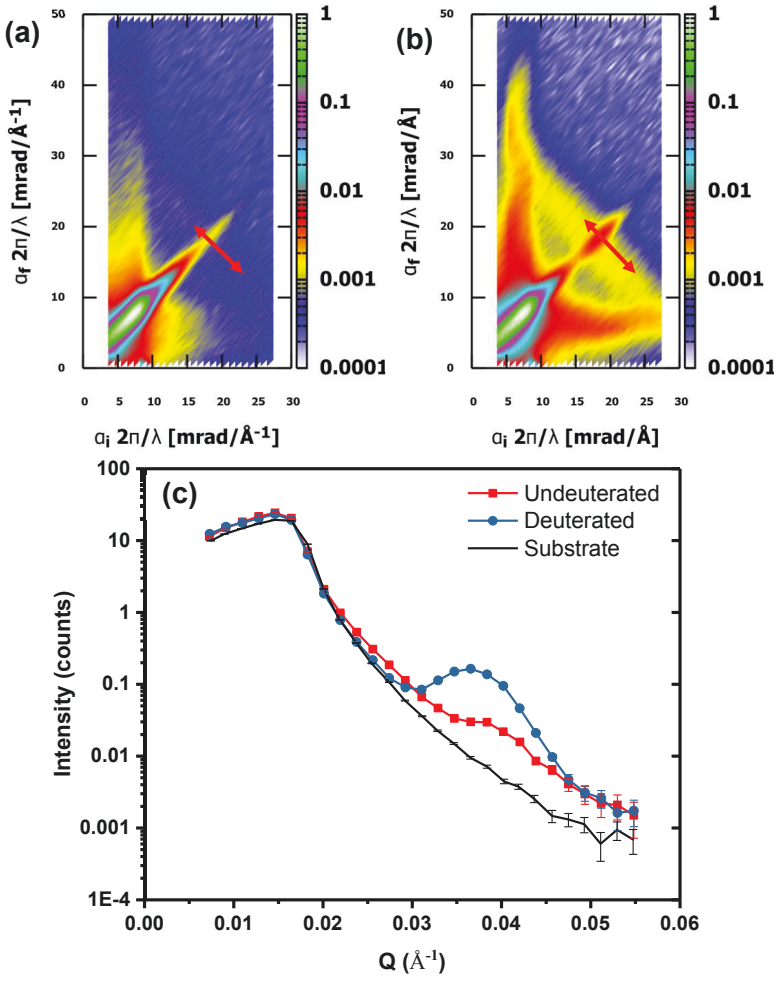

Fig. 7. 11 The off-specular Neutron reflectivity map of (a) H8 and (b) D8, (c) the specular reflectivity curves. Double arrow pointed out the Bragg sheet.

In order to avoid background due to incoherent scattering from hydrogen, deuterated block copolymer is used for further PNR measurements. The PNR data were collected at 5 K in the saturated field (1.1 T) and at coercive field (5 mT) with λ = 6 Å. The

polarization analysis of the scattered beam was applied. During the measurements, we checked the polarization before and after measurements at different fields. Before measurement, the polarization was 98 ± 0.2 % and after the measurement at saturated field, the value changed to 97.9 ± 0.2 %. The polarization remains the same after the measurements at coercive field. The background corrected off-specular reflectivity data (350 s for each step) measured at two different fields are presented in Fig. 7.12. The features in non-spin-flip channels (++, --) are similar at two different fields. When coercive field is applied, there are clear signals in the spin-flip channels (+-, -+) along Yoneda wings. As the field increasing, magnetic moments of nanoparticles are aligned along the field direction and hence there is less signal strength in the spin-flip channel at the saturation field. The difference of spin-flip channels between two different fields give the solid evidence the magnetic scattering exists.

The specular reflectivity curves are shown in Fig. 7.13(a) and (b). The spin-flip channels signals are sensitive to the in-plane magnetization component perpendicular to the magnetic field. The spin-flip curves (ud and du) replicate the shape of non-spin-flip channels (dd and uu) and two orders of magnitude lower than the intensity in the non-spin-flip channels (see Fig. 7.13(a) and (b)). This means that we only measured the neutron spin leakage, which is due to the beam polarization of ~98 %. But the intensity of the regime before critical edge of spin-flip curves (ud and du) at 5 mT is higher than at 1.1 T which is also the clue of some spin flipped at 5 mT.

In order to separate the nuclear and magnetic components and to amplify the magnetic scattering, the so-called spin asymmetry ($\mathrm{SA} = (I^{uu} - I^{dd})/(I^{uu} + I^{dd})$) is used in the analysis of the PNR data. The spin asymmetry is very sensitive to small magnetic signals. Fig. 7.14 shows the SA at 1.1 T and 5 mT. We observe no peaks in SA curve at both fields, i.e. the value of SA = 0 corresponds to a zero net magnetic moment in the film. The interpretation of this surprising result will be will discuss in the end of this chapter (In section 7.3.3.3).

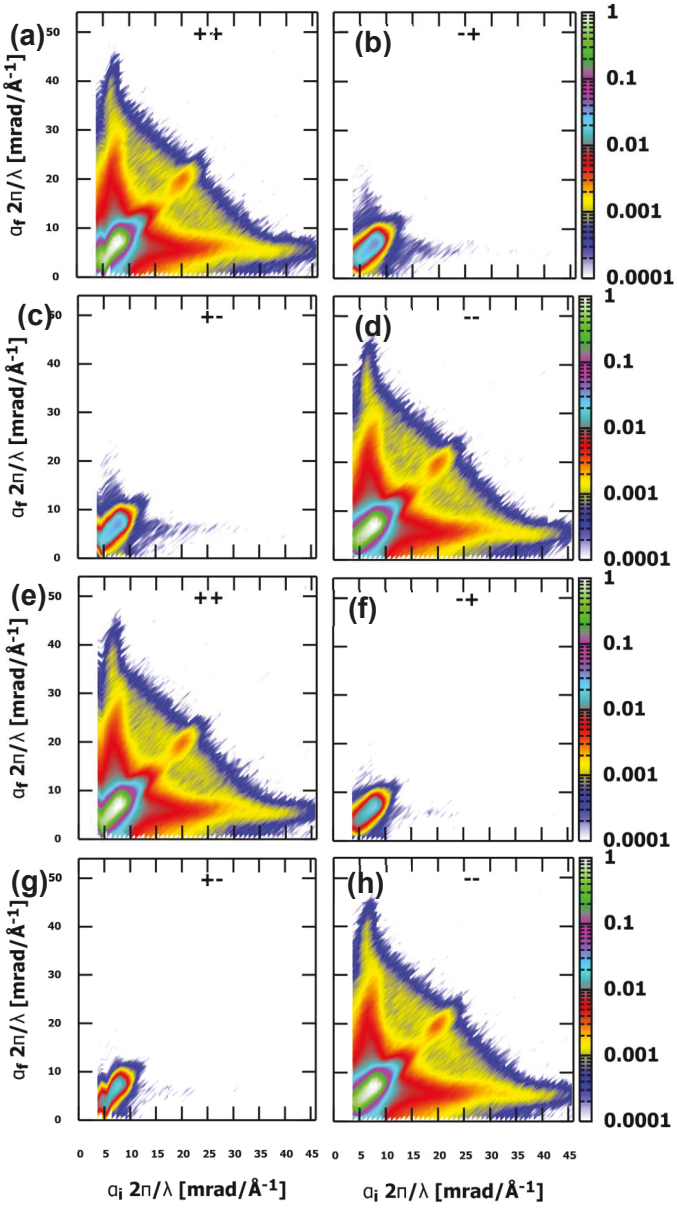

Fig. 7. 12 The off-specular map measurements taken at 5 K and at 1.1 T (a, b, c and d) and 5 mT (e, f, g and h).

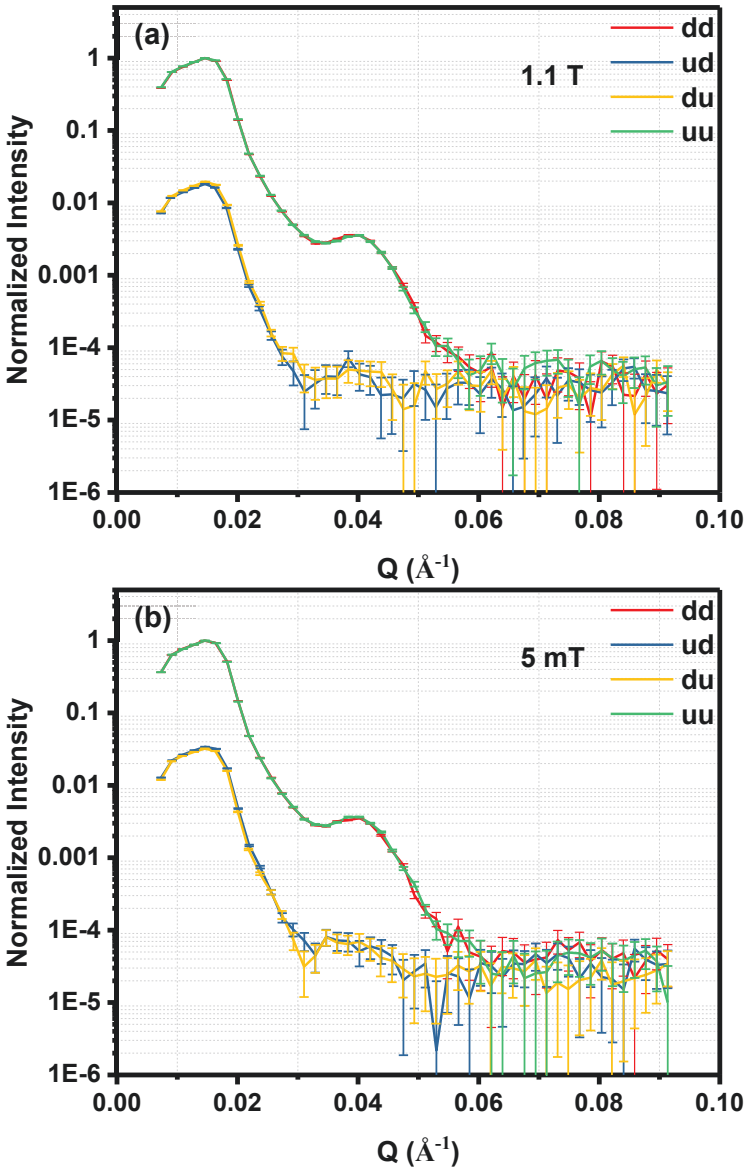

Fig. 7. 13 The PNR measured at 5 K with the magnetic field of (a) 1.1 T and (b) 5 mT.

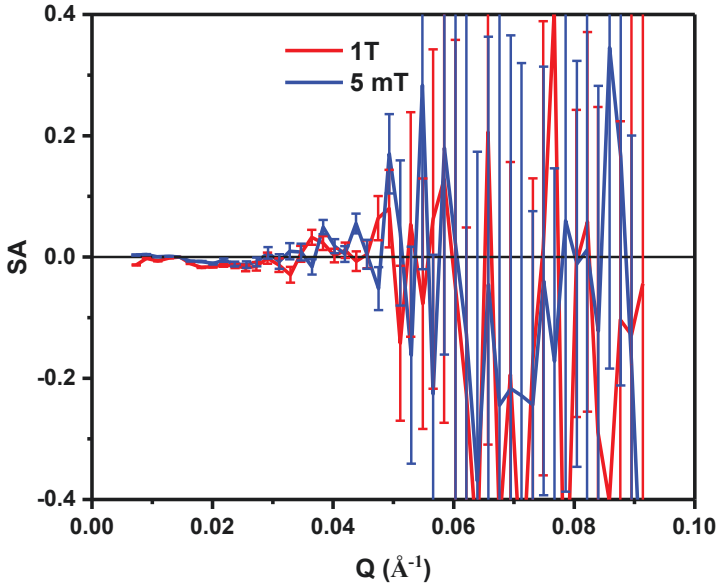

Fig. 7. 14 The spin asymmetry plot obtained from the PNR data at 5 K.

7.3.3.3 PNR @ 300 K

The measurements were planned to be performed at 5 K with λ = 6 Å. The sample quality was quickly checked (15 s for each step) by the off-specular reflectivity map measurements. The map (Fig. 7.15(a)) at room temperature is similar to our previous results depicted in Fig. 7.11(b), with a clear Bragg peak. However, after reaching 5 K, the same condition measurement result reveals no indications of the Bragg peak observed at room temperature.

After warming sample back to the room temperature, the quick measurement in air revealed no Bragg peak as well (Fig. 7.15(c)). One of the possible explanations of such a peculiar effect is the structure of nanocomposite film is changed under high vacuum, used to reach 5 K in the cryostat. If sample is disintegrated in vacuum, it might explain why the difference in the PGIANS data is becoming weaker at 5 K. It will also explain why no obvious SA variation is observed at 5 K.

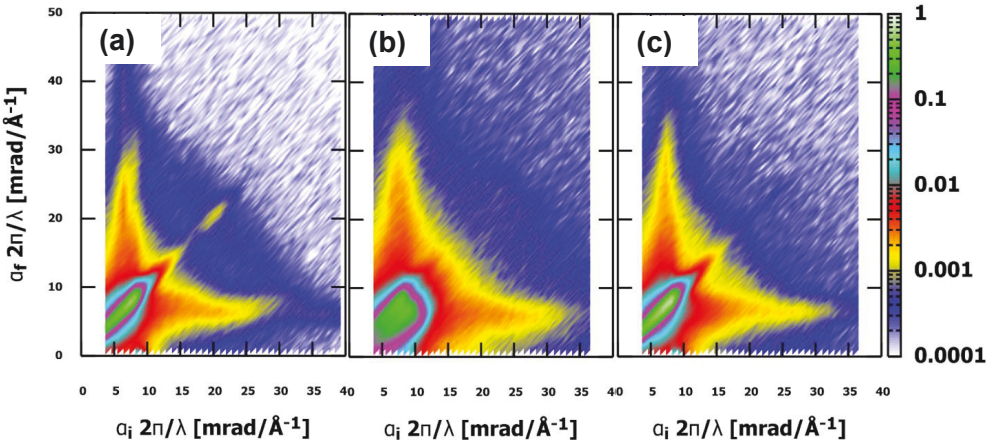

Fig. 7. 15 The off-specular map collected at (a) room temperature in air, (b) cooling down to 5 K in vacuum and (c) warming to room temperature in air.

In order to avoid any interaction of the sample with the vacuum, we modified the experimental conditions for next round of the PNR measurements. Freshly synthesized sample was first measured at the room temperature. We know from the DC magnetization results that the nanocomposite film behaves as a superparamagnet at this temperature. Hence, two different fields of 1.1 T and 5 mT have been chosen to perform the PNR. The first one corresponds to the saturation field of our sample at 300 K, while the second one is a minimum guide field required to conserve the polarization of the neutron beam. Before and after measurement, the polarization remained the same (98 ± 0.2 %).

The off-specular reflectivity data (330 s for each step) is shown in Fig. 7.16. All off-specular maps are background corrected. The features in non-spin-flip channel (++, --) and spin-flip channels (+-, -+) are similar at two different fields. There is no clear signal in spin-flip channels. The strong Bragg sheet of intensity perpendicular to the specular line at the position of the Bragg peak indicates that there are correlations in the lateral direction of the sample. By using the positions of the Yoneda wings, we estimate the critical angle of nanocomposite film to be 0.34 ± 0.01 ° at λ = 6 Å.

The PNR data measured at 1.1 T and 5 mT are displayed in Fig. 7.17. The small splitting of Bragg peaks between uu and dd channels is obvious when the 1.1 T magnetic field is applied.

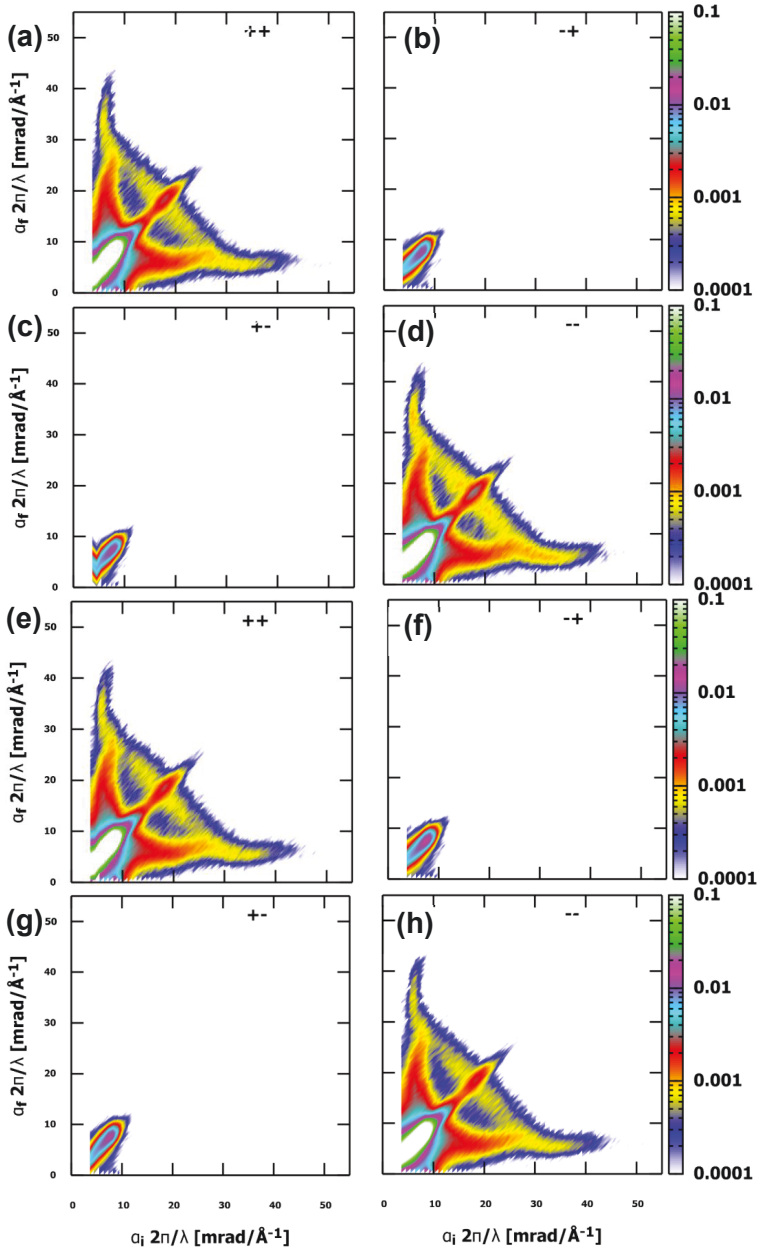

Fig. 7. 16 The off-specular map at 300 K with the field of 1.1T (a, b, c, d) and 5 mT (e, f, g, h).

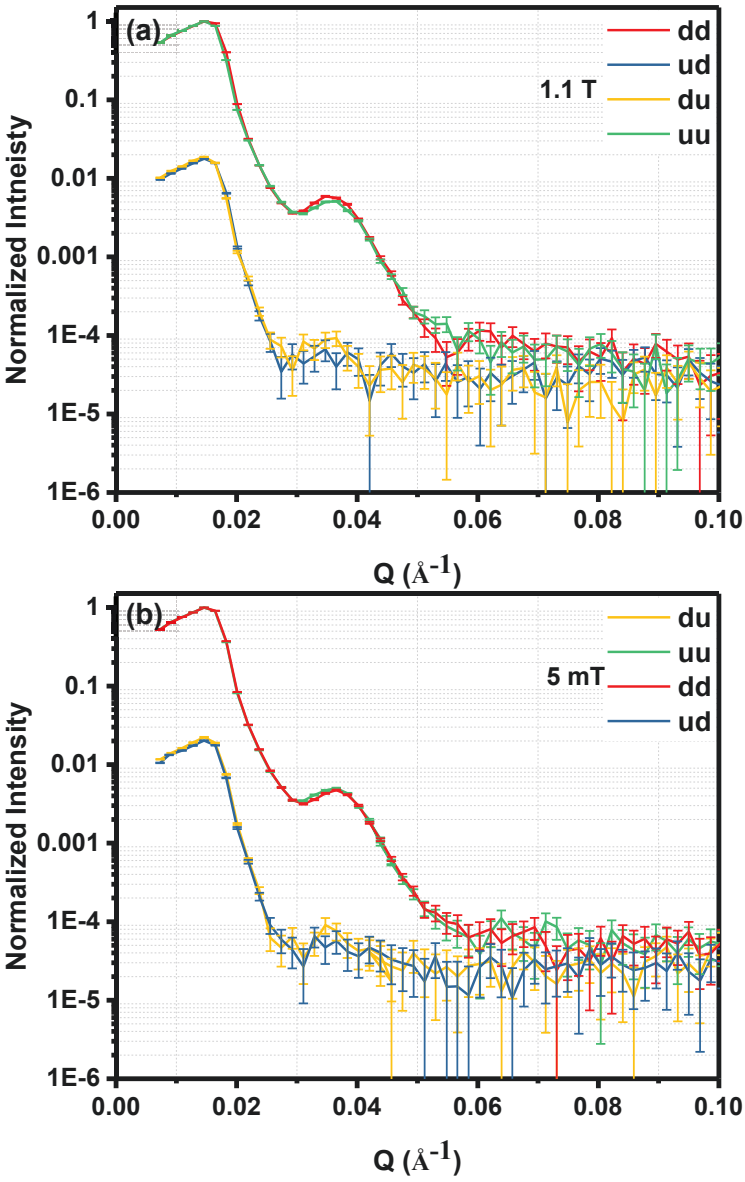

Fig. 7. 17 The PNR measured at 300 K with the field of (a) 1.1 T and (b) 5 mT.

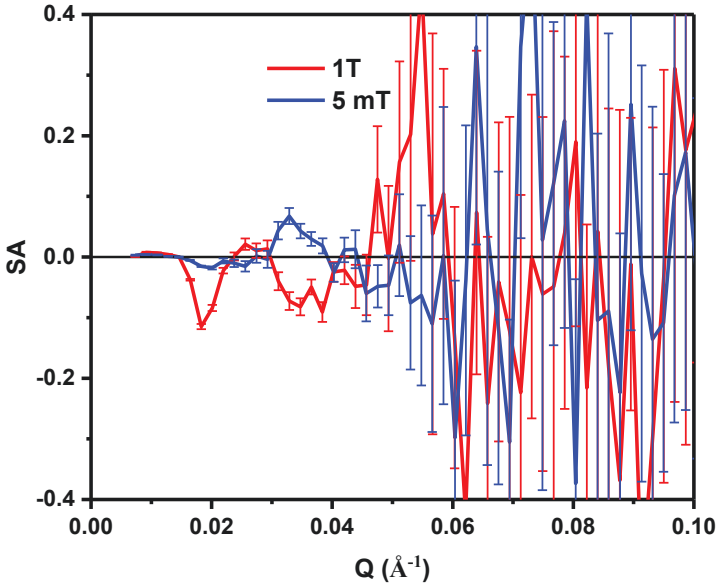

Fig. 7. 18 The SA plot at 300 K with two different fields.

The spin asymmetry plot (Fig. 7.18) clearly indicates the small in-plane magnetic contribution in our sample. The amplitude and period of the oscillation in SA curve are related to the magnetization contrast across the interfaces between magnetic/non-magnetic layers and the total thickness of the film, respectively. The field dependent SA peak (closed to 0.02 $Å^{-1}$, around the critical edge) indicate the magnetic scattering exist in this nanocomposite film. The maximum amplitude SA = -11 % has been observed around the critical edge at 1.1 T.

Based on the GISAXS and GISANS data, we know the dPS cylinders will form base-centered orthorhombic lattice and nanoparticles will fill the gaps. In order to fit the PNR data, we need to treat the film as multilayer structure even though there is no real layer in the film. There are two possible ways to choose the repetition unit shown in Fig. 7.19. The repetition unit consists of two sub-layers. The first model treats the dPS and nanoparticles as sub-layer 1 and the rest as sub-layer 2. The second one is divided in sub-layer 1 with nanoparticles and sub-layer 2 without nanoparticles. The ideal SLD and mSLD profiles are in same period. SLD is dominated by dPS cylinders and mSLD is followed the distribution of nanoparticles. The first model is easy to describe the nuclear SLD profile but not proper for the magnetic SLD profile. And the second model works in

the opposite. We know that the dPS cylinder has the big contrast from Table 7.2 and low concentration of nanoparticles was doping in the film. So we choose first model for fitting the data at 1.1 T.

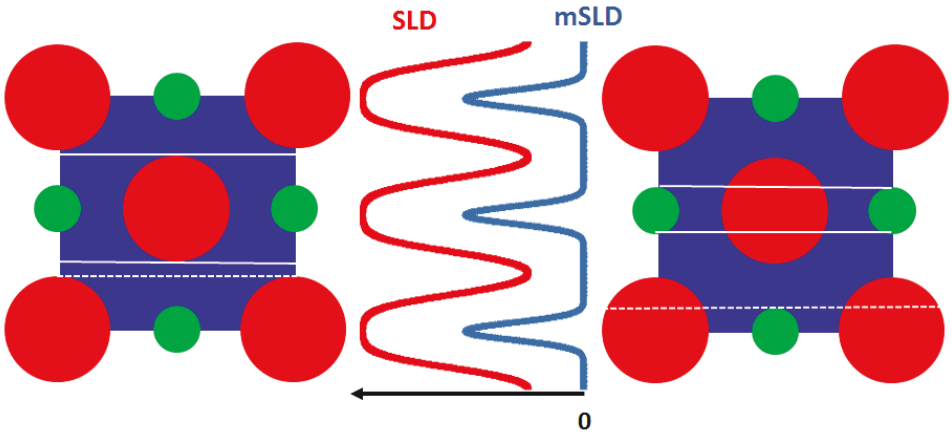

Fig. 7. 19 Two possible ways to slice sub-layers. In this schematic, the PS cylinder is in red and the P4VP(PDP)1.7 matrix is in blue and nanoparticle is in green.

By using this sample model, we start to fit the parameters of thickness, roughness, and SLD by the software package of GenX [15]. In order to simply the fitting process, the thickness of sub-layer 1 is set in range of 10 to 13 nm which is limited by the diameter of dPS and the SLD of sub-layer 2 is fixed. As the substrate has patterns on the surface, the patterned substrate is defined by two parts, solid substrate with fixed SLD and patterned layer (thickness, roughness and SLD). Because of the low magnetic nanoparticles concentrations, the sub-layer 1 is defined as uniform deuterated polymer with small magnetic SLD. As shown in the Fig. 7.19, the ideal SLD profile will change smoothly at the interface. In order to create the SLD gradient, the roughness of each sub-layer has been considered. The SLD will change sharply at the interface when there is no roughness in the sample model shown in Fig. 7.20. An oscillated SLD profile is produced by increasing the sub-layer roughness from 1 nm to 3 nm.

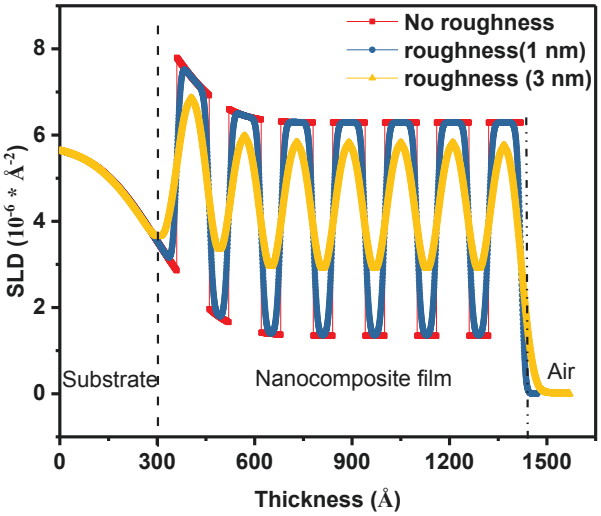

Fig. 7. 20 The ideal SLD profile changed with sub-layer roughness.

Table 7. 4 Fitted parameters.

	Sub-layer	Thickness (nm)	Roughness (nm)
Air			
Fifth stack	1	12.5 ± 0.3	5.9 ± 0.2
Fourth stack Repetition:2	2	7.4 ± 0.4	5.9 ± 0.2
	1	11.5 ± 0.5	4.9 ± 0.2
Third stack Repetition:2	2	6.5 ± 0.6	4.1 ± 0.2
	1	10.3 ± 0.2	4.5 ± 0.2
Second stack Repetition:2	2	5.6 ± 0.3	3.6 ± 0.2
	1	10.7 ± 0.5	4.8 ± 0.2
First stack	2	2.3 ± 0.6	1.8 ± 0.2
Sapphire pattern		29 ± 0.2	11.2 ± 0.2

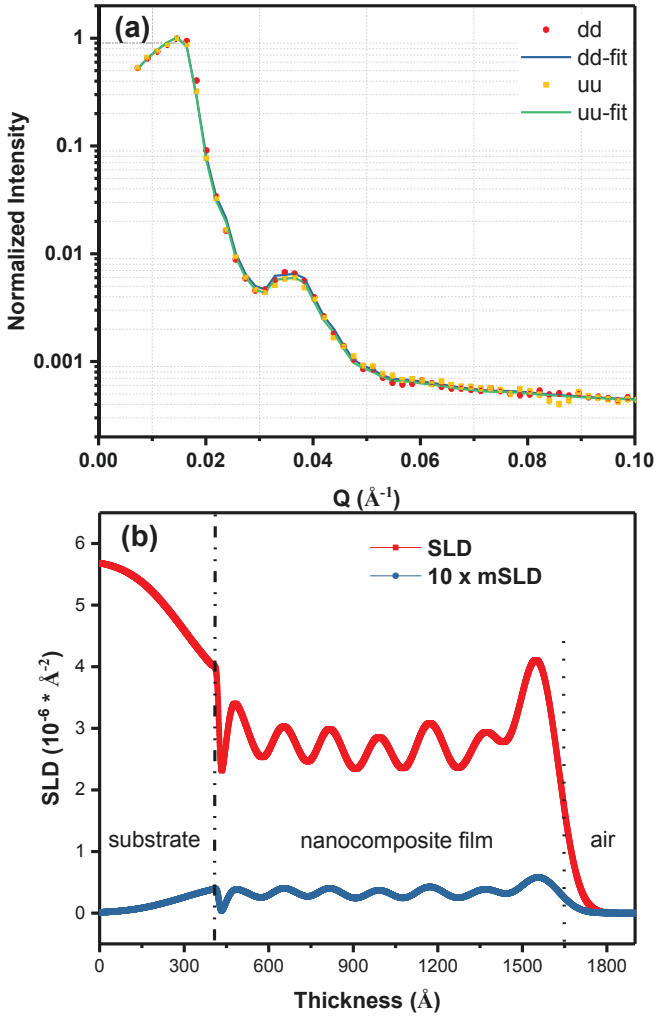

Fig. 7. 21 (a) The best fits for PNR data at 1.1 T and (b) the SLD and magnetic SLD profile obtained from the fitting.

The best fits for PNR data and the corresponding SLD and magnetic SLD are shown in Fig. 7.21. The fitted parameters are listed in the Table 7.4. The average thickness of the unit layer is 17 ± 1.5 nm which is very close to the b/2 (~ 16 nm). As shown in Fig. 7.21(b), the SLD and magnetic SLD have same period and Sine wave shape. During

the fitting, mSLD of all sub-layer 1 is in same value. The 10 times of magnetic SLD is very small in Fig. 7.21(b) compared with SLD. Because of the patterned substrate and big interfacial roughness, only one peak has been observed and the reflectivity intensity decrease very quick. Based on the PNR results, we conform that nanoparticles have period structure normal to the surface.

7.4 Summary

In the present chapter, the morphology and structure of deuterated superparamagnetic nanoparticles/dPS-b-P4VP(PDP)1.7 hybrid films were characterized with AFM and GISAXS. The results indicate that the deuterated hybrid film has similar structure as nondeuterated hybrid films. The 8 wt % of magnetic nanoparticles embedded of nanocomposite films were used to illustrate the capabilities of the polarized neutron scattering. Polarized neutron scattering method has been employed to investigate the deuterated hybrid films. The block copolymer provides periodically ordered nanostructures after solvent annealing and serve as a template to guide the self-assembly of the magnetic nanoparticles. Combined the structural information obtained from GISAXS and GISANS results, the superparamagnetic nanoparticles located in the gap of dPS cylinders and may form the magnetic structure with the same periodicity as the framework, when the external magnetic field is applied. The field dependent spin asymmetry obtained from PNR is the clear evidence the magnetic scattering length density changes along the depth of the film. Moreover, the structure of the nanocomposite film is found to be affected by the vacuum, and careful consideration of the experimental setup for low temperature measurements of such films in cryostat has to be given.

Despite this, the GISANS and PNR have two big advantages for studying our samples: a non-destructive structural probe (that is, no radiation damage occurs) that provided the magnetic structure information on the nanometer scale by averaging over macroscopic area. The GISANS and PNR are successfully applied to the investigation of the low concentration of magnetic nanoparticles embedded of nanocomposite films. The highly periodic superparamagnetic magnetic nanoparticles doped in the block copolymer films are promising material for a large number of applications in the fields of magnetic storage devices and magnetic sensors.

Chapter 8 Summary and Outlook

The main focus of this thesis is on synthesis and advanced characterization of self-assembly of magnetic nanoparticles. The patterned sapphire substrate had been used for the fabrication of various highly-ordered nanostructure systems: 2D nanoparticles arrays on the surface of the substrate and nanocomposites film embedded with 3D arrays of nanoparticles. Real space (TEM, SEM and AFM) and reciprocal space (SAXS and GISAXS) techniques have been employed to provide overall information about the morphology and structure of our self- assembled systems. The magnetic structure of self-assembled systems has been studied with PGISANS and PNR methods. Moreover, the macroscopic magnetization of our samples is investigated using Dynacool magnetometer.

The work started with characterization of free iron oxide nanoparticles of very different size 5 and 28 nm (ON5 and NP28) which were used as building blocks for the self-assembly. It is important to characterize as-synthesized nanoparticles in order to monitor how structural or magnetic properties are changed when particles are self-assembled on a substrate. The 28 nm diameter nanoparticles (NP28) were obtained from the collaborator and 5 nm nanoparticles (ON5) were purchased from Ocean NanoTech. The size and shape of nanoparticles was characterized in details by TEM and SAXS measurements. The measurements confirm the spherical shape of both samples and following dimensions are obtained: NP28 (30.6 nm, polydispersity: 0.07) and ON5 (5.6 nm, polydispersity: 0.13). The magnetization measurements of these samples were performed with Dynacool magnetometer and reveal that ON5 nanoparticles are in superparamagnetic state at room temperature, while NP28 nanoparticles show two transition temperatures and the blocking temperature above room temperature.

In order to guide the NP28 nanoparticles self-assembly, the synthesis of the patterned sapphire substrate was optimized. The M-plane (10-10) sapphire substrate was annealed at elevated temperatures (1300, 1400, 1450 or 1500 °C) for 24 hours to form saw-tooth patterns over the entire surface. The AFM and GISAXS measurements had been employed to characterize the morphology and structure of the substrates. By comparing the amplitude of patterned substrates obtained at different annealing temperatures, the patterned substrate (amplitude: 30.8, width: 146 nm) annealed at 1500 °C (sap1500) is selected for the template guiding of the NP28 nanoparticles self-assembly. The NP28 nanoparticles were spread on the patterned substrate by a spin coating method. The quasi-periodic saw-tooth structures produce the trap effect for nanoparticles and it is balanced by the centrifugal force during the spin coating.

Moreover, this method allows to align and to homogeneously distribute nanoparticles into a 2D nanostructure with the facet geometry. The structural information of 2D self-assembly samples were obtained by SEM and GISAXS measurements. The correlation length will decrease by adding more nanoparticles suspension during the sample preparation. There is no clear evidence of the hexagonal ordering in the samples with a high suspension volume. The DWBA simulations reveal that the saw-tooth topography does affect the GISAXS pattern when the incident beam is perpendicular to the ridge of the patterned substrate. The DWBA fitting results demonstrate that the 2D lattice with 1D lattice interference function is a reasonably model to describe the resulting sample morphology of our sample.

The second system is nanocomposite films composed of ON5 nanoparticles (8 wt %) and block copolymer. The spherical ON5 nanoparticles are selected because they are small enough to be embedded in the copolymer matrix. The same sap1500 substrate serves as a template for guiding the nanocomposite film self-assembly. The spatial arrangements of the nanoparticles within the polymer matrix were fabricated via spin coating followed by a post-treatment (solvent vapor annealing) to establish a microphase separation of nanocomposite films. The thickness of the films depends on the preparation conditions, spin speed and volume of supramolecular solution. With the help of SEM, the proper preparation parameters (5 µl, 50 rps) were selected to fabricate the film with thickness below 200 nm by spin coating the supramolecular solution on the sap1500 substrate. To optimize the sample quality, the solvent vapor annealing parameters, including solvent volume and the annealed time, were explored carefully. The morphology and orientation of the nanocomposite films had been checked by AFM and GISAXS measurements. Different morphology was obtained by varying the solvent volume and the annealed time. The azimuthal angle dependent GISAXS were employed to obtain the orientation factor (S) and correlation length which quantified the nanocomposite film quality. Meanwhile, slow drying process was also very important parameter in our synthesis. A highly-ordered alignment of the nanoparticles in the block copolymer matrix can be achieved via solvent vapor annealing in the jar with 120 µl chloroform for 6 minutes followed by freely evaporating. The optimized film has a high orientation factor of 0.94. Furthermore, a combination of Bragg's and Snell's laws is applied to base-centered orthorhombic lattice for a qualitative analysis of the GISAXS data (critical angle: 0.14 ± 0.001 °, lattice constants: a = 28.2 and b = 29.4 nm). The GISAXS data was simulated based on the DWBA theory for a quantitative understanding, and the correlation length in-plane (500 nm) and out-of-plane (90 nm) are obtained from the simulation. The analysis of the GISAXS data provides valuable information for the rational and controlled design of functional nanomaterials. Notably, whether embedded or not, it does not change the magnetic properties which is quite interesting for the applications.

The third system we studied in this thesis is nanocomposite films consisting of ON5 nanoparticles (8 wt %) and deuterated block copolymer. By carefully choosing the deuterated block copolymer as close as the nondeuterated block copolymer in chapter 6, the deuterated nanocomposite film has similar structure as nondeuterated nanocomposite film. A morphology of highly ordered, well oriented, the base-centered orthorhombic lattice (a = 32 and b = 31.5 nm) nanocomposite film was achieved by using the preparation parameters described in chapter 6. The deuterated nanocomposite films embedded with 8 wt % of magnetic nanoparticles are good candidates to illustrate the power of the polarized neutron scattering for revealing their magnetic structures. The GISANS and PNR measurements had been carried out to provide the information about magnetic structures that were combined with the structural information obtained from the GISAXS measurements. Furthermore, the GISANS and PNR methods have two big advantages for investigating the nanocomposite films: they are non-destructive structural probe (that is, no radiation damage occurs during the measurements) and second, they provide the magnetic structure information on the nanometer scale by averaging over macroscopic area. The GISAXS and GISANS reveals that the superparamagnetic nanoparticles locate in the gap of dPS domains and may form the magnetic structure with the same periodicity as the framework, when the external magnetic field is applied. The PNR data provides the field dependent spin asymmetry result which is the evidence of the variation of magnetic scattering length density in depth. Such unique structure is attractive for applications requiring constant periodicity of a magnetic nanostructure. The GISANS and PNR measurements are successfully applied to the investigation of the low concentration of magnetic nanoparticles embedded of nanocomposite films. Moreover, the structure of the nanocomposite film is found to be affected by the vacuum.

To conclude, the following relevant programs were achieved in this thesis:

1. The thermally reconstructed M-plane sapphire substrate is effective to guide the self-assembly of nanoparticles.

2. Nanocomposite film with hierarchically structured 3D nanoparticles assemblies with long-range order in unidirectional block copolymer matrix is achieved via patterned substrate.

3. The GISANS and PNR techniques are successfully applied to the investigation of the low concentration of magnetic nanoparticles embedded in nanocomposite films.

As an outlook, several unsolved issues would be interesting to resolve. For instance, the nanocomposite film is sensitive to the vacuum and might be damaged particularly at low temperatures, when high vacuum is required for cooling. This issue limits use of scattering methods at low temperatures. The in-situ GISAXS measurements on the

solvent vapor annealing and the drying process could be useful to understand the self-assembly of the nanocomposite film. Of course, how to build more complex magnetic structures by using the polymer matrix of various properties is another interesting question. Yet, our recipes and methods used to study of nanocomposite film doping with superparamagnetic nanoparticles provide a solid base for manipulating and tracking the changes in the magnetic structure of even more complex self-assemblies.

Appendix A List of abbreviations

2D Two dimensional

3D Three dimensional

AFM Atomic Force Microscopy

SAXS Small angle x-ray scattering

SANS Small angle neutron scattering

GISAXS Grazing incidence small angle x-ray scattering

GISANS Grazing incidence small angle neutron scattering

PGISANS Polarized Grazing incidence small angle neutron scattering

PNR Polarized neutron reflectivity

DWBA Distorted-wave Born Approximation

BA Born Approximation

AAO Anodic aluminum oxide

DBP Di-block copolymers

SAS Small angle scattering

SLD Scattering length density

mSLD Magnetic scattering length density

SAXS Small Angle X-ray Scattering

SEM Scanning Electron Microscopy

TEM Transmission Electron Microscopy

VSM Vibrating Sample Magnetometer

ZFC Zero Field Cooling

FC Field Cooling

Appendix B Simulation script of GISAXS for 2D self-assembly nanoparticles

```python
import numpy
import bornagain as ba
from bornagain import deg, angstrom, nm, nm2, kvector_t


def get_sample():
    # Defining Materials
    material_1 = ba.HomogeneousMaterial("Air", 0.0, 0.0)
    material_2 = ba.HomogeneousMaterial("Sap", 9.55662e-06, 8.4396e-08)
    material_3 = ba.HomogeneousMaterial("Particle_Fe3O4", 1.18426087e-05, 8.48039519e-07)
    material_4 = ba.HomogeneousMaterial("sapphire_sub", 9.55662e-06, 8.4396e-08)

    # Defining Layers
    layer_1 = ba.Layer(material_1)
    layer_2 = ba.Layer(material_4)

    # Defining Form Factors
    formFactor_1 = ba.FormFactorRipple2(1000.0*nm, 146.0*nm, 30.8*nm, 24.5*nm)
    formFactor_2 = ba.FormFactorRipple2(1000.0*nm, 146.0*nm, 30.8*nm, 24.5*nm)
    formFactor_3 = ba.FormFactorFullSphere(15.1*nm)

    # Defining Particles
    particle_1 = ba.Particle(material_2, formFactor_1)
    particle_1_rotation = ba.RotationZ(-90.0*deg)
    particle_1.setRotation(particle_1_rotation)
    particle_2 = ba.Particle(material_2, formFactor_2)
    particle_2_rotation = ba.RotationZ(-90.0*deg)
    particle_2.setRotation(particle_2_rotation)
    particle_2_position = kvector_t(146.0*nm, 0.0*nm, 0.0*nm)
    particle_2.setPosition(particle_2_position)
    particle_3 = ba.Particle(material_3, formFactor_3)
    particle_3_position = kvector_t(73.0*nm, 0.0*nm, 0.0*nm)
    particle_3.setPosition(particle_3_position)

    # Defining Interference Functions
    interference_1 = ba.InterferenceFunction1DLattice(34.1*nm, 90.0*deg)
    interference_1_pdf  = ba.FTDecayFunction1DCauchy(1000.0)
    interference_1.setDecayFunction(interference_1_pdf)

    # Defining Particle Layouts and adding Particles
    layout_1 = ba.ParticleLayout()
    layout_1.addParticle(particle_1, 1.0)
    layout_1.addParticle(particle_2, 1.0)
    layout_1.addParticle(particle_3, 1.0)
    layout_1.setInterferenceFunction(interference_1)
    layout_1.setWeight(1)
    layout_1.setTotalParticleSurfaceDensity(0.01)

    # Adding layouts to layers
    layer_1.addLayout(layout_1)

    # Defining Multilayers
    multiLayer_1 = ba.MultiLayer()
    multiLayer_1.addLayer(layer_1)
    multiLayer_1.addLayer(layer_2)
    return multiLayer_1

```

```
58
59  def get_simulation():
60      simulation = ba.GISASSimulation()
61
62      detector = ba.RectangularDetector(981, 168.7, 1043, 179.4)
63      detector.setPerpendicularToDirectBeam(3530.0, 103.8, 50.0)
64      simulation.setDetector(detector)
65
66      simulation.setDetectorResolutionFunction(ba.ResolutionFunction2DGaussian(0.5, 0.5))
67      simulation.setBeamParameters(0.134*nm, 0.197*deg, 0.0*deg)
68      simulation.setBeamIntensity(1.0e+08)
69      distr_1 = ba.DistributionGaussian(0.197*deg, 0.007*deg)
70      simulation.addParameterDistribution("*/Beam/InclinationAngle", distr_1, 5, 2.0, ba.RealLimits.limited(0.0*deg, 90.0*deg))
71      distr_2 = ba.DistributionGaussian(0.0*deg, 0.006*deg)
72      simulation.addParameterDistribution("*/Beam/AzimuthalAngle", distr_2, 5, 2.0, ba.RealLimits.limited(-90.0*deg, 90.0*deg))
73      background = ba.ConstantBackground(1.0e-01)
74      simulation.setBackground(background)
75      return simulation
76
77
78  def run_simulation():
79      sample = get_sample()
80      simulation = get_simulation()
81      simulation.setSample(sample)
82      simulation.runSimulation()
83      return simulation.result()
84
85
86  if __name__ == '__main__':
87      result = run_simulation()
88      ba.plot_simulation_result(result)
89
```

Appendix C Simulation script of GISAXS for nanocomposite film

```python
import numpy as np
import matplotlib
import matplotlib.pyplot as plt
import bornagain as ba
from bornagain import deg, angstrom, nm, nm2, kvector_t

datafile = "wenhai_18488.tif"
xmin, ymin, xmax, ymax = 42.0, 60.0, 156.0, 138.0 # ROI, mm

qy_slice = 0.227
qz_slice = 0.31
noise = 2.0

height = 150*nm
intensity = 3.0e+9
matrix_thickness = 150*nm

outfname="sim"

nparticles=50       # number of particles to simulate disorder. Will slow down the simulation!

fontsize=20         # fontsize for plotting
linewidth=3         # line width for plotting


def get_sample():
    # Defining Materials
    m_air = ba.HomogeneousMaterial("Air", 0.0, 0.0)
    m_matrix = ba.HomogeneousMaterial("Martrix", 2.6e-06, 3e-09)
    m_ps = ba.HomogeneousMaterial("PS", 2.61e-06, 2.78e-09)
    m_fe2o3 = ba.HomogeneousMaterial("Fe2O3", 1.204e-05, 8.344e-07)
    m_sapphire = ba.HomogeneousMaterial("Substrate-sapphire", 9.57e-06, 8.46e-08)

    # Defining Layers
    l_air = ba.Layer(m_air)
    l_matrix = ba.Layer(m_matrix, matrix_thickness)
    l_substrate = ba.Layer(m_sapphire)

    # Defining Form Factors
    ff_cylinder = ba.FormFactorCylinder(5.0*nm, 11.2*nm)
    ff_sphere = ba.FormFactorFullSphere(2.8*nm)

    # Defining Particles
    cylinder = ba.Particle(m_ps, ff_cylinder)
    cylinder_rotation = ba.RotationY(90.0*deg)
    cylinder.setRotation(cylinder_rotation)
    sphere = ba.Particle(m_fe2o3, ff_sphere)
    sphere_position = kvector_t(0.0*nm, 13.8*nm, -2.8*nm)
    sphere.setPosition(sphere_position)


    # Defining composition of particles at specific positions
    particle = ba.ParticleComposition()
    particle.addParticle(cylinder)
    particle.addParticle(sphere)

    # Defining 3D lattices
    lattice = ba.Lattice(
        ba.kvector_t(11.2*nm, 0.0*nm, 0.0*nm),
        ba.kvector_t(0.0*nm, 27.6*nm, 0.0*nm),
        ba.kvector_t(0.0*nm, 13.8*nm, 13.5*nm))

    # Defining crystals: basis particle + lattice
    crystal = ba.Crystal(particle, lattice)
    crystal.setDWFactor(3.8)     # variance of displacement in each dimension (sigma^2)

```

```
    # Defining mesocrystals of various heights
    layout = ba.ParticleLayout()
    for h in np.linspace(60, matrix_thickness, nparticles):
        meso_ff = ba.FormFactorLorentz(300.0*nm, h)
        meso_ff2 = ba.FormFactorBox(600.0*nm, 600.0*nm, h)
        meso = ba.MesoCrystal(crystal, meso_ff)
        meso2 = ba.MesoCrystal(crystal, meso_ff2)
        meso.setPosition(kvector_t(0.0, 0.0, -1*h))
        meso2.setPosition(kvector_t(0.0, 0.0, -1*h))
        layout.addParticle(meso, 0.98)
        layout.addParticle(meso2, 0.02)
    layout.setWeight(1)
    layout.setTotalParticleSurfaceDensity(1.0e-5)

    # loose particles
    layout2 = ba.ParticleLayout()
    for z in np.linspace(-2.8, matrix_thickness, nparticles):
        sphere.setPosition(kvector_t(0.0, 0.0, -1*z))
        layout2.addParticle(sphere, 1.0)
    layout2.setWeight(1)
    layout2.setTotalParticleSurfaceDensity(0.02)

    # Adding layouts to layers
    l_matrix.addLayout(layout)
    l_matrix.addLayout(layout2)
```

```
    # roughness
    roughness = ba.LayerRoughness(30.0*nm, 0.3, 500*nm)

    # Defining Multilayers
    multiLayer = ba.MultiLayer()
    multiLayer.addLayer(l_air)
    multiLayer.addLayer(l_matrix)
    multiLayer.addLayerWithTopRoughness(l_substrate, roughness)
    # multiLayer.addLayer(l_substrate)
    return multiLayer


def get_simulation(roi=True):
    simulation = ba.GISASSimulation()

    detector = ba.RectangularDetector(981, 168.732, 1043, 179.396)
    detector.setPerpendicularToDirectBeam(3530.0, 103.6, 49.82)
    simulation.setDetector(detector)
    if roi:
        simulation.setRegionOfInterest(xmin, ymin, xmax, ymax)
    simulation.addMask(ba.Rectangle(101.0, ymin, 106.0, 97.0), True)
    simulation.setDetectorResolutionFunction(ba.ResolutionFunction2DGaussian(0.172, 0.172))
    simulation.setBeamParameters(0.134*nm, 0.18*deg, 0.0*deg)
    simulation.setBeamIntensity(intensity)
    simulation.getOptions().setUseAvgMaterials(True)
    bg = ba.ConstantBackground(noise)
    # bg = ba.PoissonNoiseBackground()
    simulation.setBackground(bg)
    simulation.setTerminalProgressMonitor()
    return simulation
```

```

def run_simulation(integration=False):
    sample = get_sample()
    simulation = get_simulation()
    simulation.getOptions().setMonteCarloIntegration(integration, 10)
    simulation.setSample(sample)
    simulation.runSimulation()
    return simulation.result()


def load_data(filename=datafile):
    """
    Loads experimental data and returns numpy array.
    """
    simulation = get_simulation()
    data = ba.IntensityDataIOFactory.readIntensityData(filename).array()
    return ba.ConvertData(simulation, data, True)


def save_result(result, fname=outfname):
    # save simulation parameters
    sample = get_sample()
    pstring = sample.parametersToString()
    filename = "{}_parameters.txt".format(fname)
    with open(filename, 'wt') as f:
        f.write("Beam intensity: {}\n".format(intensity))
        f.write(pstring)
```

```
    # save axis limits
    filename = "{}_axes.txt".format(fname)
    axes_labels = ba.get_axes_labels(result, ba.AxesUnits.QSPACE)
    axes_limits = ba.get_axes_limits(result, ba.AxesUnits.QSPACE)
    s = "{name}: {qmin}, {qmax}\n"
    with open(filename, 'wt') as f:
        f.write(s.format(name=axes_labels[0], qmin=axes_limits[0], qmax=axes_limits[1]))
        f.write(s.format(name=axes_labels[1], qmin=axes_limits[2], qmax=axes_limits[3]))

    filename = "{}.txt".format(fname)
    np.savetxt(filename, result.array())


def plot(integration=False):
    plt.style.use('seaborn-talk')
    matplotlib. rcParams['xtick.labelsize'] = fontsize
    matplotlib. rcParams['ytick.labelsize'] = fontsize
    data = load_data()
    plt.figure(figsize=(22, 17))
    zmin = 0.1*noise
    zmax = 2.0e+04
    # ====================
    # Experiment 2D
    # ====================
    plt.subplot(2, 2, 1)
    ba.plot_colormap(data, units=ba.AxesUnits.QSPACE, zmin=zmin, zmax=zmax)
    plt.axhline(y=qz_slice, color='0.5', linestyle='--', linewidth=1)
    plt.axvline(x=qy_slice, color='0.5', linestyle='--', linewidth=1)
    plt.title("Experiment", fontsize=fontsize)
    # ax.tick_params(axis='both', which='major', labelsize=fontsize)
    # ====================
    # Simulation 2D
    # ====================
    result = run_simulation(integration)
    save_result(result)
    axes_labels = ba.get_axes_labels(result, ba.AxesUnits.QSPACE)
    plt.subplot(2, 2, 2)
    ba.plot_colormap(result, units=ba.AxesUnits.QSPACE, zmin=zmin, zmax=zmax)
    plt.axhline(y=qz_slice, color='0.5', linestyle='--', linewidth=1)
    plt.axvline(x=qy_slice, color='0.5', linestyle='--', linewidth=1)
    plt.title("BornAgain simulation", fontsize=fontsize)

    # ====================
    # projection along Qz
    # ====================
    plt.subplot(2, 2, 3)
    exp_qz = data.histogram2d(ba.AxesUnits.QSPACE).projectionY(qy_slice)
    sim_qz = result.histogram2d(ba.AxesUnits.QSPACE).projectionY(qy_slice)
    plt.semilogy(exp_qz.getBinCenters(), exp_qz.getBinValues(), color='k', marker='.', markersize=5, linestyle='None', label="Experiment")
    plt.semilogy(sim_qz.getBinCenters(), sim_qz.getBinValues(), color='g', linewidth=linewidth, label="Simulation")
    plt.xlim(0.1, 1.21)
    plt.ylim(0.5*noise, zmax)
    plt.xlabel(axes_labels[1], fontsize=fontsize)
    plt.ylabel(r'$\mathrm{I(Q_z)}$, a.u.', fontsize=fontsize)
    plt.legend(fontsize=fontsize)
    plt.title(r"Slice along $Q_z$", fontsize=fontsize)
    # ====================
    # projection along Qy
    # ====================
    plt.subplot(2, 2, 4)
    exp_qy = data.histogram2d(ba.AxesUnits.QSPACE).projectionX(qz_slice)
    sim_qy = result.histogram2d(ba.AxesUnits.QSPACE).projectionX(qz_slice)
    plt.semilogy(exp_qy.getBinCenters(), exp_qy.getBinValues(), color='k', marker='.', markersize=5, linestyle='None', label="Experiment")
    plt.semilogy(sim_qy.getBinCenters(), sim_qy.getBinValues(), color='g', linewidth=linewidth, label="Simulation")
    plt.xlim(-0.81, 0.71)
    plt.ylim(0.5*noise, zmax)
    plt.xlabel(axes_labels[0], fontsize=fontsize)
    plt.ylabel(r'$\mathrm{I(Q_y)}$, a.u.', fontsize=fontsize)
    plt.legend(fontsize=fontsize)
    plt.title(r"Slice along $Q_y$", fontsize=fontsize)
    plt.savefig("{}.png".format(outfname))


    # save slices to text files
    np.savetxt("{}_slice_qz.txt".format(outfname), np.column_stack([sim_qz.getBinCenters(), sim_qz.getBinValues()]))
    np.savetxt("{}_slice_qy.txt".format(outfname), np.column_stack([sim_qy.getBinCenters(), sim_qy.getBinValues()]))

    plt.show()


if __name__ == '__main__':
    plot(False)
```

Appendix D Solvent vapor annealing

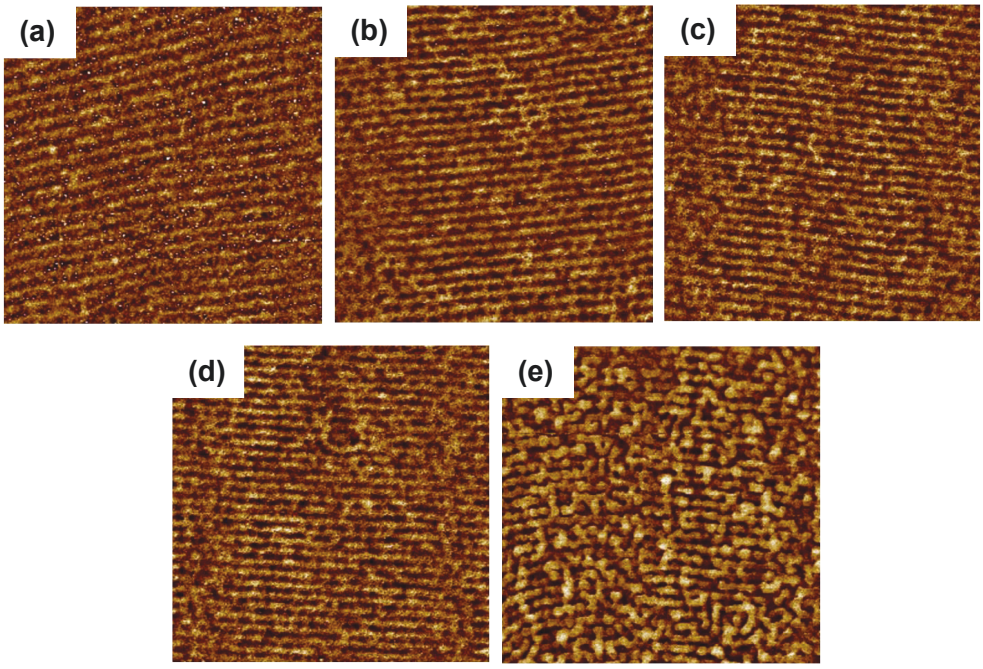

Fig. D.1 AFM phase images of the film annealed with 120 μl solvent for (a)2, (b)4, (c)6, (d)8 and (e)10 minutes, respectively.

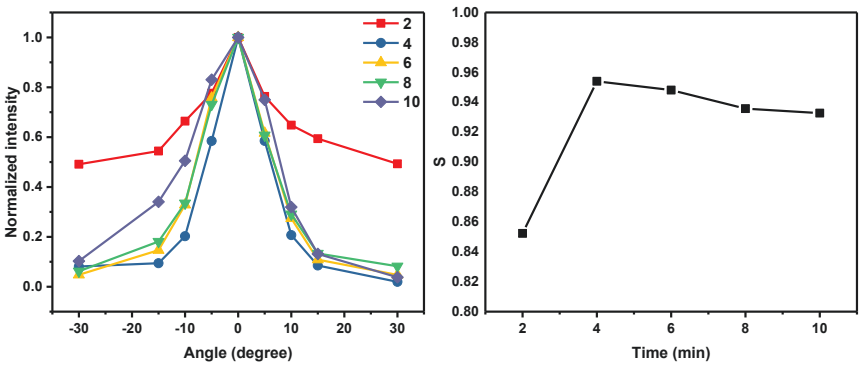

Fig. D.2 (a) The normalized intensity profiles and (b) orientation parameter (S) of films annealed with 120 µl solvent.

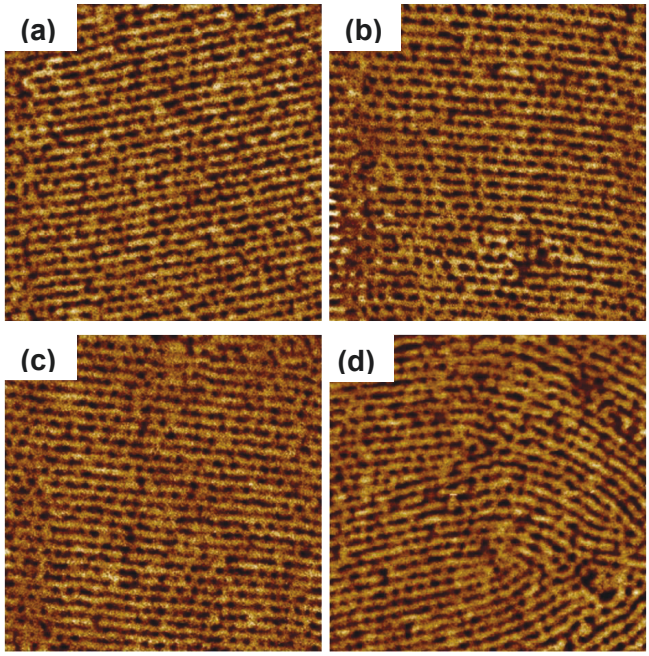

Fig. D.3 AFM phase images of the film annealed with 200 µl solvent for (a)2, (b)4, (c)6 and (d)8 minutes, respectively.

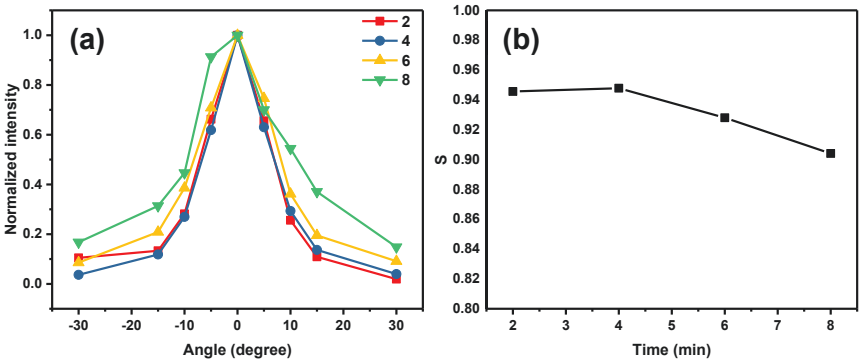

Fig. D.4 (a) The normalized intensity profiles and (b) orientation parameter (S) of films annealed with 200 µl solvent.

Appendix E Neutron scattering 15 wt %

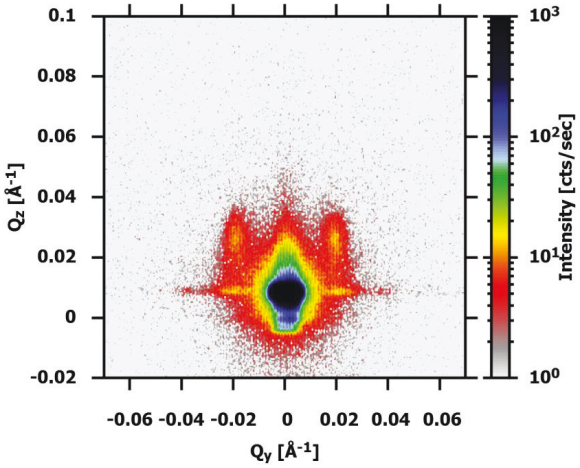

Fig. E. 1. The GISANS data taken at incident angle of 0.4° with λ=6 Å at 280 K.

Reference

Chapter 1

1. Laurent, Sophie, et al. "Magnetic iron oxide nanoparticles: synthesis, stabilization, vectorization, physicochemical characterizations, and biological applications." Chemical reviews 108.6 (2008): 2064-2110.

2. Wang, Xiaojing, et al. "Synthesis, properties, and applications of hollow micro-/nanostructures." Chemical reviews 116.18 (2016): 10983-11060.

3. Ghosh Chaudhuri, Rajib, and Santanu Paria. "Core/shell nanoparticles: classes, properties, synthesis mechanisms, characterization, and applications." Chemical reviews 112.4 (2011): 2373-2433.

4. Greybush, Nicholas J., et al. "Plasmon-enhanced upconversion luminescence in single nanophosphor–nanorod heterodimers formed through template-assisted self-assembly." ACS nano 8.9 (2014): 9482-9491.

5. Kim, Aryeon, et al. "Solvent‐free directed patterning of a highly ordered liquid crystalline organic semiconductor via template‐assisted self‐assembly for organic transistors." Advanced Materials 25.43 (2013): 6219-6225.

6. Yap, Fung Ling, et al. "Nanoparticle cluster arrays for high-performance SERS through directed self-assembly on flat substrates and on optical fibers." Acs Nano 6.3 (2012): 2056-2070.

7. Chang, Hsuan‐Chun, et al. "Single‐crystal C60 needle/CuPc nanoparticle double floating‐gate for low‐voltage organic transistors based non‐volatile memory devices." Advanced Materials 27.1 (2015): 27-33.

8. Zhou, Lin, et al. "3D self-assembly of aluminium nanoparticles for plasmon-enhanced solar desalination." Nature Photonics 10.6 (2016): 393.

9. Hunt, Sean T., et al. "Self-assembly of noble metal monolayers on transition metal carbide nanoparticle catalysts." Science 352.6288 (2016): 974-978.

10. Dong, Bin, et al. "Directed self-assembly of nanoparticles for nanomotors." ACS nano 7.6 (2013): 5192-5198

11. Yi, Chenglin, et al. "Anisotropic self-assembly of hairy inorganic nanoparticles." Accounts of chemical research 50.1 (2016): 12-21.

12. Gwo, Shangjr, et al. "Nanomanipulation and controlled self-assembly of metal nanoparticles and nanocrystals for plasmonics." Chemical Society Reviews 45.20 (2016): 5672-5716.

13. Ross, Caroline A., et al. "Three‐Dimensional Nanofabrication by Block Copolymer Self‐Assembly." Advanced Materials 26.25 (2014): 4386-4396.

14. Ozdemir, Tugce, et al. "Assembly of magnetic nanoparticles into higher structures on patterned magnetic beads under the influence of magnetic field." Nanotechnology 21.12 (2010): 125603.

15. Wang, Mingsheng, Le He, and Yadong Yin. "Magnetic field guided colloidal assembly." Materials Today 16.4 (2013): 110-116.

16. Hanske, Christoph, et al. "Strongly coupled plasmonic modes on macroscopic areas via template-assisted colloidal self-assembly." Nano letters 14.12 (2014): 6863-6871.

17. Yin, Yadong, and Younan Xia. "Self-assembly of spherical colloids into helical chains with well-controlled handedness." Journal of the American Chemical Society 125.8 (2003): 2048-2049.

18. Yin, Yadong, and Younan Xia. "Self‐assembly of monodispersed spherical colloids into complex aggregates with well‐defined sizes, shapes, and structures." Advanced Materials 13.4 (2001): 267-271.

19. Holzner, Felix, et al. "Directed placement of gold nanorods using a removable template for guided assembly." Nano letters 11.9 (2011): 3957-3962.

20. Kiziroglou, Michail E., et al. "Orientation and symmetry control of inverse sphere magnetic nanoarrays by guided self-assembly." Journal of applied physics 100.11 (2006): 113720.

21. Asbahi, Mohamed, et al. "Directed self-assembly of densely packed gold nanoparticles." Langmuir 28.49 (2012): 16782-16787.

22. Park, Soojin, et al. "Macroscopic 10-terabit–per–square-inch arrays from block copolymers with lateral order." Science 323.5917 (2009): 1030-1033.

23. Hong, Sung Woo, et al. "Unidirectionally aligned line patterns driven by entropic effects on faceted surfaces." Proceedings of the National Academy of Sciences 109.5 (2012): 1402-1406.

24. Kao, Joseph, et al. "Direct 3‐D Nanoparticle Assemblies in Thin Films via Topographically Patterned Surfaces." Advanced Materials 26.18 (2014): 2777-2781.

25. Erb, Denise J., Kai Schlage, and Ralf Röhlsberger. "Uniform metal nanostructures with long-range order via three-step hierarchical self-assembly." Science advances 1.10 (2015): e1500751.

26. Shelton, Cameron K., et al. "Tracking Solvent Distribution in Block Polymer Thin Films during Solvent Vapor Annealing with in Situ Neutron Scattering." Macromolecules 49.19 (2016): 7525-7534.

27. Mueller-Buschbaum, Peter. "GISAXS and GISANS as metrology technique for understanding the 3D morphology of block copolymer thin films." European Polymer Journal 81 (2016): 470-493.

28. Lauter-Pasyuk, V., et al. "Neutron reflectivity studies of composite nanoparticle–copolymer thin films." Physica B: Condensed Matter 248.1-4 (1998): 243-245.

29. Lauter-Pasyuk, V., et al. "Nanoparticles in block-copolymer films studied by specular and off-specular neutron scattering." Langmuir 19.19 (2003): 7783-7788.

Chapter 2

1. Blundell, Stephen. "Magnetism in condensed matter." (2003): 94-95.

2. Robert, C. OHandley, and O. Handley. "Modern magnetic materials: principles and applications." Ed. John Wiley & Sons, Inc., New York (2000).

3. Bedanta, Subhankar, Oleg Petracic, and Wolfgang Kleemann. "Supermagnetism." Handbook of magnetic materials. Vol. 23. Elsevier, 2015. 1-83.

4. Petracic, O. "Superparamagnetic nanoparticle ensembles." Superlattices and Microstructures 47.5 (2010): 569-578.

5. Ce, Yang, Hou Yang-Long, and Gao Song. "Nanomagnetism: Principles, nanostructures, and biomedical applications." Chinese Physics B 23.5 (2014): 057505.

6. Néel, L. "Theory of magnetic viscosity of fine grained ferromagnetics with application to baked clays." Ann. Geophys 5.99-136 (1949): 41.

7. Brown Jr, William Fuller. "Thermal fluctuations of a single-domain particle." Physical Review 130.5 (1963): 1677.

8. Zheng, R. K., et al. "The origin of the non-monotonic field dependence of the blocking temperature in magnetic nanoparticles." Journal of Physics: Condensed Matter 18.26 (2006): 5905.

9. Demortiere, Arnaud, et al. "Size-dependent properties of magnetic iron oxide nanocrystals." Nanoscale 3.1 (2011): 225-232.

10. Dronskowski, Richard. "The little maghemite story: A classic functional material." Advanced Functional Materials 11.1 (2001): 27-29.

11. Dormann, JEAN-LOUIS, D. I. N. O. Fiorani, and E. L. I. S. A. B. E. T. H. Tronc. "Magnetic relaxation in fine‐particle systems." Advances in chemical physics 98 (1997): 283-494.

12. Bødker, Franz, Steen Mørup, and Søren Linderoth. "Surface effects in metallic iron nanoparticles." Physical Review Letters 72.2 (1994): 282.

13. Ehlert, Sascha, et al. "Polymer ligand exchange to control stabilization and compatibilization of nanocrystals." ACS nano 8.6 (2014): 6114-6122.

14. Ryan, Kevin M., et al. "Electric-field-assisted assembly of perpendicularly oriented nanorod superlattices." Nano letters 6.7 (2006): 1479-1482.

15. Ahniyaz, Anwar, Yasuhiro Sakamoto, and Lennart Bergström. "Magnetic field-induced assembly of oriented superlattices from maghemite nanocubes." Proceedings of the National Academy of Sciences 104.45 (2007): 17570-17574.

16. Zaraska, Leszek, et al. "Porous anodic alumina formed by anodization of aluminum alloy (AA1050) and high purity aluminum." Electrochimica Acta 55.14 (2010): 4377-4386.

17. Wang, Li-Ming, et al. "Manipulation of dipolar magnetism in low-dimensional iron oxide nanoparticle assemblies." Physical Chemistry Chemical Physics (2019).

18. Heffelfinger, Jason R., Michael W. Bench, and C. Barry Carter. "On the faceting of ceramic surfaces." Surface Science 343.1-2 (1995): L1161-L1166.

19. Kao, Joseph, et al. "Toward functional nanocomposites: taking the best of nanoparticles, polymers, and small molecules." Chemical Society Reviews 42.7 (2013): 2654-2678.

20. Botiz, Ioan, and Seth B. Darling. "Optoelectronics using block copolymers." Materials Today 13.5 (2010): 42-51.

21. Thomas Brückel, Stephan Förster, Georg Roth, and Reiner Zorn (Editors), Laboratory Course Neutron Scattering: Lectures, Forschungszentrum Jülich GmbH Zentralbibliothek, 2018.

22. Griffiths, David J. Introduction to quantum mechanics. Cambridge University Press, 1994.

23. Yoneda, Y. "Anomalous surface reflection of X rays." Physical review 131.5 (1963): 2010.

24. Korolkov, D. Structural analysis of diblock copolymer nanotemplates using grazing incidence scattering, Thesis, Forschungszentrum Jülich, 2008.

25. J. Burle, C. Durniak, J. M. Fisher, M. Ganeva, G. Pospelov, W. Van Herck, J. Wuttke, D. Yurov (2018), BornAgain - Software for simulating and fitting X-ray and neutron small-angle scattering at grazing incidence, version N.n, http://www.bornagainproject.org.

26. Tanwar, Sanju, et al. "Magnetic field dependence of blocking temperature in oleic acid functionalized iron oxide nanoparticles." Journal of superconductivity and novel magnetism 25.6 (2012): 2041-2045.

27. Hamaker, Hugo C. "The London-van der Waals attraction between spherical particles." physica 4.10 (1937): 1058-1072.

Chapter 3

1. J. Burle, C. Durniak, J. M. Fisher, M. Ganeva, G. Pospelov, W. Van Herck, J. Wuttke, D. Yurov (2018), BornAgain - Software for simulating and fitting X-ray and neutron small-angle scattering at grazing incidence, version N.n, http://www.bornagainproject.org.

2. Jülich Centre for Neutron Science. (2016). GALAXI: Gallium anode low-angle x-ray instrument. Journal of large-scale research facilities, 2, A61. http://dx.doi.org/10.17815/jlsrf-2-109

3. Doucet, Mathieu, et al. " SasView Version 4.1." Zenodo http://dx. doi . org/10.5281/ zenodo 438138 (2017).

4. Heinz Maier-Leibnitz Zentrum. (2015). MARIA: Magnetic reflectometer with high incident angle. Journal of large-scale research facilities, 1, A8. http://dx.doi.org/10.17815/jlsrf-1-29.

Chapter 4

1. Sun, Shouheng, et al. "Monodisperse FePt nanoparticles and ferromagnetic FePt nanocrystal superlattices." science 287.5460 (2000): 1989-1992.

2. Zhou, Li, Chao Gao, and Weijian Xu. "Robust Fe3O4/SiO2-Pt/Au/Pd magnetic nanocatalysts with multifunctional hyperbranched polyglycerol amplifiers." Langmuir 26.13 (2010): 11217-11225.

3. Zeng, Hao, et al. "Exchange-coupled nanocomposite magnets by nanoparticle self-assembly." Nature 420.6914 (2002): 395.

4. https://www.oceannanotech.com/products-type/iron-oxide-nanoparticles-5-30nm/iron-oxide-in-organic-solvents.html

5. Shavel, Alexey, et al. "Synthesis and characterization of iron/iron oxide core/shell nanocubes." Advanced functional materials 17.18 (2007): 3870-3876.

6. Park, Jongnam, et al. "Ultra-large-scale syntheses of monodisperse nanocrystals." Nature materials 3.12 (2004): 891.

7. Shavel, Alexey, et al. "Synthesis and characterization of iron/iron oxide core/shell nanocubes." Advanced functional materials 17.18 (2007): 3870-3876.

8. https://www.dectris.com/technology/dectris-detector-technology/asics/pilatus

9. Doucet, Mathieu, et al. " SasView Version 4.1." Zenodo http://dx. doi . org/10.5281/ zenodo 438138 (2017).

10. Gabai, Rachel, Ariel Ismach, and Ernesto Joselevich. "Nanofacet Lithography: A New Bottom‐Up Approach to Nanopatterning and Nanofabrication by Soft Replication of Spontaneously Faceted Crystal Surfaces." Advanced Materials 19.10 (2007): 1325-1330.

11. Choi*, Jung‐Hae, et al. "Equilibrium shape of internal cavities in sapphire." Journal of the American Ceramic Society 80.1 (1997): 62-68.

12. Heffelfinger, Jason R., Michael W. Bench, and C. Barry Carter. "On the faceting of ceramic surfaces." Surface Science 343.1-2 (1995): L1161-L1166.

13. Huth, Michael, et al. "Highly Ordered Fe and Nb Stripe Arrays on Facetted α‐Al2O3 (10¯1 0)." Advanced Functional Materials 12.5 (2002): 333-338.

14. Heffelfinger, Jason R., and C. Barry Carter. "Mechanisms of surface faceting and coarsening." Surface Science 389.1-3 (1997): 188-200.

Chapter 5

1. Shukla, Nisha, Joachim Ahner, and Dieter Weller. "Dip-coating of FePt nanoparticle films: surfactant effects." Journal of Magnetism and Magnetic Materials 272 (2004): E1349-E1351.

2. Josten, Elisabeth, et al. "Superlattice growth and rearrangement during evaporation-induced nanoparticle self-assembly." Scientific reports 7.1 (2017): 2802.

3. Hong, Young-Kyu, et al. "Controlled two-dimensional distribution of nanoparticles by spin-coating method." Applied Physics Letters 80.5 (2002): 844-846.

4. Demirörs, Ahmet Faik, et al. "Directed self-assembly of colloidal dumbbells with an electric field." Langmuir 26.18 (2010): 14466-14471.

5. Singh, Gurvinder, et al. "Magnetic field-induced self-assembly of iron oxide nanocubes." Faraday discussions 181 (2015): 403-421.

6. Wang, Dayang, and Helmuth Möhwald. "Template-directed colloidal self-assembly–the route to 'top-down'nanochemical engineering." Journal of Materials Chemistry 14.4 (2004): 459-468.

7. Dauksher, W. J., et al. "Nano-imprint lithography: templates, imprinting and wafer pattern transfer." Microelectronic engineering 83.4-9 (2006): 929-932.

8. Hong, Sung Woo, et al. "Controlled Orientation of Block Copolymers on Defect‐Free Faceted Surfaces." Advanced Materials 24.31 (2012): 4278-4283.

9. Wang, Xin, and Gao-Rong Han. "Fabrication and characterization of anodic aluminum oxide template." Microelectronic Engineering 66.1-4 (2003): 166-170.

10. Gabai, Rachel, Ariel Ismach, and Ernesto Joselevich. "Nanofacet Lithography: A New Bottom‐Up Approach to Nanopatterning and Nanofabrication by Soft Replication of Spontaneously Faceted Crystal Surfaces." Advanced Materials 19.10 (2007): 1325-1330.

11. Huth M, Ritley K A, Oster J, et al. Highly Ordered Fe and Nb Stripe Arrays on Facetted α-Al2O3 (10-10)[J]. Advanced Functional Materials, 2002, 12(5): 333-338.

12. Heffelfinger J R, Bench M W, Carter C B. On the faceting of ceramic surfaces[J]. Surface science, 1995, 343(1): L1161-L1166.

Chapter 6

1. Albert, Julie NL, and Thomas H. Epps III. "Self-assembly of block copolymer thin films." Materials Today 13.6 (2010): 24-33.

2. Lin, Yao, et al. "Self-directed self-assembly of nanoparticle/copolymer mixtures." Nature 434.7029 (2005): 55.

3. Stark, Wendelin J., et al. "Industrial applications of nanoparticles." Chemical Society Reviews 44.16 (2015): 5793-5805.

4. Sim, Seunghyun, et al. "Tailoring micrometer-long high-integrity 1D array of superparamagnetic nanoparticles in a nanotubular protein jacket and its lateral magnetic assembling behavior." Journal of the American Chemical Society 137.14 (2015): 4658-4661.

5. Katagiri, Kiyofumi, et al. "Magnetoresponsive on‐demand release of hybrid liposomes formed from Fe3O4 nanoparticles and thermosensitive block copolymers." Small 7.12 (2011): 1683-1689.

6. Bregar, Vladimir B. "Advantages of ferromagnetic nanoparticle composites in microwave absorbers." IEEE Transactions on Magnetics 40.3 (2004): 1679-1684.

7. van Zoelen, Wendy, et al. "Phase behavior of solvent vapor annealed thin films of PS-b-P4VP (PDP) supramolecules." Macromolecules 41.9 (2008): 3199-3208.

8. van Zoelen, Wendy, Evgeny Polushkin, and Gerrit Ten Brinke. "Hierarchical terrace formation in PS-b-P4VP (PDP) supramolecular thin films." Macromolecules 41.22 (2008): 8807-8814.

9. Vukovic, Ivana, Gerrit ten Brinke, and Katja Loos. "Hexagonally perforated layer morphology in PS-b-P4VP (PDP) supramolecules." Macromolecules 45.23 (2012): 9409-9418.

10. Perepichka, Iryna I., et al. "Understanding and controlling morphology formation in Langmuir–Blodgett block copolymer films using PS-P4VP and PS-P4VP/PDP." Langmuir 29.14 (2013): 4502-4519.

11. Ikkala, Olli, and Gerrit ten Brinke. "Hierarchical self-assembly in polymeric complexes: towards functional materials." Chemical Communications 19 (2004): 2131-2137.

12. Kao, Joseph, et al. "Direct 3‐D Nanoparticle Assemblies in Thin Films via Topographically Patterned Surfaces." Advanced Materials 26.18 (2014): 2777-2781.

13. Huang, Jingyu, Yihan Xiao, and Ting Xu. "Achieving 3-D Nanoparticle Assembly in Nanocomposite Thin Films via Kinetic Control." Macromolecules 50.5 (2017): 2183-2188.

14. Thorkelsson, Kari, et al. "Direct nanorod assembly using block copolymer-based supramolecules." Nano letters 12.1 (2011): 498-504.

15. Thorkelsson, Kari, et al. "End-to-end alignment of nanorods in thin films." Nano letters 13.10 (2013): 4908-4913.

16. Hsu, Su-Wen, and Ting Xu. "Tailoring Co-assembly of Nanodiscs and Block Copolymer-Based Supramolecules by Manipulating Interparticle Interactions." Macromolecules 52.7 (2019): 2833-2842.

17. Berry, Brian C., et al. "Orientational order in block copolymer films zone annealed below the order− disorder transition temperature." Nano letters 7.9 (2007): 2789-2794.

18. Sinturel, Christophe, et al. "Solvent vapor annealing of block polymer thin films." Macromolecules 46.14 (2013): 5399-5415.

19. Deshpande, Girish, and Mary E. Rezac. "Kinetic aspects of the thermal degradation of poly (dimethyl siloxane) and poly (dimethyl diphenyl siloxane)." Polymer Degradation and Stability 76.1 (2002): 17-24.

20. Evans, Katherine, and Ting Xu. "Self-Assembly of Supramolecular Thin Films: Role of Small Molecule and Solvent Vapor Annealing." Macromolecules 52.2 (2018): 639-648.

21. Hong, Sung Woo, et al. "Controlled Orientation of Block Copolymers on Defect‐Free Faceted Surfaces." Advanced Materials 24.31 (2012): 4278-4283.

22. Park, Soojin, et al. "Macroscopic 10-terabit–per–square-inch arrays from block copolymers with lateral order." Science 323.5917 (2009): 1030-1033.

23. D. Frenkel , R. Eppenga , Phys. Rev. A 1985 , 31 , 1776.

24. Busch, P., et al. "Grazing-incidence small-angle X-ray scattering from thin polymer films with lamellar structures–the scattering cross section in the distorted-wave Born approximation." Journal of applied crystallography 39.3 (2006): 433-442.

25. Busch, Peter, et al. "Debye–Scherrer rings from block copolymer films with powder-like order." Journal of applied crystallography 44.2 (2011): 370-379.

26. Thorkelsson, Kari, Noah Bronstein, and Ting Xu. "Nanorod-based supramolecular nanocomposites: effects of nanorod length." Macromolecules 49.17 (2016): 6669-6677.

27. Flensburg, Claus, and Robert F. Stewart. "Lattice dynamical Debye-Waller factor for silicon." Physical Review B 60.1 (1999): 284.

28. Vargas, J. M., et al. "Effect of dipolar interaction observed in iron-based nanoparticles." Physical Review B 72.18 (2005): 184428.

Chapter 7

1. Huang, Jing, et al. "Magnetic nanoparticle facilitated drug delivery for cancer therapy with targeted and image‐guided approaches." Advanced functional materials 26.22 (2016): 3818-3836.

2. Wu, Wei, et al. "Recent progress on magnetic iron oxide nanoparticles: synthesis, surface functional strategies and biomedical applications." Science and technology of advanced materials 16.2 (2015): 023501.

3. Akbarzadeh, Abolfazl, Mohammad Samiei, and Soodabeh Davaran. "Magnetic nanoparticles: preparation, physical properties, and applications in biomedicine." Nanoscale research letters 7.1 (2012): 144.

4. Hauser, Anastasia K., et al. "Magnetic nanoparticles and nanocomposites for remote controlled therapies." Journal of Controlled Release 219 (2015): 76-94.

5. Peng, Erwin, Fenghe Wang, and Jun Min Xue. "Nanostructured magnetic nanocomposites as MRI contrast agents." Journal of Materials Chemistry B 3.11 (2015): 2241-2276.

6. Wang, Dongmei, et al. "Fabrication of thermo-responsive polymer functionalized reduced graphene oxide@ Fe 3 O 4@ Au magnetic nanocomposites for enhanced catalytic applications." Journal of Materials Chemistry A 5.10 (2017): 5088-5097.

7. Barandiaran, I., and G. Kortaberria. "Synthesis and characterization of nanostructured PS-b-P4VP/Fe 2 O 3 thin films with magnetic properties prepared by solvent vapor annealing." RSC Advances 5.116 (2015): 95840-95846.

8. Wang, Hyun Suk, Ki Hyun Kim, and Joona Bang. "Thermal Approaches to Perpendicular Block Copolymer Microdomains in Thin Films: A Review and Appraisal." Macromolecular rapid communications 40.4 (2019): 1800728.

9. Sageshima, Yoshio, et al. "Fabrication and modification of ordered nanoporous structures from nanophase-separated block copolymer/metal salt hybrids." Langmuir 28.50 (2012): 17524-17529.

10. Müller-Buschbaum, Peter. "Grazing incidence small-angle neutron scattering: challenges and possibilities." Polymer journal 45.1 (2013): 34.

11. Mueller-Buschbaum, Peter. "GISAXS and GISANS as metrology technique for understanding the 3D morphology of block copolymer thin films." European Polymer Journal 81 (2016): 470-493.

12. Theis-Bröhl, Katharina, et al. "Self-ordering of nanoparticles in magneto-organic composite films." Physical Review B 78.13 (2008): 134426.

13. Heinz Maier-Leibnitz Zentrum. (2015). MARIA: Magnetic reflectometer with high incident angle. Journal of large-scale research facilities, 1, A8. http://dx.doi.org/10.17815/jlsrf-1-29.

14. SLD calculator, https://sld-calculator.appspot.com/

15. Björck, Matts, and Gabriella Andersson. "GenX: an extensible X-ray reflectivity refinement program utilizing differential evolution." Journal of Applied Crystallography 40.6 (2007): 1174-1178.

Acknowledgement

I would like to extend my sincere gratitude for everyone who graciously supported me during my graduate years. First and foremost, I would like to thank Prof. Dr. Thomas Brückel for providing me the opportunity to work in JCNS-2. He introduced me to the wonderful community and gave me the chance to 'see' the world with neutrons. He also granted me the freedom to pursue my research interests, and introduced me to many brilliant colleagues. I am grateful for his guidance and cultivation throughout the years.

I also would like to thank Prof. Dr. Joachim Mayer for agreeing to be the second referee of my thesis. I would like to thank him for his excellent advices.

I would like to express my thankfulness to my two supervisors Dr. Yinguo Xiao and Dr. Mikhail Feygenson. I sincerely acknowledge them for their encouragement, patience and support during my thesis. I sincerely appreciate their advices about the scientific career. I always enjoyed discussing with them.

I also would like to thank everyone in the group whom I had the pleasure to spend these past 4 years with. They are not only my colleagues in lab but also my dear friends in life. They make JCNS-2 as such a collaborative and friendly place to explore interesting scientific questions. I am especially grateful to Dr. Emmanuel Kentzinger, Dr. Ulrich Rucker, Dr. Alexandros Koutsioumpas, Dr. Stefan Mattauch, Dr. Kirill Zhernenkov, Dr. Marina Ganeva and Berthold Schmitz, who have been supporting me in my PhD study. I also appreciate the help and company of Dr. Xiao Sun, Dr. Liming Wang, Dr. Erxi Feng and Lei Cao, Nileena Nandakumaran, Annika Stellhorn, Asma Qdemat, Mohammed Ait Haddouch, and Dr. Anirban Sarkar. They are good friends who never hesitate to share a joke, a laugh, and a beer. I have learned much from them, both professionally and personally.

Financial support from China Scholarship Council (CSC) is gratefully acknowledged.

Finally, I would like to thank my parents. They offered me their unconditional love and support for my academic pursuit, and encouraged me to overcome many difficulties as they arise.

Band / Volume 200
Variability and compensation in Alzheimer's disease across different neuronal network scales
C. Bachmann (2019), xvi, 165 pp
ISBN: 978-3-95806-420-1

Band / Volume 201
Crystal structures and vibrational properties of chalcogenides: the role of temperature and pressure
M. G. Herrmann (2019), xi, 156 pp
ISBN: 978-3-95806-421-8

Band / Volume 202
Current-induced magnetization switching in a model epitaxial Fe/Au bilayer
P. Gospodarič (2019), vi, 120, XXXVIII pp
ISBN: 978-3-95806-423-2

Band / Volume 203
Network architecture and heme-responsive gene regulation of the two-component systems HrrSA and ChrSA
M. Keppel (2019), IV, 169 pp
ISBN: 978-3-95806-427-0

Band / Volume 204
Spin-orbitronics at the nanoscale: From analytical models to real materials
J. Bouaziz (2019), 228 pp
ISBN: 978-3-95806-429-4

Band / Volume 205
Advanced methods for atomic scale spin simulations and application to localized magnetic states
G. P. Müller (2019), xx, 194 pp
ISBN: 978-3-95806-432-4

Band / Volume 206
Different growth modes of molecular adsorbate systems and 2D materials investigated by low-energy electron microscopy
J. E. Felter (2019), vi, 114, XXXIV pp
ISBN: 978-3-95806-434-8

Band / Volume 207
NADPH-related studies performed with a SoxR-based biosensor in *Escherichia coli*
A. Spielmann (2019), IV, 73 pp
ISBN: 978-3-95806-438-6

Band / Volume 208
Chemisorption aromatischer Moleküle auf Übergangsmetalloberflächen: Bildung molekularer Hybridmagnete
S. Schleicher (2019), 109 pp
ISBN: 978-3-95806-442-3

Band / Volume 209
Regulatory interactions between *Corynebacterium glutamicum* and its prophages
M. Hünnefeld (2019), IV, 209 pp
ISBN: 978-3-95806-445-4

Band / Volume 210
Quantum Technology
Lecture Notes of the 51st IFF Spring School 2020
23 March – 03 April 2020, Jülich, Germany
ed. by H. Bluhm, T. Calarco, D. DiVincenzo (2020), ca. 700 pp
ISBN: 978-3-95806-449-2

Band / Volume 211
Interaction of physical fields with nanostructured materials
(2020), 255 pp
ISBN: 978-3-95806-450-8

Band / Volume 212
First-principles study of collective spin excitations in noncollinear magnets
F.J. dos Santos (2020), 270 pp
ISBN: 978-3-95806-459-1

Band / Volume 213
Direct measurement of anisotropic resistivity in thin films using a 4-probe STM
T. Flatten (2020), viii, 129 pp
ISBN: 978-3-95806-460-7

Band / Volume 214
The guided self-assembly of magnetic nanoparticles into two- and three-dimensional nanostructures using patterned substrates
W. Ji (2020), VI, 140 pp
ISBN: 978-3-95806-462-1

Weitere ***Schriften des Verlags im Forschungszentrum Jülich*** unter
http://wwwzb1.fz-juelich.de/verlagextern1/index.asp

Schlüsseltechnologien / Key Technologies
Band / Volume 214
ISBN 978-3-95806-462-1

Mitglied der Helmholtz-Gemeinschaft

JÜLICH
Forschungszentrum